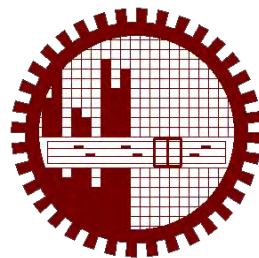


An Experimental Study on the Aerodynamic Performance of Winglets with Curve Edged Wing of NACA 4412

By

Ismat Ara

MASTER OF SCIENCE IN MECHANICAL ENGINEERING



Department of Mechanical Engineering
BANGLADESH UNIVERSITY OF ENGINEERING & TECHNOLOGY

February 2018

**An Experimental Study on the Aerodynamic Performance of Winglets
with Curve Edged Wing of NACA 4412**

By

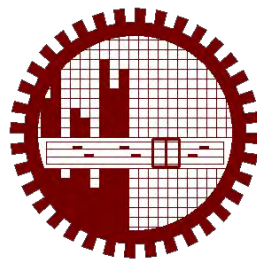
Ismat Ara

A THESIS SUBMITTED TO THE DEPARTMENT OF MECHANICAL ENGINEERING,
BANGLADESH UNIVERSITY OF ENGINEERING AND TECHNOLOGY (BUET) IN
PARTIAL FULFILLMENT OF THE REQUIREMENTS FOR THE DEGREE OF
MASTER OF SCIENCE IN MECHANICAL ENGINEERING

Supervised by

Dr. Mohammad Ali

Professor, Department of Mechanical Engineering



Department of Mechanical Engineering
BANGLADESH UNIVERSITY OF ENGINEERING & TECHNOLOGY

February 2018

DEDICATION


Dedicate this thesis


To my teachers;

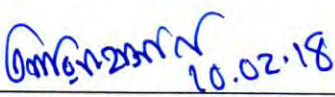
To my parents;

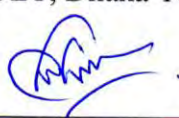
The thesis titled “An Experimental Study on the Aerodynamic Performance of Winglets with Curve Edged Wing of NACA 4412,” submitted by Ismat Ara, Roll: P0413102112, Session: April-2013, has been accepted as satisfactory in partial fulfillment of the requirements for the degree of Master of Science in Mechanical Engineering on 10th February 2018.

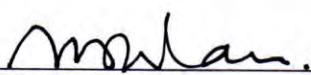
BOARD OF EXAMINERS

1. 

Dr. Mohammad Ali
Professor
Department of Mechanical Engineering
BUET, Dhaka-1000, Bangladesh. Chairman
(Supervisor)
2. 

Head
Department of Mechanical Engineering
BUET, Dhaka-1000, Bangladesh. Member
(Ex-Officio)
3. 

Dr. Mohammad Arif Hasan Mamun
Professor
Department of Mechanical Engineering
BUET, Dhaka-1000, Bangladesh. Member
4. 

Dr. Mohammad Mamun
Professor
Department of Mechanical Engineering
BUET, Dhaka-1000, Bangladesh. Member
5. 

Dr. Md. Quamrul Islam
Professor
Military Institute of Science & Technology
Mirpur, Dhaka-1216, Bangladesh. Member
(External)

ABSTRACT

Aerodynamic drag force breakdown of a typical transport aircraft shows that lift-induced drag can be as much as 40% of total drag at cruise conditions and 80-90% of the total drag in take-off configuration. Induced drag is caused due to wingtip vortices formed by the difference in pressure between the upper and lower surfaces of the wing. The main aim of implementing winglet is to reduce the induced drag as well as to convert them to additional thrust therefore reducing the fuel cost and increasing the efficiency of the aircraft. This thesis deals with the curved trailing edge tapered wing by adding different winglets at the wing tip. NACA 4412 aerofoil planform is used due to its good stall properties and low roughness effect.

The experimental investigation is carried out in the wind tunnel to explore aerodynamics of wings with three winglet models. For reference curved trailing edged tapered wing is considered as base wing. Including other than base wing three winglets are used namely curved trailing edged tapered wing with blended winglet, curved trailing edged tapered wing with double blended winglet and curved trailing edged tapered wing with spiroid winglet. All the models are designed using Solidworks. The wing and winglets are manufactured by using wood with same span and equal surface area. All the models are tested at air speed of 98.64 km/h (0.08 Mach) i.e. at Reynolds Number 2.05×10^5 in the closed circuit wind tunnel available at Turbulence Laboratory, Department of Mechanical Engineering, BUET. The Static pressure at different AOA (-4° , 0° , 4° , 8° , 12° , 16° , 20° & 24°) is measured from both upper and lower surfaces of the wing models through different pressure tapings by using a multi-tube water manometer. The aerodynamic characteristics (Coefficient of Lift, Coefficient of Drag and Lift to Drag ratio) for different models is determined from the static pressure distribution.

The experimental results show that lift to drag ratio increases and induced drag decreases for wing models with winglets compared to wing model without winglet for the Reynolds number considered in the present study.

ACKNOWLEDGEMENT

At first I would like to express my gratitude to the Almighty for the successful completion of this research. My heart-felt thanks and sincere gratitude to my supervisor Dr. Mohammad Ali, Professor and Head, Department of Mechanical Engineering, BUET, Dhaka, for his continuous guidance, supervision, inspiration, encouragement, and untiring support throughout this research work. It is beyond doubt that without his assistance and kind support, it was impossible for me to complete this research work.

I am grateful to Professor Dr. Md. Quamrul Islam, Department of Mechanical Engineering, MIST, Dhaka and Professor Dr. Mohammad Arif Hasan Mamun and Professor Dr. Mohammad Mamun, Department of Mechanical Engineering, BUET, Dhaka for their cooperation and suggestions whenever needed. Their valuable comments and reviews were very helpful in making this a complete work.

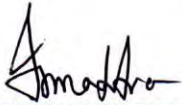
I would also like to thank all the staffs of Turbulence Laboratory of Department of Mechanical Engineering, BUET for providing assistance during preparation of the experimental setup.

Finally, I am very grateful to my family members and friends who supported and motivated me regarding this thesis work.

DECLARATION

It is hereby declared that this thesis or any part of it has not been submitted elsewhere for the award of any degree or qualification.

Signature of the Candidate:

A handwritten signature in black ink, appearing to read 'Ismat Ara', written above a horizontal dashed line.

Ismat Ara



	Page
Cover Sheet	I
Title	II
Dedication	III
Certificate of Approval	IV
Abstract	V
Acknowledgement	VI
Candidate's Declaration	VII
Contents	VIII-XI
List of Figures	XII-XVI
List of Tables	XVII
Nomenclature	XVIII-XIX
CHAPTER - 1 INTRODUCTION	1-3
1.1 General	1
1.2 Background	1
1.3 Winglet Phenomena	2
1.4 Organization of the Thesis	3

CHAPTER-2	LITERATURE REVIEW	4-18
2.1	Induced Drag Phenomena	4
2.2	History of Wingtip Devices and Winglets	6
2.3	Types of Winglets and Wingtip Devices	7
2.3.1	Blended Winglet	7
2.3.2	Spiroid Winglet	8
2.3.3	Wing- Grid as Wing Tip	8
2.3.4	Wingtip Devices	9
2.4	Literature Survey	10
2.5	Summary of the Literature Review	17
2.6	Motivation of the Research Work	18
2.7	Scope and Objectives of the Research	18
CHAPTER-3	OVERVIEW OF WING AND WINGLET AERODYNAMICS	19-46
3.1	Geometric Features of Wing	19
3.2	Geometric Parameters of Wing	20
3.2.1	Mean Geometric Chord	21
3.2.2	Mean Aerodynamic Chord	21
3.2.3	Aspect Ratio	21
3.2.4	Tapper Ratio	21
3.3	Fundamental Aerodynamics of Aerofoil	22
3.3.1	The Kutta-Zhukowski Condition	22
3.3.2	Aerodynamic Characteristics of Aerofoils	25
3.3.3	Lift and Drag Coefficient of Airfoil	27
3.3.4	Aerofoil Data Sources	29
3.3.5	NACA Aerofoils	30
3.3.6	Co-ordinates of NACA Airfoils	30
		Page
3.4	The Finite Wing	32

3.4.1	Flow Field around Finite Wings	32
3.4.2	Downwash an Induced Drag	35
3.4.3	Fundamental Equations of Finite-Wing Theory	39
3.4.4	The Elliptical Lift Distribution	41
3.5	Winglets	44
3.6	Selection Criteria to Use NACA 4412	46
CHAPTER-4	MATHEMATICAL MODELING	47-57
4.1	Determination of Pressure Coefficient	47
4.2	Estimation of Aerodynamic Coefficient	49
CHAPTER-5	EXPERIMENTAL SETUP AND METHODOLOGY	58-66
5.1	Design and Construction	59
5.1.1	Wing Models	59
5.1.2	Pressure Measuring Device	62
5.2	Experimental Setup	62
5.2.1	Wind Tunnel	62
5.2.2	Fixture for Altering Angle of Attack	64
5.2.3	Experimental Parameters	65
5.3	Methodology	65
CHAPTER-6	RESULT AND DISCUSSIONS	67-99
6.1	Introduction	67
6.2	Surface Pressure Distributions	67
6.2.1	Pressure Distributions at -4° AOA	68
6.2.2	Pressure Distributions at 0° AOA	72
6.2.3	Pressure Distributions at 4° AOA	77

Page

6.2.4	Pressure Distributions at 8° AOA	80
6.2.5	Pressure Distributions at 12° AOA	84
6.2.6	Pressure Distributions at 16° AOA	87
6.2.7	Pressure Distributions at 20° AOA	90
6.2.8	Pressure Distributions at 24° AOA	93
6.3	Lift Characteristics	96
6.4	Drag Characteristics	97
6.5	Lift and Drag Ratio	98
6.6	Induced Drag	99
CHAPTER-7	CONCLUSIONS AND RECOMMENDATIONS	100-102
7.1	Conclusion	100
7.2	Recommendations	102
REFERENCES		103-108
APPENDIX-I	Calculated Values of Pressure Coefficient	109-116
APPENDIX-II	Uncertainty Analysis	117-120

LIST OF FIGURES

Figure No	Nomenclature	Page No
Figure 1.1	Vortex Generation at the Wingtip	3
Figure 2.1	Different Forms of Drag	4
Figure 2.2	Distribution of Drag Components	5
Figure 2.3	(a) Flow Pattern of the Velocity (b) Vortex Sheet from Trailing edge	5
Figure 2.4	Blended Winglet	7
Figure 2.5	Spiroid Winglet	8
Figure 2.6	Wing Grids as Wing End Section	9
Figure 2.7	Raked Wing Tip	9
Figure 2.8	Different Types of Tip Devices	10
Figure 3.1	Wing and Aerofoil with Nomenclature	19
Figure 3.2	Geometric Features of a Typical Aircraft Wing	20
Figure 3.3	Wing Geometric Parameters	20
Figure 3.4	Kutta-Zhukowski Condition, No viscosity	23
Figure 3.5	Kutta-Zhukowski Condition, Viscosity	23
Figure 3.6	Starting Vortices	23
Figure 3.7	Airfoil Pressure Distribution	24
Figure No	Nomenclature	Page No

Figure 3.8	Airfoil Characteristics	25
Figure 3.9	Aerodynamic Characteristics of Aircraft Wing	26
Figure 3.10	Flow around an Airfoil	27
Figure 3.11	Variation of Aerodynamic Characteristics with Angle of Attack	27
Figure 3.12	Graphs of Different Parameters of Aerofoil	29
Figure 3.13	NACA Aerofoil Co-ordinates	31
Figure 3.14	Vortex Configuration	32
Figure 3.15	Superimposition of Elliptical Vortices in Steady Flow	33
Figure 3.16	Formation of Trailing Vortices at Wing Tips	34
Figure 3.17	Wing Tip Flow Vortices	34
Figure 3.18	Formation of Trailing Vortices at Wing Tips	35
Figure 3.19	Downwash Velocity w Induced by Trailing Vortices	36
Figure 3.20	Downwash Contribution from Trailing Vortex Filament	38
Figure 3.21	Finite Wing Theory Parameters	39
Figure 3.22	Finite Wing Theory Representation	40
Figure 3.23	Winglet Parameters	45
Figure 4.1	Pressure distribution over an Aerofoil's Surface in terms of C_p	48
Figure 4.2	Illustration of Pressure and Shear Stress on Aerofoil Surface	49
Figure 4.3	Resultant Aerodynamic Force and its Components	50

Figure No	Nomenclature	Page No
------------------	---------------------	----------------

Figure 4.4	Nomenclature for Integration of ρ and τ	51
Figure 4.5	Aerodynamic Force on an Element of the Body Surface	51
Figure 4.6	Reference Area and Length for Airplane	54
Figure 4.7	Geometric Relationship of Differential Lengths	54
Figure 4.8	Paneling of the wing surface	56
Figure 5.1	Solidworks Design of Wing Models	59
Figure 5.2	Curved Trailing Edge Tapered Planform (Reference Wing)	60
Figure 5.3	Experimental Winglet Models	61
Figure 5.4	Multi-tube Manometer	62
Figure 5.5	Photograph of Experimental Set-up	63
Figure 5.6	Schematic Diagram of the Wind tunnel at BUET's Turbulence Lab	64
Figure 5.7	AOA Altering Fixture	65
Figure 6.1	C_p Distribution of Segment-A at $\alpha = -4^\circ$	68
Figure 6.2	C_p Distribution of Segment-B at $\alpha = -4^\circ$	69
Figure 6.3	C_p Distribution of Segment-C at $\alpha = -4^\circ$	70
Figure 6.4	C_p Distribution of Segment-D at $\alpha = -4^\circ$	72
Figure 6.5	C_p Distribution of Segment-A at $\alpha = 0^\circ$	73
Figure 6.6	C_p Distribution of Segment-B at $\alpha = 0^\circ$	74
Figure 6.7	C_p Distribution of Segment-C at $\alpha = 0^\circ$	75
Figure 6.8	C_p Distribution of Segment-D at $\alpha = 0^\circ$	76
Figure 6.9	C_p Distribution of Segment-A at $\alpha = 4^\circ$	77

Figure No	Nomenclature	Page No
------------------	---------------------	----------------

Figure 6.9	C_p Distribution of Segment-A at $\alpha = 4^\circ$	77
Figure 6.10	C_p Distribution of Segment-B at $\alpha = 4^\circ$	78
Figure 6.11	C_p Distribution of Segment-C at $\alpha = 4^\circ$	79
Figure 6.12	C_p Distribution of Segment-D at $\alpha = 4^\circ$	80
Figure 6.13	C_p Distribution of Segment-A at $\alpha = 8^\circ$	81
Figure 6.14	C_p Distribution of Segment-B at $\alpha = 8^\circ$	82
Figure 6.15	C_p Distribution of Segment-C at $\alpha = 8^\circ$	83
Figure 6.16	C_p Distribution of Segment-D at $\alpha = 8^\circ$	83
Figure 6.17	C_p Distribution of Segment-A at $\alpha = 12^\circ$	84
Figure 6.18	C_p Distribution of Segment-B at $\alpha = 12^\circ$	85
Figure 6.19	C_p Distribution of Segment-C at $\alpha = 12^\circ$	86
Figure 6.20	C_p Distribution of Segment-D at $\alpha = 12^\circ$	87
Figure 6.21	C_p Distribution of Segment-A at $\alpha = 16^\circ$	88
Figure 6.22	C_p Distribution of Segment-B at $\alpha = 16^\circ$	89
Figure 6.23	C_p Distribution of Segment-C at $\alpha = 16^\circ$	89
Figure 6.24	C_p Distribution of Segment-D at $\alpha = 16^\circ$	90
Figure 6.25	C_p Distribution of Segment-A at $\alpha = 20^\circ$	91
Figure 6.26	C_p Distribution of Segment-B at $\alpha = 20^\circ$	91
Figure 6.27	C_p Distribution of Segment-C at $\alpha = 20^\circ$	92
Figure 6.28	C_p Distribution of Segment-D at $\alpha = 20^\circ$	92
Figure 6.29	C_p Distribution of Segment-A at $\alpha = 24^\circ$	93
Figure 6.30	C_p Distribution of Segment-B at $\alpha = 24^\circ$	94
Figure No	Nomenclature	Page No

Figure 6.31	C_p Distribution of Segment-C at $\alpha = 24^\circ$	94
Figure 6.32	C_p Distribution of Segment-D at $\alpha = 24^\circ$	95
Figure 6.33	Variation of Lift Coefficient with Angle of Attack	96
Figure 6.34	Variation of Drag Coefficient with Angle of Attack	97
Figure 6.35	Variation of Lift to Drag Ratio with Angle of Attack	98
Figure 6.36	Variation of Induced Drag Coefficient with Angle of Attack	99

LIST OF TABLES

Table No	Nomenclature	Page No
Table 1	Boeing Series Advantages after Using Winglet	17
Table 2	Dimensions of Three Winglet Models	61
Table 3	Calculated Values of Pressure Coefficient at -4° Angle of Attack	109
Table 4	Calculated Values of Pressure Coefficient at 0° Angle of Attack	110
Table 5	Calculated Values of Pressure Coefficient at 4° Angle of Attack	111
Table 6	Calculated Values of Pressure Coefficient at 8° Angle of Attack	112
Table 7	Calculated Values of Pressure Coefficient at 12° Angle of Attack	113
Table 8	Calculated Values of Pressure Coefficient at 16° Angle of Attack	114
Table 9	Calculated Values of Pressure Coefficient at 20° Angle of Attack	115
Table 10	Calculated Values of Pressure Coefficient at 24° Angle of Attack	116

NOMENCLATURE

A	Axial Force
b	Wing Span
C	Wing Chord
C_a	Axial Force Coefficient
C_D	Coefficient of Drag
C_{di}	Sectional Induced Drag Coefficient
C_L	Coefficient of Lift
C_{pl}	Lower Surface Pressure Coefficient
C_n	Normal Force Coefficient
C_p	Coefficient of Pressure
C_{pu}	Upper Surface Pressure Coefficient
C_{root}	Root Chord
C_{tip}	Tip Chord
$c(y)$	Chord Distribution
D	Drag Force
D_i	Induced Drag Force
L	Lift Force
L/D	Lift to Drag Ratio
M	Model
N	Normal Force
p	Pressure
P_∞	Free Stream Pressure
P_i	Local Static Surface Pressure
q_∞	Dynamic Pressure
r_0	Radius of Curvature at Airfoil's Leading Edge
R_N	Reynolds Number
S	Wing Surface Area
t_{max}	Maximum Thickness of Aerofoil

V_{∞}	Free Stream Velocity of Air
v	Velocity of Air
w	Downwash
x_c	Distance of Maximum Camber
x_t	Distance from the Leading Edge of Aerofoil
z_c	Maximum Camber
α	Angle of Attack
α_a	Absolute Angle of Attack
α_{Lmax}	Stalling Angle of Attack
α_i	Induced Angle of Attack
α_o	Effective Angle of Attack
τ	Shear Stress
ρ_a	Density of Air
ρ_w	Density of Water
μ_a	Absolute Viscosity of Air
μ_w	Absolute Viscosity of Water
Γ	Circulation
$\frac{1}{2} \rho U_{\infty}^2$	Free Stream Dynamic Pressure

INTRODUCTION

1.1 General

Wing is the primary lifting surface of an aircraft which sustains the weight of the aircraft to make flight in the air while from aerodynamics perspective it is also the main source of the aircraft drag. As a result, the effects of wing shape and size are crucial to aerodynamic characteristics on which the efficiency of aircraft depends. As such, researches on different wing shapes and geometries are still on throughout the world to explore the maximum possible lift and minimum possible drag. The present research is focusing on the improved aerodynamic characteristics and performance by reducing induced drag which is one of the primary source of drag with the incorporation of various wingtip devices.

1.2 Background

In aerodynamics, the main source of the airplane drag is related with the wing. Around two-thirds of the total drag of typical transport aircraft at cruise conditions is produced by the wing [1]. There are three sources of drag: (i) profile drag which is related to skin friction caused by flow of air over the aircraft surface (ii) induced drag which is the result of lift generation for finite wingspan and (iii) the compressibility drag caused by high speed aerodynamics. The drag stems from the vortices shed by an aircraft's wings, which causes the local relative wind downward (an effect known as downwash) and generate a component of the local lift force in the direction of the free stream. The strength of this induced drag is proportional to the spacing and radii of these vortices. By designing wings, which force the vortices farther apart and at the same time create vortices with larger core radii, may significantly reduce the amount of drag the aircraft induces. Airplanes which experience less drag require less power and therefore less fuel to fly an arbitrary distance, thus making flight more efficient and less costly. So, reduction of induced drag of a wing plays a vital role to make the flight safe, smooth, effective and less costly.

1.3 Winglet Phenomena

Wing is the most important structure of an airplane as it affects the cruise speed, takeoff and landing distances, stall speed, handling qualities (specially near the stall), and overall aerodynamic efficiency during all phases of flight. Lift is generated because there is a lower pressure on the upper wing surface and a higher pressure on the lower wing surface. For a wing of finite span, this effect will cause the flow to pass from the low pressure zone to the high pressure zone at the wingtip as can be seen in Figure 1.1. This crossflow at the wingtip meet at the trailing edge and causes wing-tip vortex. The energy in the vortex originates from the flow around the wing hence the lost energy reduces the overall lift capability of the wing. This lost energy is referred to as induced drag. If there is a wing of infinite aspect ratio, the air flows over the wing surface without any inward or outward deflection, and therefore no wing-tip vortices, no induced drag. But such a thing is not plausible in practical flight. An increase in span automatically increase the root bending moment which in turn needs more structural mass. There is another factor that has to be taken into consideration. Every aircraft is required to have less than 80 meters in span in order to handle on ground at airports. Airports are designed to have no more than 80-meter space between each aircraft. Thus, the increase in root bending moment due to a wing augmentation and the 80-meter airport space are two main restrictions that establish the need for the winglet. Winglets work by increasing the aspect ratio of a wing without adding greatly to the structural stress and hence necessary weight of its structure.

The small extension at the wing tip is called winglet and is placed at any angle to the existing wing surface so that the creation of rotating vortex flow at the wingtip is slowed down. A lift force is generated on the winglet due to the interaction of winglet flow field and main wing flow field giving a forward component which can be seen as negative drag following the definition of drag and lift. This forward component of the lift force reduces the total wing drag.

The purpose of this investigation is to study the aerodynamic characteristics of an added winglet of varied geometries to a NACA 4412 curved trailing edged tapered wing.

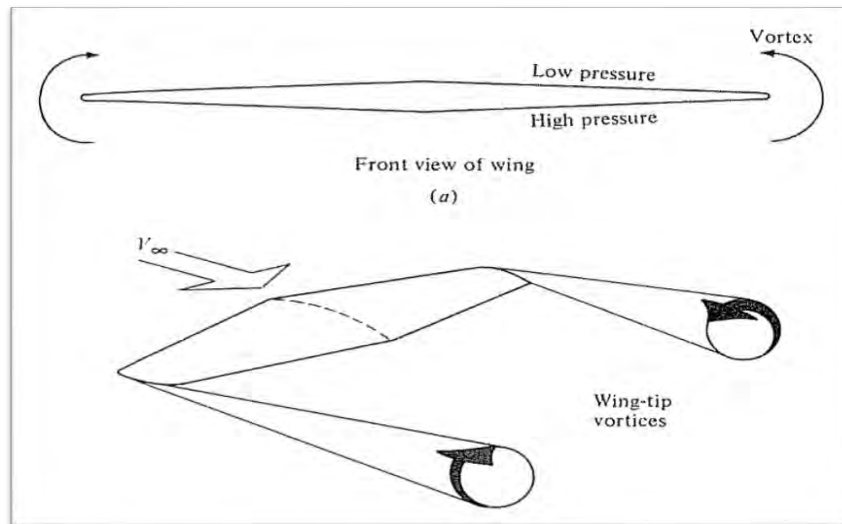


Figure 1.1: Vortex generation at the wing tip

1.4 Organization of the Thesis

The dissertation is divided into seven chapters as follows:

- a. The first chapter covers the background information and winglet phenomena.
- b. The second chapter reviews the available literature related to the present research work along with scope and objectives of the research.
- c. The third chapter presents the overview of the aerodynamics of wing and winglet.
- d. The fourth chapter describes theory of calculations and mathematical modeling in details.
- e. The fifth chapter illustrates the details of experimental set up and procedures.
- f. The sixth chapter presents the experimental results and discussion on the important aspects of the results.
- g. Finally, the seventh chapter concludes the overall research and recommends few scopes for further research related to the present outcome.

LITERATURE REVIEW

2.1 Induced Drag Phenomena

In Aerodynamics, the four main forces which act on aircraft during the flight are Lift, Drag, Thrust and Weight. Drag is one of the most critical phenomena amongst all and is the opposing force of aircraft's forward motion. It could be classified briefly into parasite drag (not due to lift) and lift induced drag [2]. In a civil transport aircraft, frictional drag and induced drag together contributes more than 80% of the total drag as represented in Figure 2.2 [3], but the other forms of drag could not be excluded certainly.

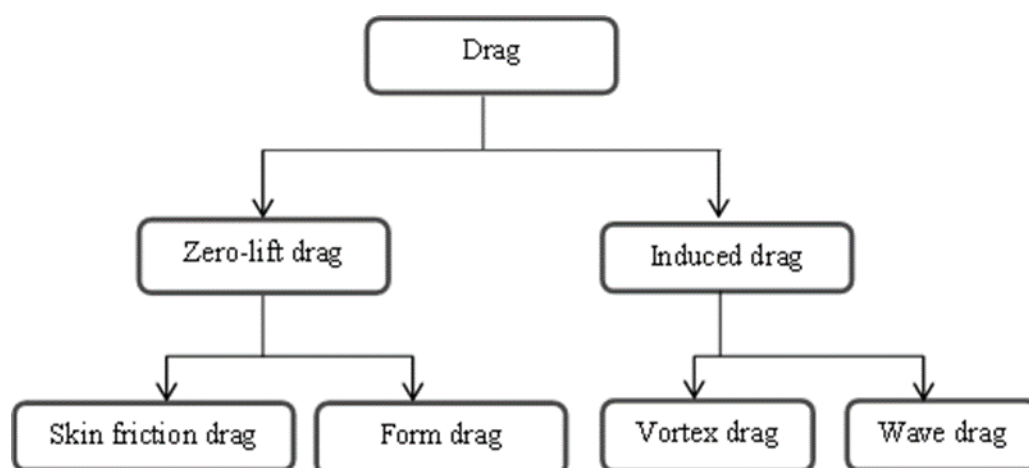


Figure 2.1: Different forms of Drag

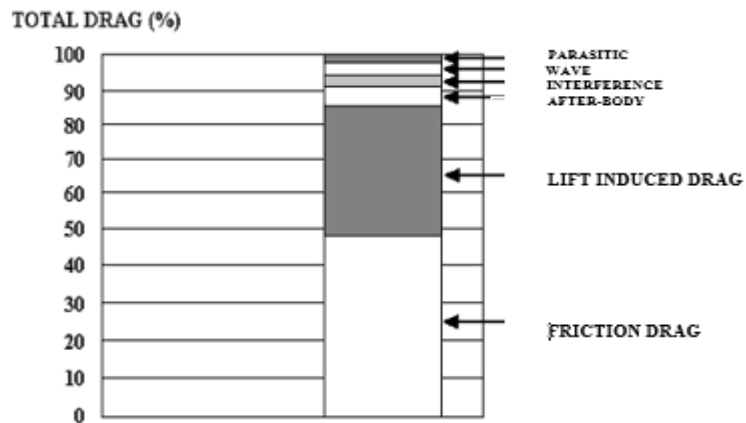


Figure 2.2: Distribution of Drag Components [3]

Induced drag produces kinetic energy which will cause the downward motion perpendicular to the airflow. This downward force could be recognized as the lift vector and this component is regarded as the induced drag [4]. Induced drag differs from the other forms of drag through a phenomenon of converting the dissipated kinetic energy into heat gradually. Vortex wake is a unique feature of induced drag. Mclean [4] has proposed the misinterpretations of the induced drag and the vortex wake produced by the wing. Normally the vortex wake is produced from the flow pattern due to the difference in velocities at upper and lower surface of an aircraft. It is shown in Figure 2.3 that the velocities at the down surface move towards the upper surface and thus it creates a circular flow pattern. This flow pattern is responsible for the vortex sheet that produced from the entire span of the wing.

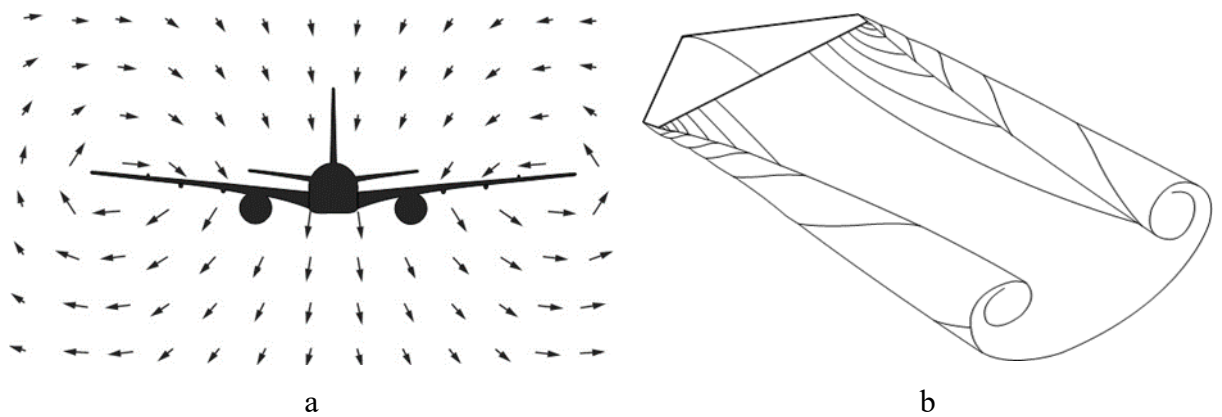


Figure 2.3: (a) Flow Pattern of the velocity (b) Vortex Sheet from Trailing Edge

[4]

Research has been conducted to reduce the induced drag and different methods have been developed to calculate this lift induced drag. One of the most talked about methods to reduce induced drag for a commercial jet transport aircraft is to incorporate wingtip devices and winglets at the wingtip of the wing which will be discussed in upcoming section.

2.2 History of Wingtip devices and Winglets

Endplate theory was the first to propose wingtip device and was patented by Fredrick W. Lanchester, British Aerodynamicist in 1897. Unfortunately, his theory could not reduce the overall drag of aircraft despite reducing the induced drag. The increase in the viscous drag during cruise conditions outruns the reduction in induced drag [5]. In July 1976, Dr. Whitcomb made a research at NASA Langley research center and developed the concept of winglet technology. According to Whitcomb, winglet could be described as the small wing like vertical structures which extends from the wingtip, aiming at reduction in induced drag when compared to other wing tip devices or extensions. He also claimed in his research that the winglet shows 20% reduction in induced drag when compared to tip extension and also improved lift-to-drag ratio [5].

In 1994 Aviation Partners Inc. (API) developed an advance design of winglet called blended winglet. Louis B. Gratzner from Seattle has the patent for blended winglet and invention of the winglet is to reduce the interference drag due to sharp edges as seen in the Whitcomb's winglet [6]. Also, Gratzner has the patent for the invention of spiroid-tipped wing in April 7, 1992 [7]. Later, "wing grid" concept was developed by La Roche from Switzerland in 1996 and got the patent for his invention [8]. The main purpose of all the above inventions was to decrease the strength of wake vortex and to reduce induced drag.

2.3 Types of Winglets and Wingtip devices

After the invention of winglet by Whitcomb, many types of winglets and tip devices were developed by aircraft designers. Some of the inventions of winglets by the respective aircraft manufacturer are discussed in the following section.

2.3.1 Blended Winglet

Blended winglet was developed by Grazter from Seattle in 1994. The unique design in this winglet has no sharp edge at the wing/winglet intersection and is followed by smooth curve. Aviation Partners Inc. (API) and Boeing Company made collaboration in 1999 for the design of advance blended winglets in 1999. Mike Stowell, Executive vice president of APB mentioned about the interference drag, an aerodynamic phenomenon caused due to intersection of lifting surfaces, hence the winglet design was developed to overcome the interference drag formed at the junction of wing and winglet. The winglets were retrofitted in Boeing business jets and also in B7371. Now these flights have their services in American airlines (Southwest airlines) and also in European airlines (Ryanair)¹.

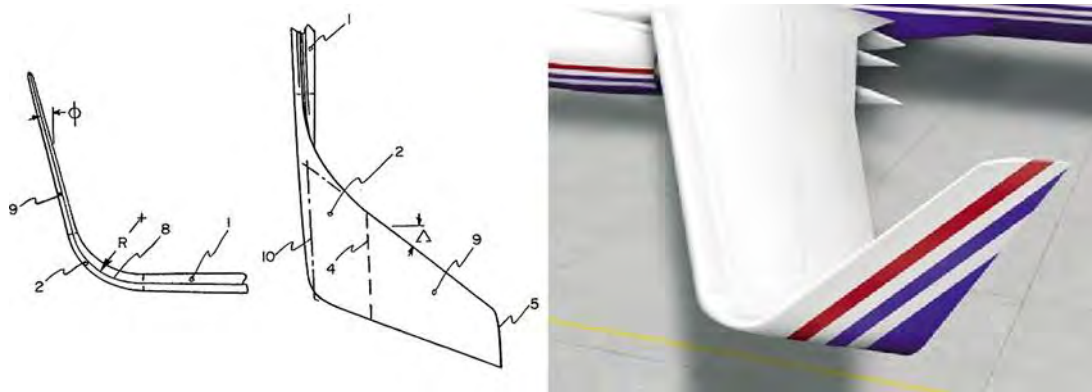


Figure 2.4: Blended Winglet [6]

¹ http://spinoff.nasa.gov/Spinoff2010/t_5.html

2.3.2. Spiroid Winglet

Gratzer has developed the spiroid-tipped wing technology and got the patent in 1992. One end of the spiroid tip is attached with forward part of the wing tip and continues to form a spiral loop which ends at the aft portion of the wing tip. Hence it looks oval shaped when viewed from front. Spiroid tipped wing was created to reduce the induced drag and also to reduce the noise effects associated with the tip vortices [7]. API has made their flight test in Dassault Falcon 50 with spiroid tipped wing.

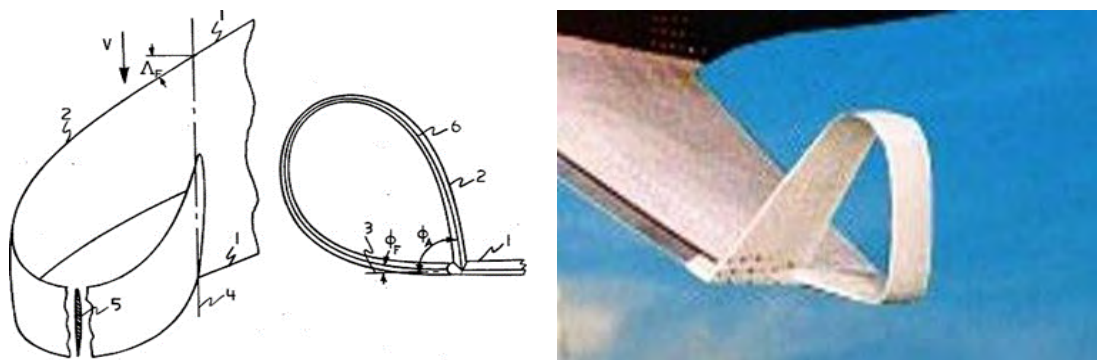


Figure 2.5: Spiroid Winglet [7]

2.3.3. Wing-Grid as Wing Tip

Wing grid geometry is defined by two or more wing like surfaces running parallel to each other from the end of wing section which forms the grid. La Roche from Switzerland held the patent for this invention since October, 1998. Instead of entire wing with no tip devices, wing grid at partial span could be replaced. La Roche claimed that wing grid could provide much reduction in induced drag when compared to wing span extension [8].

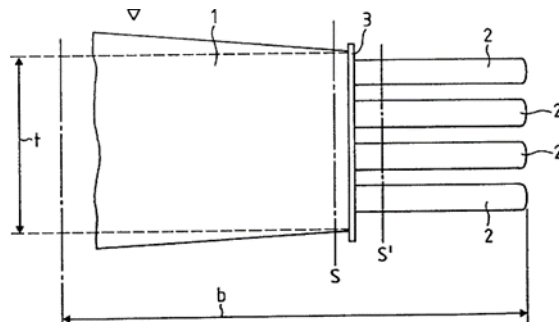


Figure 2.6: Wing Grids as Wing End Section [8]

2.3.4. Wing Tip Devices

Raked wing tip from Boeing Company was designed by Herrick and got the patent in 2000 [9]. The raked tip is attached with the main wingtip with higher angle of sweep than the main wing. Boeing 777 long-range jets have been designed with raked wingtip.



Figure 2.7: Raked Wing Tip [9]

Some of the conventional wingtips used in the aircrafts are mentioned in Figure 2.8.

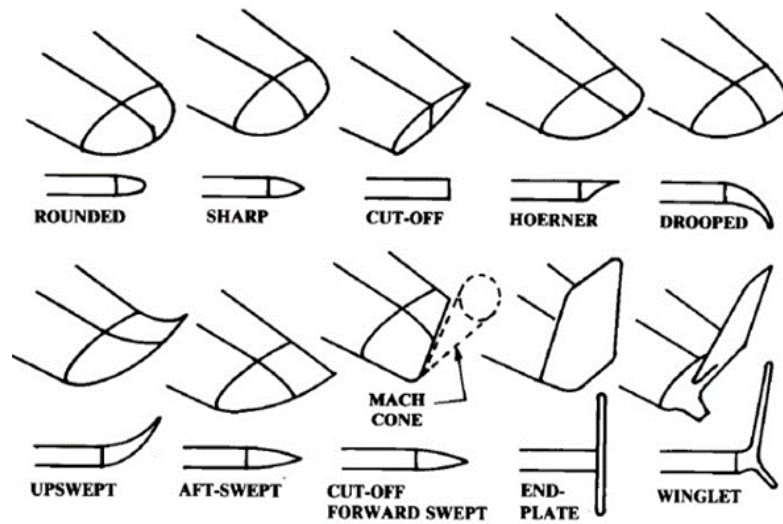


Figure 2.8: Different Types of Tip Devices [10]

2.4 Literature Survey

Ever since the winglet technology has been introduced, the advantages were being investigated. Dr. Whitcomb has performed an experiment with the winglet in which the winglet shows reduction in induced drag about 20%. In 1977, Heyson made an experiment to study the advantages of Whitcomb's winglet. His results indicate that winglets would reduce the induced drag more than tip extension and will be at its best when it is nearly vertical [11]. Later in 1980, Jones et al. [12] made a research in winglets to determine its effect over the induced drag using Trefftz-plane theory and concluded that the vertical length of the winglet should be twice than the length of horizontal extension in order to have its gain over tip extension.

Mostafa et al. [13] studied spiroid winglet, wing without winglet and simple winglet in order to make a performance comparison. This study proved that the spiroid was superior compared to other two wingtip configurations in terms of vortex suppression and overall drag reduction.

Ashrafi et al. [14] investigated the aerodynamic performance of wing with winglet using numerical simulation based on Control Volume Method. A comparison was

made among wing without winglet, simple winglet and semi-circular winglet based on aerodynamic features such as lift coefficient, drag coefficient, lift to drag ratio and tip vortices. It was found that semi-circular winglet showed best aerodynamic features.

Inam et al. [15] conducted an experiment on aircraft model with and without winglets at different Reynolds numbers. Experimental results showed that the drag decreased by 26~30% for wing with winglet compared to wing without winglet.

Bojja et al. [16] adopted a numerical approach to make comparison among wing without winglet, circular winglet and blended winglet. The results showed that the blended wing gave the better performance compared to others.

Azlin et al. [17] analyzed the aerodynamic characteristics of two winglets with semicircular and elliptical cross section at different angles of attack (AOA) through numerical simulation. It was found that elliptical winglet with 45° cant angle showed the best performance.

Raj et al. [18] studied spiroid winglets using numerical simulation software. The results showed that the spiroid winglet caused higher lift to drag ratio than wing without winglet.

Hossain et al. [19] conducted an experimental analysis for the aerodynamic characteristics of rectangular wing with and without bird feather like winglets for different Reynolds Number. The experimental result shows 25~30% reduction in drag coefficient and 10~20% increase in lift coefficient by using bird feather like winglet at 8° angle of attack.

Gall et al. [20] examined the possibility of improving aerodynamic characteristics of bi-plane by using winglets theoretically and experimentally. Both results indicated that the addition of winglets to biplane can increase the lift-curve slope.

Some researchers have worked on winglet cant angle [21-22] and found that 45° cant angle gave the higher lift force as well as lower drag force. Various numerical techniques have been developed instead of using commercially available simulation software to analyze the aerodynamic characteristic of winglet. Weierman et al. [23] conducted an investigation on winglet design and optimization for UAVs (Unmanned Aerial Vehicle) that operated on Reynolds numbers near 10⁶. A VLM (Vortex Lattice Method) and Matlab based Tornado VLM approaches were developed for designing and optimization of winglet.

Jain et al. [24] studied the effects of winglet on NACA 2415 aerofoil based wing using computational fluid dynamics (CFD). The authors compared wing with and without winglet by applying Spalart-Allmaras turbulence model for better accuracy around the boundary wall of wing. The computational simulation was carried out by ANSYS FLUENT with low Mach number of 0.23 at various angle of attack. It was found from the simulation that lift to drag ratio was increased by 2.5 percent due to the incorporation of winglet at the wingtip.

Dwivedi et al. [25] conducted an experimental investigation on three types of winglet such as blended winglet, bird feather like winglet and finlet. The wing and winglets were designed and analyzed using CATIA V6 and UNIFIGUREICS. The experimental analysis was carried out in a low subsonic flow at a speed of 40 meter per second and 25 meter per second by varying angle of attacks. This comparative study showed that the finlet was inclined to delay the stall, bird feather like winglet was efficient at low speed and overall the blended winglet was more efficient than the other two types of winglets.

Gavrilović et al. [26] analyzed five winglets such as spiroid 1 winglet, spiroid 2 winglet, blended winglet, wingtip fence and maxi winglet and studied their influence aircraft performance. The authors conducted the investigation through numerical simulation by using ANSYS Fluent. Moreover, Non-Dominated Sorting Genetic Algorithm- NSGA II in modeFRONTIER optimization software was used to determine an optimal one-parameter winglet configuration that simultaneously

minimizes drag and maximizes lift. It was found from the analysis that the lift to drag ratio increased up to 5.05 percent compared to the wing without winglet. It was also evident from the research that the amount of fuel saved could reach from 6000 tones up to 8000 tones depending on a chosen winglet.

Helal et al. [27] conducted a numerical investigation on a rectangular wing with NACA65-218 airfoil section while having a blended winglet at the wingtip. The numerical simulation was carried out by FLUENT where Spalart-Allmaras turbulence model was adopted for determination and estimation of aerodynamic characteristics of the wing at 0.2 Mach number. The results illustrated that the wing with winglet could increase lift to drag ratio by approximately 6% to 15% more than wing without winglet.

Panagiotou et al. [28] conducted a winglet optimization procedure for a Medium-Altitude-Long-Endurance (MALE) Unmanned-Aerial-Vehicle (UAV). The winglet optimization procedure was a part of the detail design phase. The flow around several winglet configurations was investigated, using CFD. Reynolds-Averaged-Navier–Stokes (RANS) were employed and coupled with the Spalart–Allmaras turbulence model. At first, only the flow around the wing-winglet part of the UAV was investigated, in order to determine the optimal design, by comparing the lift and drag coefficients, the lift-to-drag ratios, the stalling characteristics and the root bending moment. Then, the airflow around the entire aircraft was studied, at loiter conditions for the first and the optimal winglet configuration, in order to compare the overall UAV aerodynamic performance. The calculations showed a considerable improvement in the aircraft's aerodynamic performance after installing the optimized winglet; this in turn provided an increase in total flight time by approximately 10%.

Sidairi et al. [29] carried out a numerical simulation on the design and aerodynamic characteristics of winglets by using software such as CATIA- V5 and ANSYS. The results showed that fuel consumption was decreased by 3.8 percent and flight range was increased by 3.9 percent due to the addition of winglet at the wingtip.

Reddy et al. [30] conducted a numerical analysis on blended winglet and split winglet configuration using a Navier-Stokes solver on each configuration to obtain objective function. The multiobjective optimization was performed using modeFRONTIER. Results showed that a split winglet configuration diffuses the vortex core more effectively than a simple blended winglet. The split winglet configuration with the addition of scimitar tip spikes further increases the wing tip vortex core radius and better redirected the flow to reduce the induced drag. The Pareto optimized configuration was shown to have superior aerodynamic features over a range of aerodynamic angles of attack. That is, consistently lower drag and considerably lower moment, while having consistently higher lift and lift-to-drag ratio. This opens a possibility of optimizing split winglets with multiple elements mimicking a soaring bird's wing tip spread feathers.

Inaganti et al. [31] done a comparative numerical investigation of wings with and without winglet using Xflr5 software. A rectangular wing with Blended wingtip, Raked wingtip and winglet were investigated in this study. The results acquired from this analysis showed that the lift to drag ratio has increased by 4.33 percent for a wing with increased span whereas this ratio rose to 6.63 percent for a wing with winglet. This led to the conclusion that by increasing the span the aerodynamic efficiency increased and it was further increased by incorporating a wingtip device.

Cosin et al. [32] conducted an experimental investigations of wing-body half model with and without multi winglet at Reynolds number of $4 \cdot 10^5$. Multi winglets provided a potential improvement as it led to a significant increase in the performance parameters with a 7.3 percent gain in the maximum aerodynamic efficiency and 12 percent rise in climb factor. Aerodynamic characteristics of the multi winglets revealed improvements in the lift slope as well as expressive reduction of induced drag.

Hossain et al. [33] carried out an experimental investigation of wing with and without winglet at $1.7 \cdot 10^5$, $2.1 \cdot 10^5$ and $2.5 \cdot 10^5$ for different angle of attacks. Then

the authors applied fuzzy logic approach for the representation, manipulation and utilization of aerodynamic characteristics. The results developed with fuzzy logic was then compared with experimental results. The mean relative error of actual (from experiment) and predicted values (from FLS model) was found as 5.18 percent for the velocity of 26.36 m/s which was happened to be less than the acceptable limits (10%).

Numerous studies are being conducted throughout the as well on winglet designs alongside investigating the effect of winglets on wing aerodynamics. Continuous trial and error and optimization are being carried out to find out a winglet design with the highest reduction in induced drag while keeping the rise in profile drag as minimum as possible. Some of research regarding winglet design are mentioned below.

Ning et al. [34] performed an investigation on tip extensions, winglets and C-wings' design by combining the numerical optimization with conceptual wing design to find minimum drag. Results showed that at fixed lift, weight, and stall speed, the minimum drag trapezoidal tip device depends on the ratio of the maneuver lift coefficient to the cruise lift coefficient and C-wings have slightly lower drag compared with wings without winglet and wings with winglets when positive pitching moments are required about the aerodynamic center.

Jansen et al. [35] investigated a series of wing planform and winglets combination using single-discipline aerodynamic optimization and multidisciplinary aero structural optimization. A panel method and an equivalent beam finite element model are used to explore the wing and winglet models. It was found that when only aerodynamics is considered, closed lifting surface configuration, such as the box wing and joined wing are found to be optimal. But in case of aero structural optimization a winglet configuration is found to be optimal while considering the overall span is constrained.

Maughmer et al. [36] designed PSU 94-097 airfoil for use on winglets of high performance sailplanes. Later the author performed an experimental investigation as well as compared the experimental data with computer codes which were both were in good agreement with each other.

Chattot [37] done an investigation on the design and analysis of winglets from an aerodynamic point of view using XFOIL. It was found that viscosity had little effect on the optimal geometry but it had a significant effect in reducing the efficiency factor. The result also showed that the winglets generated a thrust which counteracts some of the friction drag of the winglets.”

Aviation Partners Boeing announced that their APB blended winglet has saved more than 2 billion gallons of fuel in 2010. APB also added that the winglets could save 5 billion gallons of fuel by 2014 which also represents the total reduction in carbon emission. Indeed, APB blended winglet on B737 showed increased in range of about 5-7% due to overall reduction in drag. In case of spiroid tipped wing, API has made a flight test on Gulfstream II in 1993 and they achieved more than 10% of fuel efficiency during the cruise conditions². Raked wingtip is a unique design for Boeing B777 family and it has improved the aircraft’s performance by reducing the take-off field length, improved fuel efficiency and good climb performance. Raked wing tip could provide 2 % reduction in fuel burn which is compensated by 1.3 million of fuel saving per year and 3.9 million of carbon-di-oxide emission per year³. Sharklets is the recent invention from the Airbus Company for their A320 family. They claimed that sharklets would reduce fuel burn up to 3.4% and this corresponds to 700 tons of carbon emission per aircraft in a year. Airbus also added that A320 could lift off with more weight due to the performance of sharklets⁴. The research made with spiroid tipped wing indicates that it would disperse the vortex effects within short span of time and therefore the time for take-off and landing between the aircrafts would be reduced [38].

² <http://www.aviationpartners.com/>

³ <http://www.boeing.com/commercial/777family/background/back4.html>

⁴ [http://www.airbus.com/newsevents/news-events-single/detail/first new-built-sharklet-equipped-a320-completed-in-toulouse/](http://www.airbus.com/newsevents/news-events-single/detail/first-new-built-sharklet-equipped-a320-completed-in-toulouse/)

Table 1: Boeing Series Advantages After Using Winglet⁵

Series	Range before	Range(Winglets)
B737-700	3250	3634
B737-800	2930	3060
B737-900	2670	2725

The above table shows that there was an increase in range when blended winglets were retrofitted.

2.5 Summary of the Literature Review

Conclusions from the studies of literature have shown that methods for improving aircraft efficiency are continually being investigated and aerodynamic drag reduction is a great challenge. The winglet concept appears to offer significant increases in aerodynamic and structural efficiency by reducing the lift-induced drag without overly penalizing wing weight. In airline industry, cost efficiency is the most important commercial consideration. Winglets lower drag and improve aerodynamic efficiency, thus reducing fuel burn. With a better fuel economy, airlines are able to offer more competitive ticket prices to the passengers. It is also evident from the studies that introducing winglet at the wingtip increases range and payload. In addition to that incorporating winglets at the wing tip has some environmental benefits such as reduction of noise effects produced from vortex effects and cutback the amount of carbon emission. Albeit all these advantages of winglet, it has some limitations as well. Winglets provide the greatest benefit when the wing tip vortex is strong, for this reason a low-aspect-ratio wing will see more advantage from the use of winglets than an already-efficient high-aspect-ratio wing.

⁵<http://www.b737.org.uk/winglets.htm>

2.6 Motivation of the Research Work

Literature review as discussed in chapter-2 reveals that researches on different wingtip devices like raked winglet, blended winglet, spiroid winglet have been carried out in many places in the world in an extensive way. But studies on the combination of specific wing shape with winglets and to reveal the mechanism behind the performance of wing with winglets are yet to be explored. Thus this investigation will make an effort to obtain the optimum performance of aircraft wing by combining specific wing shape with winglets.

2.7 Scope and Objectives of the Research

An experimental investigation will be carried out in the wind tunnel to study aerodynamics characteristics of curved trailing edge tapered wing. Further experiment will be carried out on curved trailing edge tapered wing with different kinds of winglets at the tips. At the end, the aerodynamic characteristics of all the wings will be analyzed and compared with each other to find out the best winglet design. Specific objectives are as follows:

- (i) To analyze the pressure distribution over the surfaces of wing with different types of winglets at the wingtip such as blended winglet, spiroid winglet, double blended winglet at different Angles of Attack.
- (ii) To study the aerodynamic characteristics (Coefficient of Pressure- C_p , Coefficient of Lift- C_L , Coefficient of Drag- C_D and Lift to Drag Ratio-L/D) from static pressure distributions of the wing models.
- (iii) To analyze and compare all the above characteristics with the variation of AOA.
- (iv) To reveal the mechanisms of improving aerodynamic characteristics like drag reduction.

AN OVERVIEW OF WING AND WINGLET AERODYNAMICS

3.1 Geometric Features of Wing

Wing is an aerodynamic structure that generates lift when comes into contact with moving air molecules i.e. wind. It may be considered as the most important component of an aircraft, since a fixed-wing aircraft is not able to fly without it. The main function of the wing of an aircraft is to generate lift force to make the flight possible in the air. This will be generated by a special wing cross section which is called airfoil. Wing is a three dimensional component, while the airfoil is two dimensional section as shown in Figure 3.1. The wing may have a constant or a non-constant cross-section across the wing [39]. Airfoils are basically replicas of wings that is much smaller in size. With the drag and lift values that are taken with airfoils, coefficients are calculated and since coefficients do not depend on wing size, larger wings can be produced.

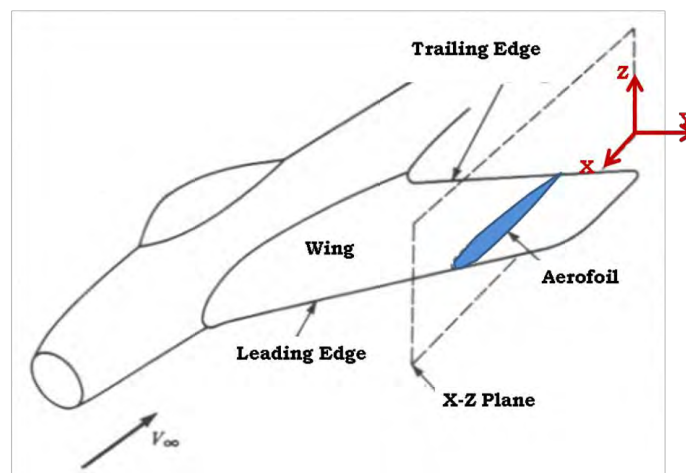


Figure 3.1: Wing and Aerofoil with Nomenclature [39]

The wing has a finite length called its wing span. If the wing is sliced with a plane parallel to the x-z plane of the aircraft, the intersection of the wing surfaces with that plane is called an airfoil. The wing is a 3D object, but it is usually treated as a set of two 2D geometric features; planform (x-y plane) and airfoil (x-z plane) as shown in Figure 3.2:

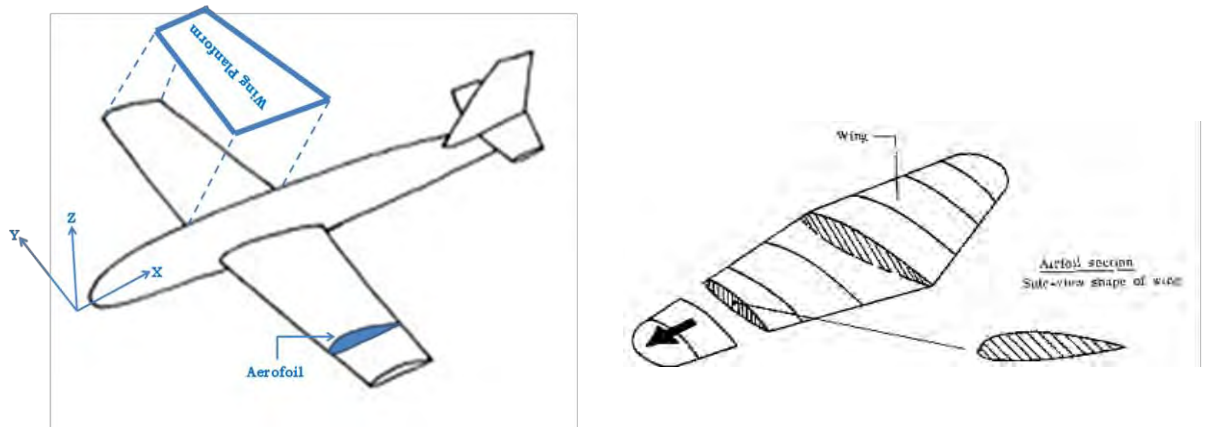


Figure 3.2: Geometric Features of a Typical Aircraft Wing [39]

3.2 Geometric Parameters of Wing

Aircraft wing can be defined by several geometric parameters such as span (b), wing surface area or planform (S), root chord (C_{root}), tip chord (C_{tip}) etc. as shown in Figure 3.3. Other important parameters are discussed below:

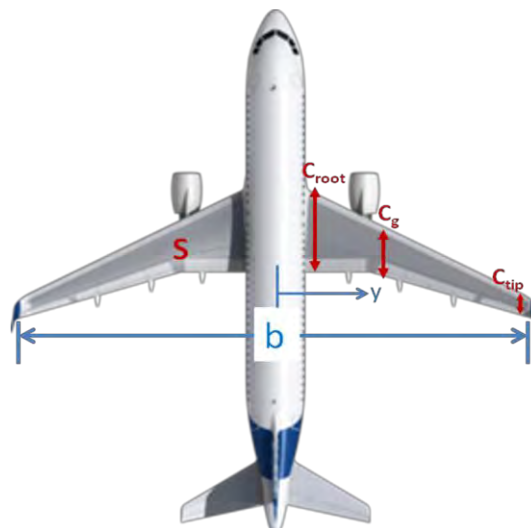


Figure 3.3: Wing Geometric Parameters [39,40].

3.2.1 Mean Geometric Chord (C_g)

The mean geometric chord is the chord of a rectangular wing having the same span and the same area as the original wing. It can be found for any general wing in the following way:

$$C_g = \frac{\int_0^{b/2} c(y) dy}{\int_0^{b/2} dy} = \frac{2}{b} \int_0^{b/2} c(y) dy = \frac{S}{b} \quad (3.1)$$

3.2.2 Mean aerodynamic chord (C_{MAC})

The mean aerodynamic chord is (loosely) the chord of a rectangular wing with the span, (not area) that has the same aerodynamic properties with regarding the pitching moment characteristics as the original wing. It can be found for any general wing in the following way:

$$C_{MAC} = \frac{\int_0^{b/2} [c(y)]^2 dy}{\int_0^{b/2} c(y) dy} = \frac{2}{S} \int_0^{b/2} [c(y)]^2 dy \quad (3.2)$$

3.2.3 Aspect ratio (AR)

The aspect ratio is the wing span divided by the mean geometric chord. It is a measure of how long and narrow a wing is. A square wing would have an aspect ratio of 1. Aspect ratio can be calculated in following ways:

$$AR = \frac{b}{C_g} = \frac{b^2}{S} \quad (3.3)$$

3.2.4 Taper ratio (λ)

It is the ratio of the tip chord to the root chord and is expressed as follows:

$$\lambda = \frac{C_{tip}}{C_{root}} \quad (3.4)$$

3.3 Fundamental Aerodynamics of Aerofoil

It is incredibly important to have a firm understanding of the theories involved in aerodynamic shape design for which purpose our emphasis begins with the foundations of aerodynamics.

3.3.1 The Kutta-Zhukowski Condition

The Kutta-Zhukowski Theorem predicts with remarkable accuracy the magnitude and distribution of the lift of airfoils up to angles of attack of 15 degrees. This theorem states that the force (L') experienced by a body in a uniform stream is equal to the product of the fluid density (ρ), stream velocity (V_∞), and circulation (Γ) and acts in a direction perpendicular to the stream velocity. Experiments have shown that when a body with a sharp trailing edge is set in motion, the action of the fluid viscosity causes the flow over the upper and lower surfaces to merge smoothly at the trailing edge; this circumstance, which fixes the magnitude of the circulation around the body, is termed the Kutta-Zhukowski Condition which may be summarized as follows: A body with a sharp trailing edge in motion through a fluid creates about itself a circulation of sufficient strength to hold the rear stagnation point at the trailing edge of finite angle to make the flow along the trailing edge bisector angle smooth. For a body with a cusped trailing edge where the upper and lower surfaces meet tangentially, a smooth flow at the trailing edge requires equal velocities on both sides on the edge in the tangential direction.

The flow around an airfoil at an angle of attack in an inviscid flow develops no circulation and the rear stagnation point occurs on the upper surface as can be seen by Fig. 3.4. Fig. 3.5 is a sketch of the streamlines around an airfoil in viscous flow, indicating the smooth flow past the trailing edge, termed the Kutta-Zhukowski Condition. This Condition has served as the basis for the calculation of forces around an airfoil.

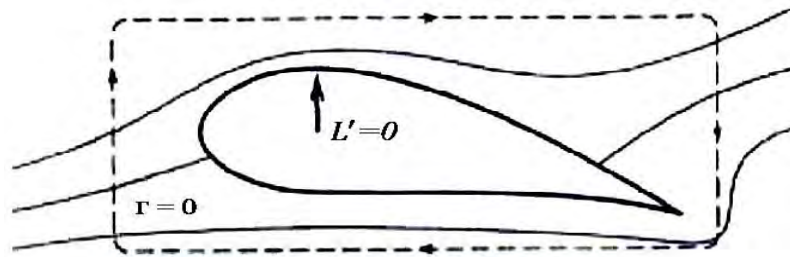


Figure 3.4: Kutta-Zhukowski Condition, No Viscosity

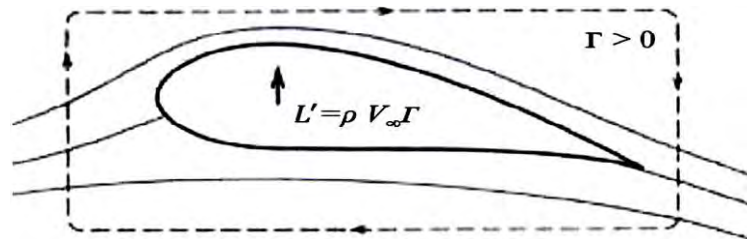


Figure 3.5: Kutta-Zhukowski Condition, Viscosity

Based on the Helmholtz laws however, the circulation around an airfoil and its „wake“, being zero before the motion began, must remain zero. The establishment of the Kutta Condition, therefore, requires the formation of the so-called starting vortices (see Fig.3.6) with a combined circulation equal and opposite to that around the airfoil. The induced flow caused by the vorticity of the airfoil, added to that caused by the starting vortices in the wake, will be just enough to accomplish the smooth flow at the trailing edge.

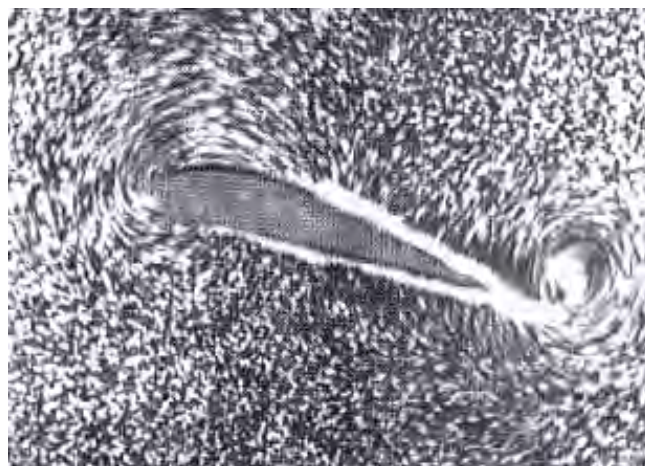


Figure 3.6: Starting Vortices

The starting vortices are left behind as the airfoil moves farther and farther from its starting point, but during the early stages of the motion, Figure 3.6 indicates that their induced velocities assist those induced by the surface vortices, to satisfy the condition. It follows that the surface vortex and as a result, the forces acting on the airfoil, will not be as strong in the early stages. They are being influenced by the starting vortices, and they are also being influenced after the flow is fully established. Then the surface vortices must be strong enough by itself to move the rear stagnation point to the trailing edge. Simultaneously, notice the increase in airspeed around the leading edge, as indicated in Figure 3.6. The resulting pressure decrease manifests a „leading edge suction“ phenomena by which two opposing pressure vectors are located adjacent to each other.

A typical pressure distribution of an airfoil is shown in Figure 3.7, the arrows representing pressure vectors. In a perfect fluid, the total force on the airfoil is the lift ρV_∞ acting normal to V_∞ . Its magnitude can be represented as the resultant of two components, one normal to the chord line of magnitude $\rho V_\infty \cos \alpha$, given by the integral over the chord of the pressure difference between points y_l and y_u on the lower and upper surfaces, and the other parallel to the chord line of magnitude $\rho V_\infty \sin \alpha$, representing the leading edge suction. In a real fluid, viscous effects alter the pressure distribution and friction drag is generated, though at low angles of attack the theoretical pressure distribution can be taken as a valid approximation.

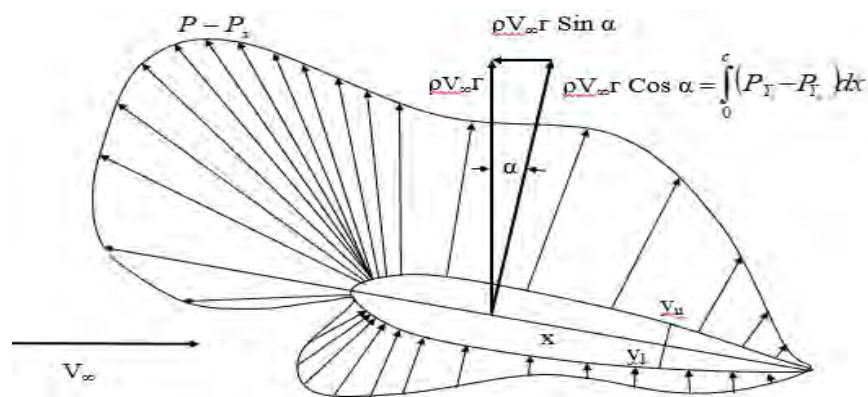


Figure 3.7: Airfoil Pressure Distribution

3.3.2 Aerodynamic Characteristics of Aerofoils

The history of the development of airfoil shapes is long and involves numerous contributions by scientists from all over the world. By the beginning of the twentieth century the methods of classical hydrodynamics had been successfully applied to airfoils, and it became possible to predict the lifting characteristics of certain airfoil shapes mathematically. In 1929, the National Advisory Committee for Aeronautics (NACA) began studying the characteristics of systematic series of airfoil in an effort to determine exact characteristics. The airfoils were composed of a thickness envelope wrapped around a mean chamber line as shown by Fig.3.8. The mean chamber line lies halfway between the upper and lower surfaces of the airfoil and intersects the chord line at the leading and trailing edges.

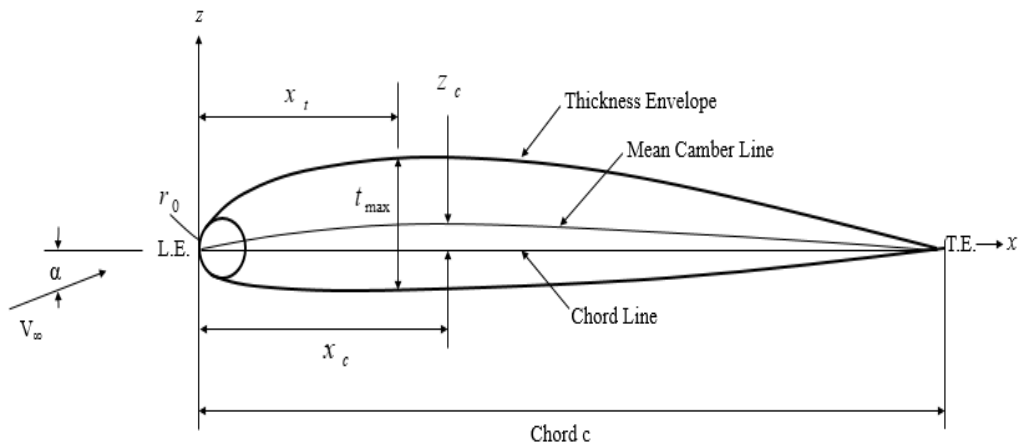


Figure 3.8: Airfoil characteristics

The various families of airfoils are designed to show the effects of varying the geometrical variables on their aerodynamic characteristics such as lift, drag and moment, as functions of the geometric angle of attack. The geometric angle of attack α is defined as the angle between the flight path and the chord line of the airfoil as shown in Figure 3.9. The geometrical variables include the maximum camber z_c of the mean chamber line and its distance x_c behind the leading edge, the maximum thickness t_{\max} and its distance x_t behind the leading edge, the radius of curvature r_0 of the surface at the leading edge, and the trailing edge angle between the upper and

lower surfaces at the trailing edge. Theoretical studies and wind tunnel experiments show the effects of these variables in a way to facilitate the choice of shapes for specific applications.

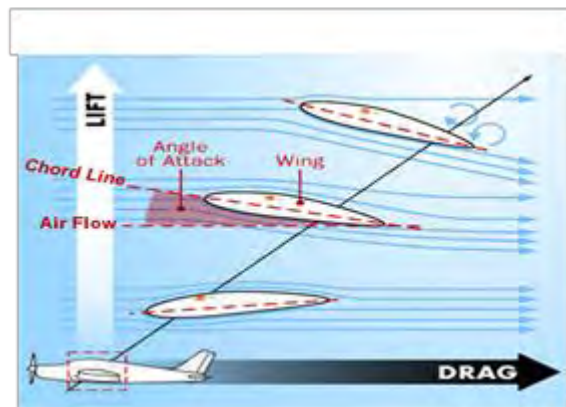


Figure 3.9: Aerodynamic Characteristics of Aircraft Wing [39, 40].

The lifting characteristics of an airfoil below stall conditions are negligibly influenced by viscosity and the resultant of the pressure forces on the airfoil is only slightly altered by the thickness envelope provided that the ratio of maximum thickness to chord $\frac{t_{\max}}{c}$ and the maximum mean chamber z_c remain small, and the airfoil is operating at a small angle of attack. These conditions are usually met during standard operations of airfoils. In a real fluid, lift is within 10% of theory for inviscid fluids up to an angle of attack of $\alpha_{L_{\max}}$ of 12 to 15° depending on the geometric factors of Figure 3.10. shows that at these low angles the streamlines follow the surface smoothly, although particularly on the upper surface the boundary layer causes some deviation. At angles of attack greater than $\alpha_{L_{\max}}$, called the stalling angle, the flow separates on the upper surface and the Kutta-Zhukowski Condition no longer holds and large vortices are formed. At these angles, the flow becomes unsteady and there is a dramatic decrease in lift, accompanied by an increase in drag and large changes in the moment exerted on the airfoil by the altered pressure distribution.

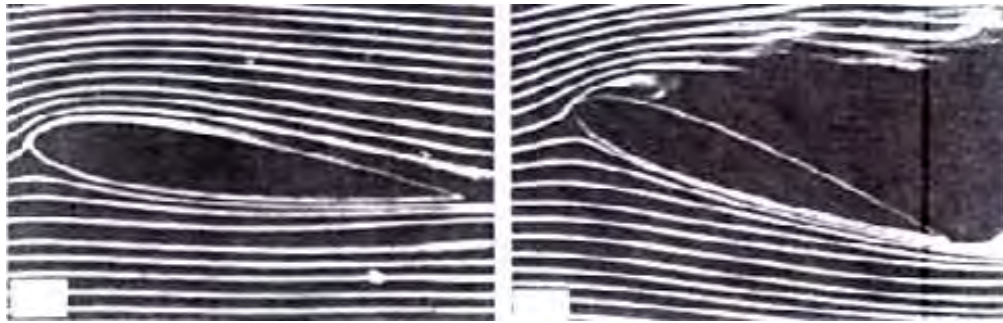


Figure 3.10: Flow around an airfoil

The lift force increases almost linearly with angle of attack until a maximum value is reached, whereupon the wing is said to stall. The variation of the drag force with angle of attack is approximately parabolic. It is desirable for the wing to have the maximum lift and smallest possible drag i.e. the maximum possible lift to drag ratio. The variation of all these aerodynamic characteristics (lift force, drag force and lift to drag ratio) with angle of attack for a typical aircraft are shown in Figure 3.11.

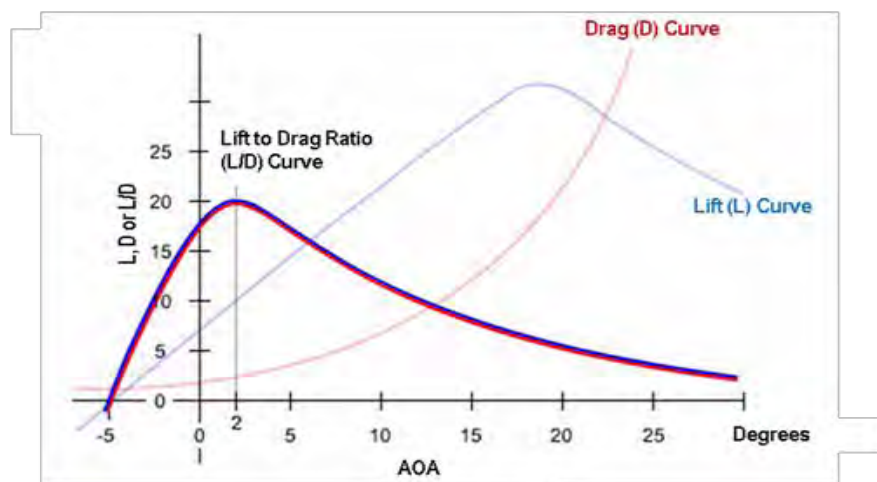


Figure 3.11: Variation of Aerodynamic Characteristics with Angle of Attack [39]

3.3.3 Lift and Drag Coefficient of Airfoil

The lift and drag generated by an airfoil are usually measured in a wind tunnel and published as coefficient which are dimensionless. These are mainly the variations of non-dimensional lift and drag relative to angle of attack [41, 42]. Two aerodynamic

forces (lift and drag) are usually non-dimensional by dividing them to appropriate parameters as follows:

$$\text{Lift Coefficient, } C_L = \frac{L}{\frac{1}{2}\rho V_\infty^2 S} \quad (3.5)$$

$$\text{Drag Coefficient, } C_D = \frac{D}{\frac{1}{2}\rho V_\infty^2 S} \quad (3.6)$$

Where, L and D are the lift force and drag force respectively.

S is the Planform area=Chord \times Span.

V_∞ is the free stream air velocity.

$\frac{1}{2}\rho V_\infty^2$ is the dynamic pressure and ρ is the density of air

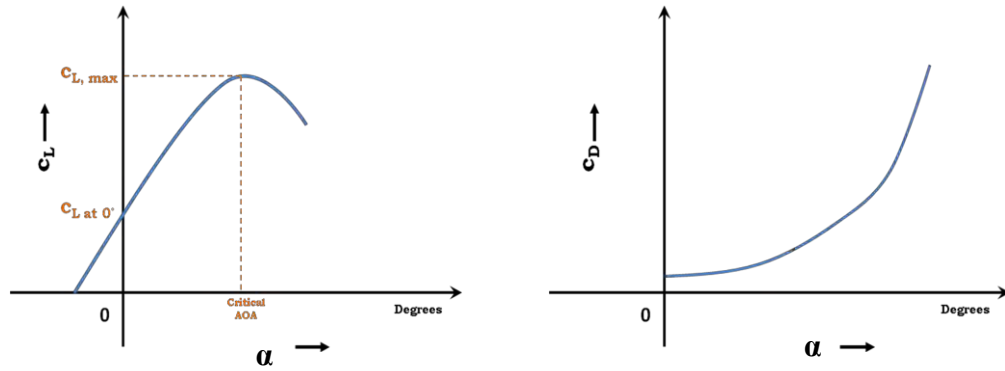
Another important parameter, the lift-to-drag ratio (L/D) is the amount of lift generated by an airfoil, divided by the drag it creates by moving through the air. An airplane has a high L/D if it produces a large amount of lift or a small amount of drag. A higher or more favorable L/D is typically one of the major goals in aircraft design.

$$\text{Ratio} = \frac{\text{Lift}}{\text{Drag}} = \frac{L}{D} \quad (3.7)$$

Thus, the performance and characteristics of an airfoil may be evaluated by looking at the following graphs:

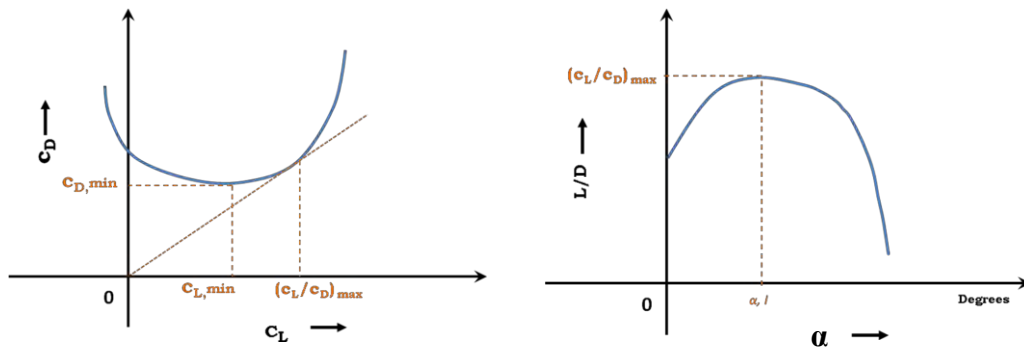
- a. The variations of lift coefficient (C_L) with angle of attack (α).
- b. The variations of drag coefficient (C_D) with angle of attack (α).
- c. The variations of drag coefficient (C_D) with lift coefficient (C_L).

d. The variations of lift-to-drag ratio (L/D) with angle of attack (α).



a. c_L vs α graph

b. c_D vs α graph



c. c_D vs c_L graph

d. L/D vs α graph

Figure 3.12: Graphs of Different Parameters of Aerofoil [39, 40]

3.3.4 Aerofoil Data Sources

Selection of a proper airfoil is possible from the previously designed and published airfoil sections. Two reliable airfoil resources are NACA and Eppler. The details of Eppler airfoils have been published in [43]. NACA airfoils have been published in a book published by Abbott and Von Doenhoff [44]. Eppler airfoil names begin with the letter “E” followed by three numbers. In general, the Eppler airfoils are for very low Reynolds number, Wortman airfoils for low (sailplane-ish) Reynolds number, and

the NASA Low-Speed airfoils (e.g. LS(1)-0413) and Mid Speed Airfoils e.g. MS(1)-0313) are for “moderate” Reynolds numbers [41].

3.3.5 NACA Aerofoils

The NACA airfoils are airfoil shapes for aircraft wings developed by the National Advisory Committee for Aeronautics (NACA). Airfoils are described and can be distinguished between each other by the numbers that follow the acronym NACA. There are six NACA families which are 4-Digit, 5-Digit, 6-Series, 7-Series, 8-Series and 16-Series. In NACA Four Digit Series, there are four digits that follow the acronym NACA and these 4 digits show 3 different properties of the airfoil. The first family of airfoils designed in the above mentioned way is known as the NACA Four-Digit aerofoils. The explanation of the 4-digit NACA aerofoil is as follows [41, 45]:

- a. The first digit specifies the maximum camber in percentage of the chord.
- b. The second digit indicates the position of the maximum camber in tenths of chord.
- c. The last two digits provide the maximum thickness of the airfoil in percentage of chord.

For example, the NACA 4412 airfoil chosen for this research has a maximum thickness of 12% with a camber of 4% located 40% back from the airfoil leading edge.

3.3.6 Co-ordinates of NACA Airfoils

One of the most reliable resources and widely used data base is the airfoils developed by National Advisory Committee for Aeronautics, NACA (predecessor of NASA) in 1930s and 1940s. The Cambered airfoil sections of all NACA families are obtained by combining a mean line and a thickness distribution [41].

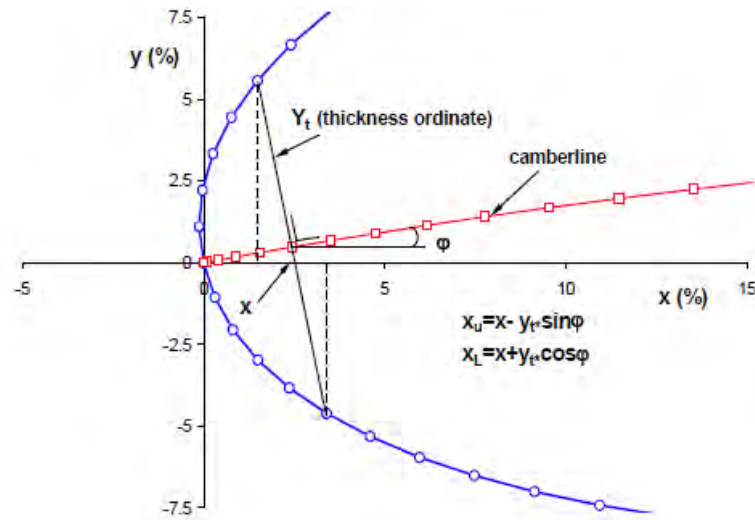


Figure 3.13: NACA Aerofoil Co-ordinates [41].

The abscissas, ordinates and slopes of the mean line are designated as x_c , y_c and $\tan \theta$ respectively. If x_u and y_u represent the abscissa and ordinate of a typical point of the upper surface of the airfoil and y_t is the ordinate of the symmetrical thickness distribution at the chord wise position x , the upper and lower surface coordinates are given by the following relations (u denotes upper surface and l denotes lower surface):

$$x_u = x - y_t(x) \sin \theta \quad (3.8)$$

$$y_u = y_c(x) + y_t(x) \cos \theta \quad (3.9)$$

$$x_l = x + y_t(x) \sin \theta \quad (3.10)$$

$$y_l = y_c(x) - y_t(x) \cos \theta \quad (3.11)$$

Where, $y_t(x)$ is the thickness function

$y_c(x)$ is the camber line function

$\tan \theta = \frac{dy_c}{dx}$ is the slope of camber line

3.4 The Finite Wing

It has been shown that, from momentum considerations, a vortex which is stationary with respect to a uniform flow experiences a force of ρV_∞ magnitude in a direction perpendicular to V_∞ , also known as the Kutta-Zhukowski Condition. It follows that a stationary line vortex normal to a moving stream is equivalent of an infinite wingspan, an airfoil, from resultant force calculations. The airfoil-vortex analogy forms the basis for calculating the properties of the finite wing. However, since the lift and therefore the circulation, is zero at the tips of a wing of finite span and varies throughout the wing span, additional flow components must be considered. This section is devoted to this address these concepts.

3.4.1 Flow Field around Finite Wings

Considering a wing of span b in a uniform flow velocity V_∞ represented by a bound vortex AB of circulation (see Figure 3.14). According to the Kutta-Zhukowski Condition, a force having magnitude ρV_∞ will be exerted onto the vortex in a direction perpendicular to V_∞ . Helmholtz Laws however, require that the bound vortex cannot end at the wingtips as it must form a complete circuit, or it must extend to infinity or a boundary of the flow. Adjunctively, it has been shown that these laws further require that at the beginning of the motion a starting vortex (CD , Figure 3.14) of strength equal to and opposite to that of the bound vortex, be formed. The Vortex Laws are satisfied by including the trailing vortices BD and AC of strength.

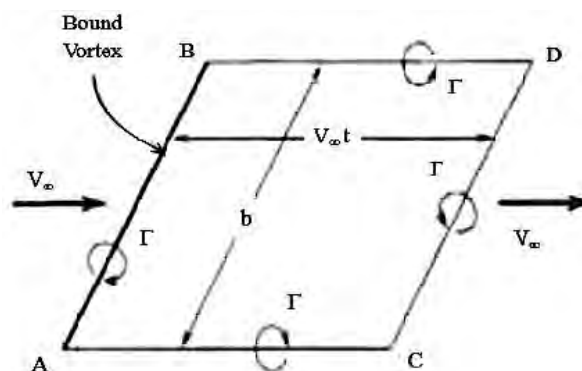


Figure 3.14: Vortex Configuration

The resulting velocity field is comprised of the uniform flow V_∞ with a superimposed downward flow within the rectangle ABCD and an upward flow outside it. This flow, however, is unsteady as the starting vortex moves downstream with the flow, and the trailing vortices AC and BD are therefore increasing in length at the rate V_∞ .

Note first, that the velocity induced by a given vortex varies with the reciprocal of the distance from the vortex. Therefore, as time goes on, the starting vortex recedes from the wing position and, soon after the start the velocities it induces at the wing are negligible compared with those induced by portions of the trailing vortices near the wing. In practice, $b \ll V_\infty t$ for steady flight and the configuration becomes essentially an elliptical vortex fixed to the wing and extending to infinity.

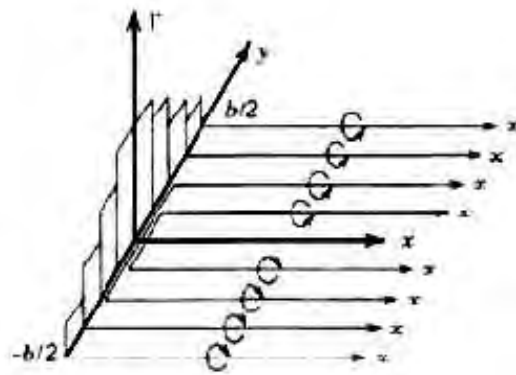


Figure 3.15: Superposition of elliptical vortices in steady flow

Actual finite wings are made up of a superposition of elliptical vortex elements of various strengths (see Figure 3.15). An infinite number of these elements lead to a continuous distribution of circulation and therefore of the lift as a function of y extending over $-b/2 < y < b/2$. In steady flight, the vortices will in general be symmetrically placed. The trailing vortex lines lying on the xy plane form a vortex sheet of width b extending from the trailing edge of the wing to infinity.

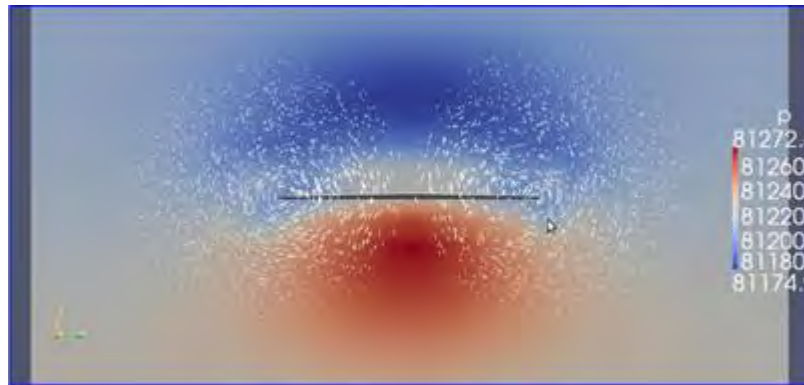


Figure 3.16: Formation of trailing vortices at wing tips

From a physical standpoint, Figure 3.16 can help visualize the formation of trailing vortices. The flow field that develops as the consequence of the circulation around the wing is initiated by an under pressure (-) over the upper surface and an overpressure (+) over the lower surface.

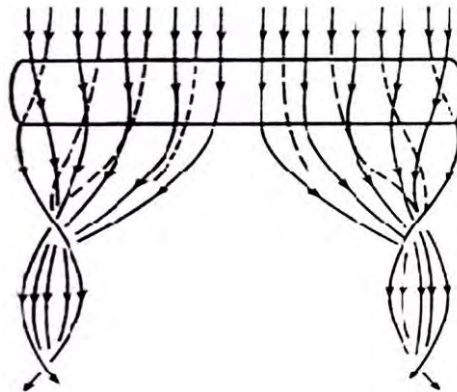


Figure 3.17: Wing tips flow vortices

The indicated flow from high to low pressure at the wing tips signifies the formation of the trailing vortices. In terms of the Vortex Laws and the Kutta-Zhukowski Condition, the formation of the trailing vortices can be expressed as follows: The circulation about the wing is generated as the consequence of the action of viscosity in establishing the Kutta Condition at the trailing edge. The boundary layer that forms adjacent to the surface is a rotational flow resulting from the viscous shearing action; the rotating fluid elements spill over the wing tips at the rate required to for trailing vortices with circulation equal to that around the wing. After leaving the wing tips, the

trailing vortices follow the streamlines of the flow and, in conformity with the Vortex Laws, the circulation around them remains constant.

Trailing vortices may become visible in the presence of dust and moisture. Figure 3.18 is a photograph of an airplane emitting insecticide dust from its trailing edge. It shows that, because of the influence of the vortex line, the trailing vortex sheet will roll up along the edge to form a concentrated vortex which can be clearly seen in Figure 3.18.

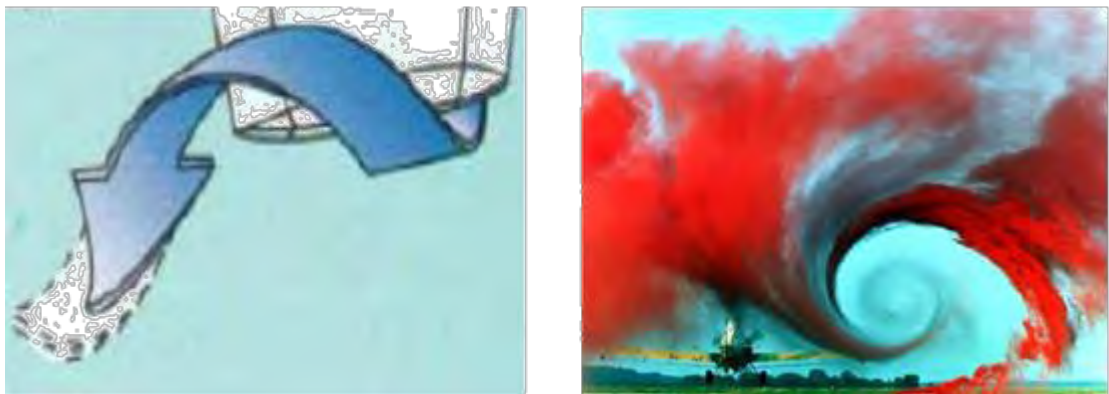


Figure 3.18: Formation of trailing vortices at wing tips

3.4.2 Downwash and Induced Drag

The main problem of finite-wing theory is the determination of the distribution of airloads on a wing of given geometry flying at a given speed and orientation in space. The analysis is based on the assumption that the trailing vortex sheet (see Figure 3.18) remains undeformed and that at every point along the span, the flow is essentially two dimensional.

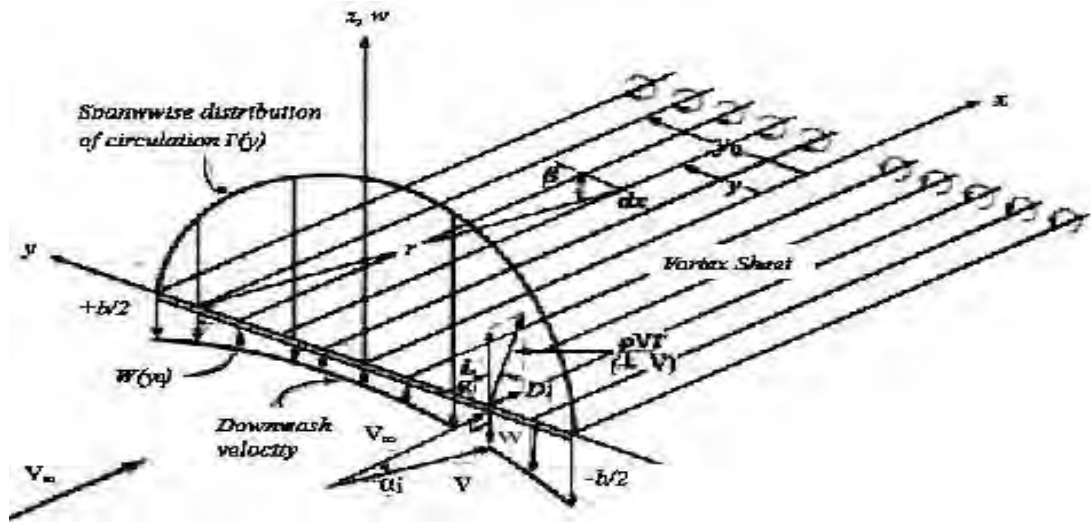


Figure 3.19: Downwash velocity w induced by trailing vortices.

Notice that the bound vortex with circulation varying along the span represents a wing for which the center of pressure at each spanwise point lies on the y axis. The lift distribution is continuous and the trailing vortices therefore form a vortex sheet of total circulation zero, since the flow field is that of an infinite number of infinitesimally weak elliptic vortices, with the cross section of each being a vortex pair of zero total circulation. The trailing line vortices are assumed to lie in the $z = 0$ plane and to be parallel to the x axis therefore, the effect on the flow at a given point on the bound vortex is therefore a downwash w , whose magnitude at each point is given by the integrated effect of the circulation distribution on the semi-infinite vortex sheet over the range $-b/2 < y < b/2$ (see Figure 3.19). The resultant velocity V at the wing has two components V_∞ and $w(y)$ at each point. These define the induced angle of attack:

$$\alpha_i(y) = \tan^{-1} \frac{w}{V_\infty} \quad (3.12)$$

By the Kutta-Zhukowski Condition, the force on the bound vortex per unit span has the magnitude ρV and is normal to V , that is inclined to the z axis at an angle of α_i . This force has a lift component normal to V_∞ given by

$$L' = \rho V \cos \alpha_i = \rho V_\infty \quad (3.13)$$

and a drag component, termed the induced drag

$$D'_i = -\rho V \sin \alpha_i = -\rho w \quad (3.14)$$

In most practical applications the downwash is small, that is $|w| \ll V_\infty$. It follows that α_i is a small angle and the above formulas become

$$\alpha_i(y) = \frac{w}{V_\infty} \quad (3.15)$$

$$D'_i = -L' \alpha_i \quad (3.16)$$

Notice that the induced drag D'_i is a component of the Kutta-Zhukowski force in the direction of V_∞ that is the plane of flight.

Although the trailing vortex sheet induces a downwash along the span of a lifting wing, it also induces an up wash velocity field in the regions beyond the wing tips. When another wing flies in such a region, the incoming flow is effectively skewed up by the up wash so that the resultant aerodynamic force will cause a forward thrust instead of a backward drag on the second wing. This phenomenon can be noticed in our daily lives for flying birds. Flock of birds flying in V-shaped formations take advantage of this effect and studies have shown that in proper configurations, savings higher than 50% in the total power required for flight can be achieved as compared to that when birds fly far apart at the same speed.

In order to calculate the downwash and induced angle of attack at a wing section, we will be referring to Figure 3.20 which represents the essential features of Figure 3.18, shown from the top view of the $z = 0$ plane. Notice that the downwash is assumed to be positive outward.

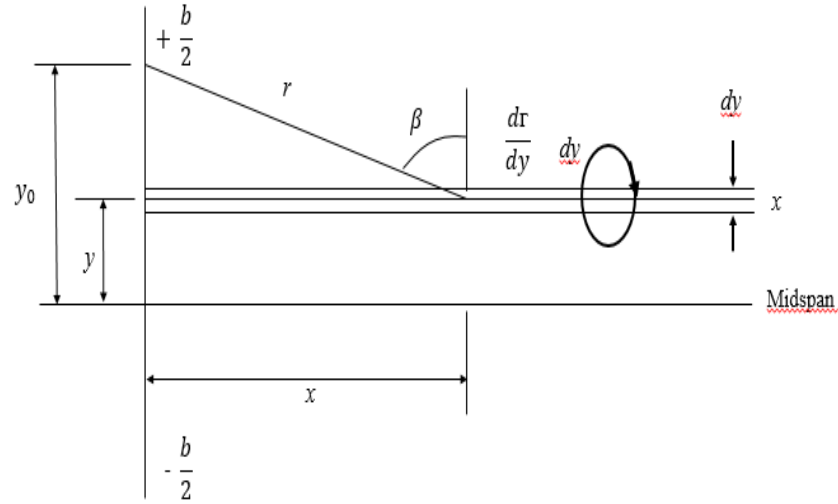


Figure 3.20: Downwash contribution from trailing vortex filament

By means of the Biot-Savart Law we can express the increment of downwash at the point $(0, y_0)$ induced by the element dx of the vortex filament of strength extending from $(0, y)$ to infinity ∞ in the $+x$ direction. The entire contribution of the vortex filament at y to the downwash is

$$w_{y_0, y} = -\frac{d}{4\pi} \int_0^{\infty} \frac{\cos \beta dx}{r^2} = -\frac{d}{4\pi} \frac{1}{y_0 - y} \quad (3.17)$$

The total downwash w_{y_0} at y_0 is the sum of the contributions of dw_{y_0} from all parts of the vortex sheet. Thus after integrating and dividing by V_{∞} we obtain the induced angle of attack for the wing section at the spanwise location y_0 :

$$\alpha_i(y_0) = \frac{w_{y_0}}{V_{\infty}} = -\frac{1}{4\pi V_{\infty}} \int_{-\frac{b}{2}}^{\frac{b}{2}} \left(\frac{d}{dy} \right)_{wing} \frac{1}{y_0 - y} \quad (3.18)$$

This equation gives the amount by which the downwash alters the angle of attack of the wing as a function of the coordinate y_0 along the span.

3.4.3 The Fundamental Equations of Finite-Wing Theory

The fundamental equations needed to find the circulation distribution for a finite wing are expressed as the equations connecting three angles: α_a , the absolute angle of attack (see Fig. 3.21) that is the angle between the direction of the flow for zero lift (Z.L.L.) at a given y_0 and the flight velocity vector V_∞ the induced angle of attack α_i , and the effective angle of attack α_0 .

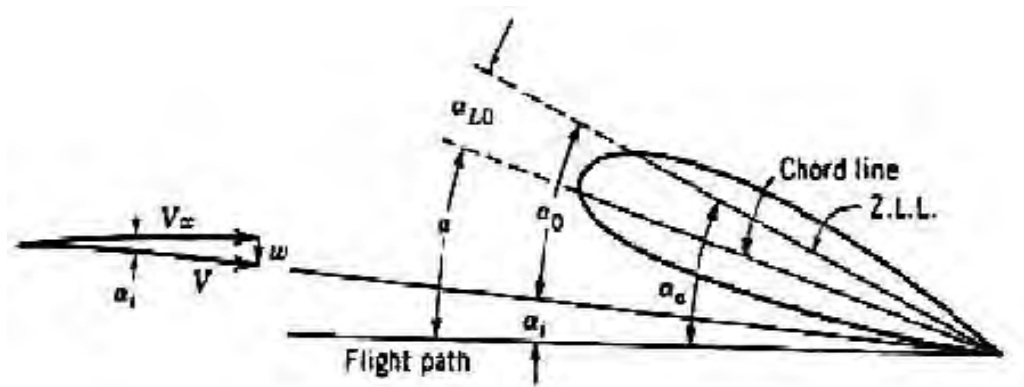


Figure 3.21: Finite wing Theory parameters

These equations are

$$\alpha_a = \alpha_0 - \alpha_i = \alpha - \alpha_{L0} \quad (3.19)$$

The effective angle of attack sectional lift coefficient is a section property and thus must satisfy the equation for

$$c_l = m_0 \alpha_0 \quad (3.20)$$

Where $m_0 = 2\pi$ according to thin wing theory. The meaning of $m_0 \alpha_0$ for a finite wing is shown in the figure below.

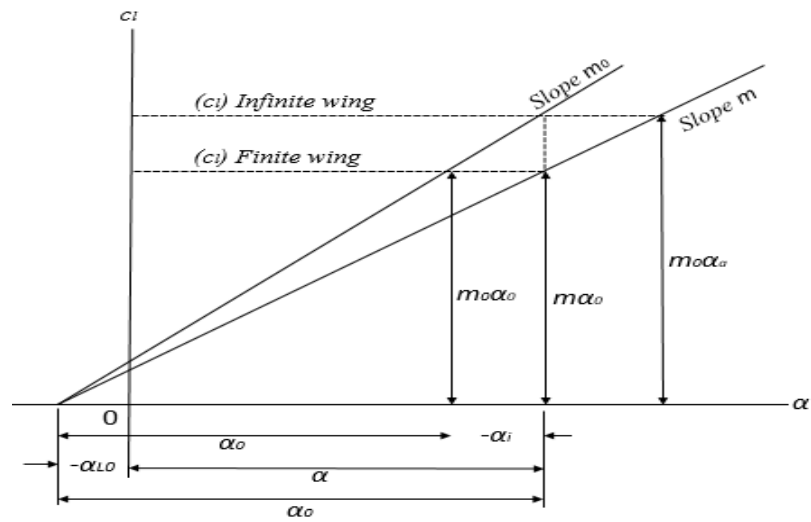


Figure 3.22: Finite wing Theory representation

If the airfoil section were on a wing of infinite span, the sectional lift coefficient there would have a higher value of $m_0\alpha_0$. Therefore, since the absolute angle of attack is determined by wing geometry, the sectional lift coefficient of a finite wing can be expressed as

$$c_l = m\alpha_a \quad (3.21)$$

Where m is a function of m_i . The relation between m_0 and m is given by

$$m = \frac{m_0}{1 - \frac{\alpha_i}{\alpha_0}} \quad (3.22)$$

Notice that $m \leq m_0$ for $c_l > 0$. The absolute angle of attack can therefore be derived by first writing

$$L' = \rho V_\infty^2 c = m_0 \alpha_0 \frac{1}{2} \rho V_\infty^2 c \quad (3.23)$$

from which,

$$\alpha_0 = \frac{2}{m_0 V_\infty c} \quad (3.24)$$

Where c is the chord length of the airfoil (see Figure 3.8).

This equation indicates that the sectional circulation on a finite wing, which is proportional to α_0 , is smaller than that of a wing of infinite span, which is proportional to α_a , because of the induced angle of attack α_i caused by the downwash (see Fig.3.20). Then the fundamental equation in its final form is

$$\alpha_a(y_0) = \left(\frac{2}{m_0 V_\infty c} \right) y_0 + \frac{1}{4\pi V_\infty} \int_{-\frac{b}{2}}^{\frac{b}{2}} \frac{\left(\frac{d}{dy} \right)_{wing}}{y_0 - y} \quad (3.25)$$

The only unknown in the above equation is the circulation, and its solution for all span wise locations y_0 solves the air load distribution problem for a given wing. Unfortunately, its solution can only be obtained for only a few special cases, the most important of these, the elliptical lift distribution.

3.4.4 The Elliptical Lift Distribution

Equation (above) is readily solved if the distribution is assumed to be known and the chord distribution $c(y)$ is taken as the unknown. This problem of finding a chord distribution that corresponds to a given circulation distribution simply involves the solution of an algebraic equation. A very important case is the elliptical circulation distribution, for this distribution represents the wing of minimum induced drag. Fortunately, the properties of wings of arbitrary planforms that do not differ radically from the most common shapes are close to those of the elliptical wing. It is therefore customary to write the properties of wings of arbitrary planforms in terms of the properties of the elliptical wing and a correction factor.

If Γ represents the circulation in the plane of symmetry, the elliptical variation of circulation with span is written

$$= \Gamma \sqrt{1 - \left(\frac{y}{b/2}\right)^2} \quad (3.26)$$

Then the induced angle of attack becomes

$$\alpha_i = \frac{-\Gamma}{2bV_\infty} \quad (3.27)$$

Which indicates that α_i at any point along the lifting line is constant if the distribution is elliptical. Therefore, if the absolute angle of attack α_a at every spanwise location is the same then the effective angle of attack α_a is also constant. Thus,

$$c_l = m_0 \alpha_0 \quad c_{di} = \frac{D_i}{q_\infty c} = -c_l \alpha_i \quad (3.28)$$

Where c_{di} is the sectional induced drag coefficient and q_∞ is the dynamic pressure $\frac{1}{2} \rho V_\infty^2$.

To summarize for wings with an elliptical distribution and constant lift curve slope and absolute angle of attack, the nondimensional sectional properties will not vary along the span. Using these conditions, the product $m_0 \alpha_0 c$ must vary elliptically for

$$L'(y) = \rho V_\infty s \sqrt{1 - \left(\frac{y}{b/2}\right)^2} = m_0 \alpha_0 \frac{1}{2} \rho V_\infty^2 c \quad (3.29)$$

$$m_0 \alpha_0 c = \frac{2}{V_\infty} \sqrt{1 - \left(\frac{y}{b/2}\right)^2} \quad (3.30)$$

Notice that in an elliptical planform only the product $m_0\alpha_0$ is independent of y . On the other hand, for a non-elliptical planform, since m_0 is nearly constant, α_0 must be a specific function of y , that is, the wing must be twisted for the equation to be satisfied. This condition could occur only at a specific attitude of the wing.

The wing properties are found by integrating the section properties across the span. The wing lift-coefficient C_L is defined as the total wing lift divided by the product of the dynamic pressure q_∞ and the wing planform area S

$$C_L = \frac{1}{\frac{1}{2}\rho V_\infty^2 S} \int_{-b/2}^{b/2} L' dy = \frac{s^{\pi b}}{2V_\infty S} \quad (3.31)$$

Notice that the wing lift coefficient and sectional lift coefficient are equal when the sectional lift coefficients are constant along the span. Under this condition, the induced angle of attack for an elliptical distribution becomes,

$$\alpha_i = -\frac{C_L}{\pi AE} = -\frac{c_l}{\pi AE} \quad (3.32)$$

Where AE is the aspect ratio of the wing and is defined as $AE = \frac{b^2}{S}$ (3.33)

The wing induced drag coefficient is given by

$$C_{Di} = c_{di} = -C_L \alpha_i = \frac{C_L^2}{\pi AE} \quad (3.34)$$

Experiments have shown that the extra power needed to compensate the induced drag is quite significant even at low flight speed. Since for a given lift coefficient the induced drag is inversely proportional to the aspect ratio, the extra power can be made smaller by increasing the aspect ratio of the wing. For this reason, slender wings of

larger aspect ratio are often observed on gliders, low power light planes, long duration reconnaissance military planes, as well as birds migrating over long distances.

For high-lift, high-payload conditions, induced drag is accountable for up to 40% of the total aerodynamic drag coefficient and, as a result, any attempt to improve such flight characteristic is highly sought-after and desirable. For design purposes, it is essential to understand that properties of wing-tip vortices change based on the speed, weight and shape of the lift-producing surface. Weight is the main contributor as the vortices' strength is virtually proportional to the operating weight of an aircraft and, as a result, to its lift. Great detail needs to be given to the effects of the generation of great lift forces. At the same time, it is also inversely proportional to the wing-span over the velocity squared therefore correct dimensioning of the wing plays a major role in designing wing shapes.

So, in general, being that lift induces a large amount of drag which is strongly correlated to the strength of the trailing vortices that have origin at the wing tips of an aircraft, particular attention needs to be devoted to the development of optimized wing tip configurations.

3.5 Winglets

We have seen in Figure 3.16, Figure 3.17 and Figure 3.18 that the vortices trailing behind a finite wing are formed by the communication of the high and low pressure regions across the lifting surface through the wing tips. It has been shown that the trailing vortices induce a downwash velocity field at the wing, which in turn causes an induced drag on the wing.

Mounting end plates would not prevent the pressure communication through the wing tips because, as sketched in Figure 3.14 the circulation of the trailing vortices is the same as that about the wing. Thus during a steady, level flight the strength of the trailing vortices is proportional to the weight of the airplane and it will remain the same with or without the end plates. Experiments with vertical plates mounted on the

upper surface of a wing tips, indicate that the plates could reduce the maximum circumferential velocity of a rolled-up trailing vortex, but with a corresponding increase in the diameter of the core. The total circulation of the vortex appeared to be the same as that of the vortex trailing behind wing tips without the plates.

Although the total strength of the trailing vortices behind an airplane cannot be changed, it is possible to decrease the induced drag of a given airplane by using properly designed end plates, called winglets, to redistribute the strength of the trailing vortex sheet. Flat end plates are not efficient in that they cause viscous drag that is large enough to offset the reduction in induced drag. To be fully effective, the vertical surface at the tip must efficiently produce significant side forces that are required to reduce the lift-induced inflow above the wing tip or the outflow below the tip.

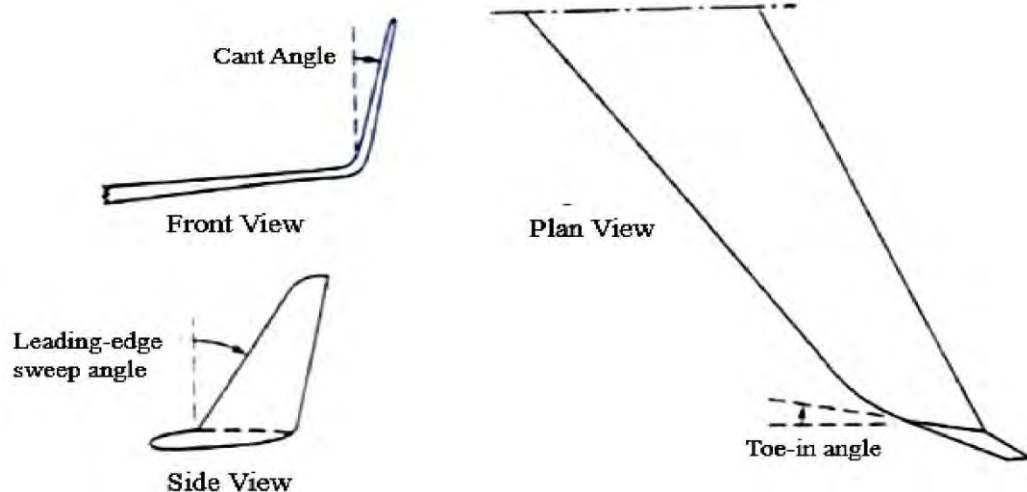


Figure 3.23: Winglet parameters

A typical winglet is shown above. It is a carefully designed lifting surface mounted at the wing tip, which can produce a gain in induced efficiency at a small cost in weight, viscous drag, and compressibility drag. The geometry of a winglet is primarily by the toe-in (or out) angle, cant angle, leading edge sweep angle, and the chord and aspect ratio of the winglet. Flow surveys behind the tip of a wing with and without winglets indicate that the basic effect of the winglets is a vertical diffusion of the tip vortex flow just downstream of the tip, which leads to drag reduction.

The gain in induced efficiency for a winglet is greater for a wing that has larger loads near the tip. If the winglet was set vertically on the wing tip, it would behave like an endplate, that is, its own normal force would contribute nothing to lift. On the other hand, if the winglet lay in the plane of the wing, its effect would be that of an irregular extension of the span, causing a large increase in the bending moment at the wing root and therefore a weight penalty for the wing structure. In practice, the winglet generally has an outward cant angle so that its influence is a mixture of both effects. The best cant angle will be a compromise between induced efficiency and drag caused by mutual interference at the junction of the wing tip and the winglet. Winglet toe-in angle provides design freedom to trade small reductions in induced efficiency increment for larger reductions in the weight penalties caused by the increased bending moment at the wing root.

For high effectiveness of the winglet for cruise conditions, the leading edge of the winglet is placed near the crest of the wing-tip section with its trailing edge near the trailing edge of the wing (see Figure 3.23). In front of the upper winglet mounted above the wing tip, a shorter lower winglet may also be mounted below the wing tip. A lower winglet in combination with a larger upper winglet produces relatively small additional reductions in induced drag at cruising speeds, but may improve overall winglet effectiveness at both high-lift and supercritical conditions.

3.6 Selection Criteria to Use NACA 4412

Though there are various types of wings available in the world but the researcher is used NACA 4412 in this experiment because it has good stall properties and has low roughness effect. However, it has low lift coefficients and relatively high drag. These wing are mainly used for general aviation. Their lift and drag values differ from each other and vary with changing angle of attack. Thus, researcher wants to use different planforms of NACA 4412 to undergo various test in wind tunnel to observe their different aerodynamic characteristics. Thereby, the efficient planform model can be utilized in general aviation.

MATHEMATICAL MODELING

4.1 Determination of Pressure Coefficient

The wind tunnel has a reference pressure tap located upstream of the test section and the pressure there is:

$$P_{\infty} = \rho_{water} g (h_{atm} - h_{\infty}) \quad (4.1)$$

From the Bernoulli relation, the corresponding velocity along a horizontal stream line is:

$$V_{\infty} = \sqrt{\frac{2\rho_{water} g (h_{atm} - h_{\infty})}{\rho_{air}}} \quad (4.2)$$

The 32 pressure taps provide pressure values determined from the manometer as:

$$P_i = \rho_{water} g (h_{atm} - h_i) \quad (4.3)$$

The pressure coefficient (C_p) is a dimensionless number which describes the relative pressures throughout a flow field in fluid dynamics. It is used in aerodynamics and hydrodynamics. Every point in a fluid flow field has its own unique pressure coefficient. It is very common to find pressures given in terms of C_p rather than the pressure itself. Figure 4.1 shows the pressure distribution at any point over the surface in terms of the pressure coefficient, C_p , which is defined as follows:

$$C_p = \frac{P_{Local} - P_{\infty}}{\frac{1}{2} \rho V_{\infty}^2} \quad (4.4)$$

Where, $\frac{1}{2}\rho V_\infty^2$ is the free stream dynamic pressure head

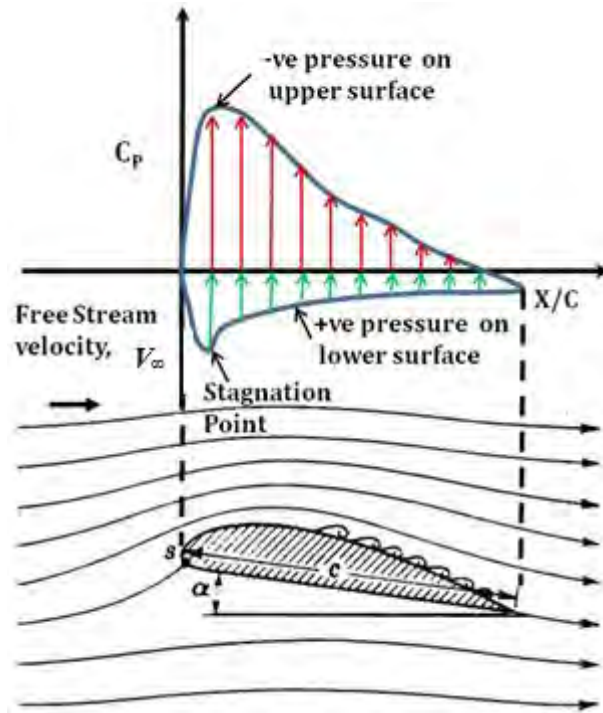


Figure 4.1: Pressure Distribution over an Aerofoil's Surface in terms of C_p [39, 46].

Thus, surface pressure coefficient, C_p can be calculated from the static pressure by the following formula [39, 46].

$$C_{p,i} = \frac{P_i - P_\infty}{\frac{1}{2}\rho V_\infty^2} \quad (4.5)$$

Where, P_i is the surface static pressure at any designated point i .

Values of C_p at any point over the aerofoil surface can be approximated from the corresponding boundary values by using the first order Lagrange interpolation and extrapolation:

$$c_p(x) = \frac{(x-x_1)}{(x_0-x_1)} c_{p,0} - \frac{(x-x_0)}{(x_1-x_0)} c_{p,1} \quad (4.6)$$

4.2 Estimation of Aerodynamic Force Coefficients from C_p

The aerodynamic forces and moments on the body are due to only two basic sources such as *the pressure distribution* over the body surface and *the Shear stress distribution* over the body surface [47]. No matter how complex the body shape may be, the aerodynamic forces and moments on the body are due entirely to the above two basic sources. The *only* mechanisms nature has for communicating a force to a body moving through a fluid are pressure and shear stress distributions on the body surface. Both pressure p and shear stress τ have dimensions of force per unit area (pounds per square foot or newton's per square meter). As sketched in Figure 4.2, p acts *normal* to the surface, and τ acts *tangential* to the surface. Shear stress is due to the "tugging action" on the surface, which is caused by friction between the body and the air.

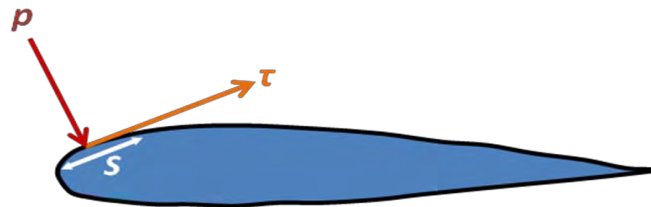


Figure 4.2: Illustration of Pressure and shear Stress on Aerofoil Surface [47].

The net effect of the p and τ distributions integrated over the complete body surface is a resultant aerodynamic force R on the body. In turn, the resultant R can be split into components, two sets of which are shown in Figure 4.3. In Figure 4.3, U_∞ is the *relative wind*, defined as the flow velocity far ahead of the body. The flow far away from the body is called the *free stream*, and hence U_∞ is also called the free stream velocity. In Figure 4.3, by definition,

$$L = \text{lift} = \text{component of } R \text{ perpendicular to } U_\infty$$

$$D = \text{drag} = \text{component of } R \text{ parallel to } U_\infty$$

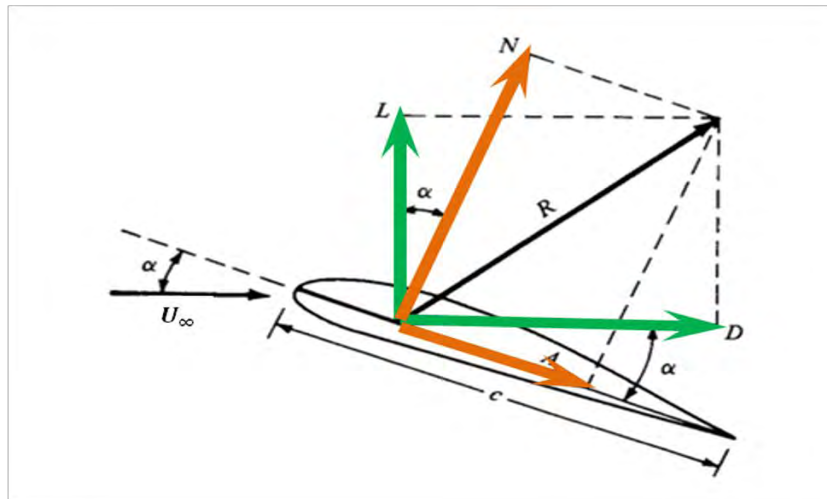


Figure 4.3: Resultant Aerodynamic Force and its Components [40, 47].

The chord c is the linear distance from the leading edge to the trailing edge of the body. Sometimes, R is split into components perpendicular and parallel to the chord, as also shown in Figure 4.3. By definition,

N = normal force = component of R perpendicular to c

A = axial force = component of R parallel to c

The angle of attack α is defined as the angle between c and U . Hence, α is also the angle between L and N and between D and A . The geometrical relation between these two sets of components is found from Figure 4.3 as:

$$L = N \cos \alpha - A \sin \alpha \quad (4.7)$$

$$D = N \sin \alpha + A \cos \alpha \quad (4.8)$$

The integration of the pressure and shear stress distributions can be done to obtain the aerodynamic forces and moments [39, 48]. Let us consider the two dimensional body sketched in Figure 4.4. The chord line is drawn horizontally, and hence the relative wind is inclined relative to the horizontal by the angle of attack α . An xy coordinate system is oriented parallel and perpendicular, respectively, to the chord. The distance from the leading edge measured along the body surface to an arbitrary point A on the upper surface is s_u ; similarly, the distance to an arbitrary point B on

the lower surface is s_l . The pressure and shear stress on the upper surface are denoted by p_u and τ_u , respectively; both p_u and τ_u are functions of s_u . Similarly, p_l and τ_l are the corresponding quantities on the lower surface and are functions of s_l .

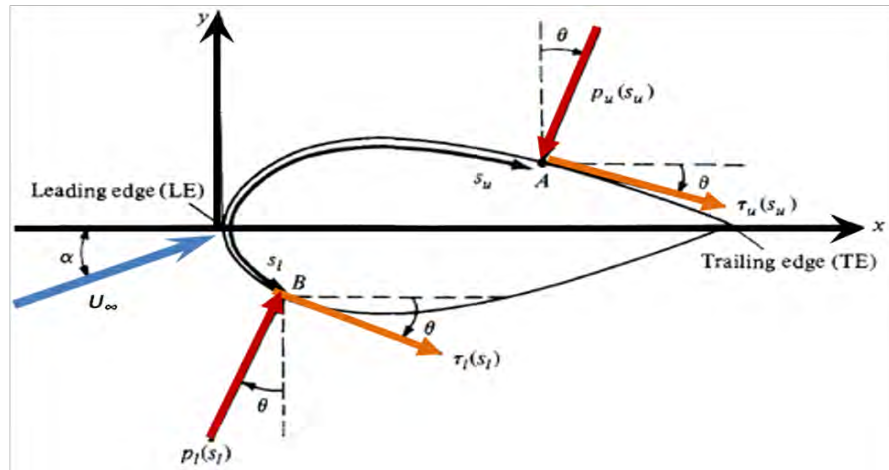


Figure 4.4: Nomenclature for Integration of p and τ Distribution [39, 48].

At a given point, the pressure is normal to the surface and is oriented at an angle θ relative to the perpendicular; shear stress is tangential to the surface and is oriented at the same angle θ relative to the horizontal. In Figure 4.4, the sign convention for θ is positive when measured *clockwise* from the vertical line to the direction of p and from the horizontal line to the direction of τ . In Figure 4.4, all thetas are shown in their positive direction.

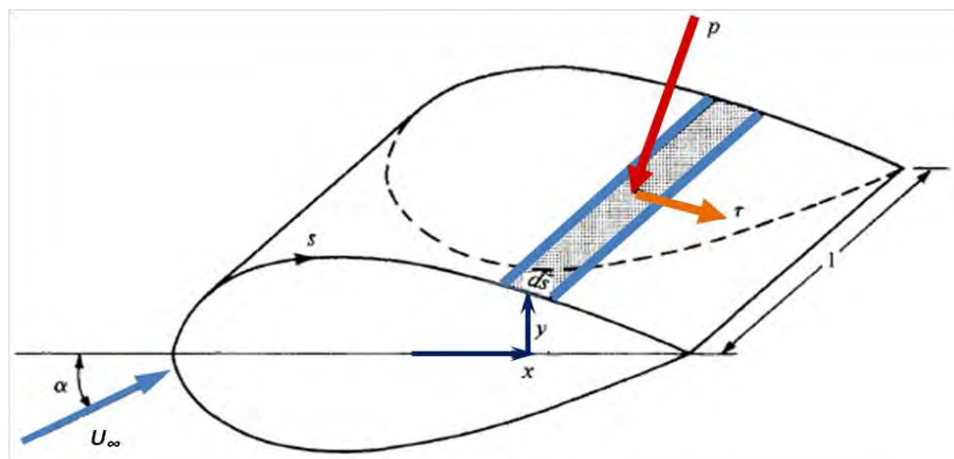


Figure 4.5: Aerodynamic Force on an Element of the Body Surface [39, 48].

Now let us consider the two-dimensional shape in Figure 4.4 as a cross section of an infinitely long cylinder of uniform section. A unit span of such a cylinder is shown in Figure 4.5. Let us consider an elemental surface area dS of this cylinder, where $dS = (ds)(l)$ as shown by the shaded area. We are interested in the contribution to the total normal force N' and the total axial force A' due to the pressure and shear stress on the elemental area dS . The primes on N' and A' denote force per unit span. Examining both Figures 4.4 and 4.5, it is seen that the elemental normal and axial forces acting on the elemental surface dS on the *upper* body surface are

$$dN'_u = -p_u ds_u \cos\theta - \tau_u ds_u \sin\theta \quad (4.9)$$

$$dA'_u = -p_u ds_u \sin\theta + \tau_u ds_u \cos\theta \quad (4.10)$$

On the *lower* body surface, we have

$$dN'_l = p_l ds_l \cos\theta - \tau_l ds_l \sin\theta \quad (4.11)$$

$$dA'_l = p_l ds_l \sin\theta + \tau_l ds_l \cos\theta \quad (4.12)$$

In these equations, the positive clockwise convention for θ must be followed. For example, consider again Figure 4.4. Near the leading edge of the body, where the slope of the upper body surface is positive, τ is inclined upward, and hence it gives a positive contribution to N' . For an upward inclined τ , θ would be counterclockwise, hence negative. Therefore, in Equation (4.9), $\sin\theta$ would be negative, making the shear stress term (the last term) a positive value, as it should be in this instance.

The total normal and axial forces *per unit span* are obtained by integrating Equations (4.9) to (4.12) from the leading edge (LE) to the trailing edge (TE):

$$N' = - \int_{LE}^{TE} (p_u \cos\theta + \tau_u \sin\theta) ds_u + \int_{LE}^{TE} (p_l \cos\theta - \tau_l \sin\theta) ds_l \quad (4.13)$$

$$A' = \int_{LE}^{TE} (-p_u \sin\theta + \tau_u \cos\theta) ds_u + \int_{LE}^{TE} (p_l \sin\theta - \tau_l \cos\theta) ds_l \quad (4.14)$$

In turn, the total lift and drag per unit span can be obtained by inserting Equations (4.13) and (4.14) into (4.7) and (4.8).

There are quantities of an even more fundamental nature than the aerodynamic forces themselves. These are *dimensionless force coefficients*. We have already defined a dimensional quantity called the free stream *dynamic pressure* as $q_\infty = \frac{1}{2}\rho U_\infty^2$. In addition, let s be a reference area and l be a reference length. The dimensionless force coefficients are defined as follows:

$$\text{Lift coefficient:} \quad C_L = \frac{L}{q_\infty s} \quad (4.15)$$

$$\text{Drag coefficient:} \quad C_D = \frac{D}{q_\infty s} \quad (4.16)$$

$$\text{Normal force coefficient:} \quad C_N = \frac{N}{q_\infty s} \quad (4.17)$$

$$\text{Axial force coefficient:} \quad C_A = \frac{A}{q_\infty s} \quad (4.18)$$

In the above coefficients, the reference area S and reference length l are chosen to pertain to the given geometric body shape; for different shapes, S and l may be different things. For example, for an airplane wing, S is the planform area, and l is the mean chord length, as illustrated in Figure 4.6.

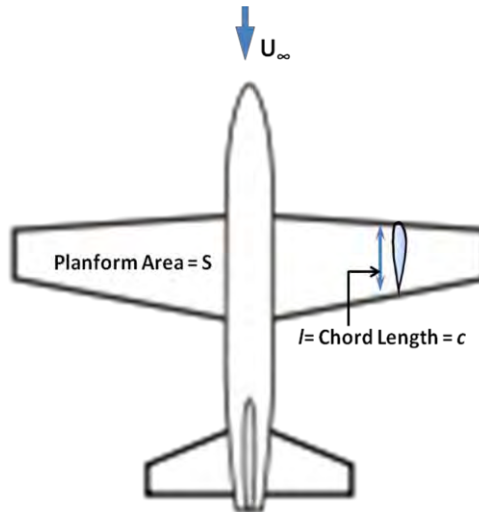


Figure 4.6: Reference Area and Length for Airplane [39].

The symbols in capital letters listed above, i.e., C_L , C_D , C_N , and C_A , denote the force coefficients for a complete three-dimensional body such as an airplane or a finite wing. In contrast, for a two-dimensional body, the forces are per unit span. For these two dimensional bodies, it is conventional to denote the aerodynamic coefficients by lowercase letters as follows:

$$c_l = \frac{L'}{q_\infty c} \quad \text{and} \quad c_d = \frac{D'}{q_\infty c}$$

Where, the reference area $S = c(l) = c$.

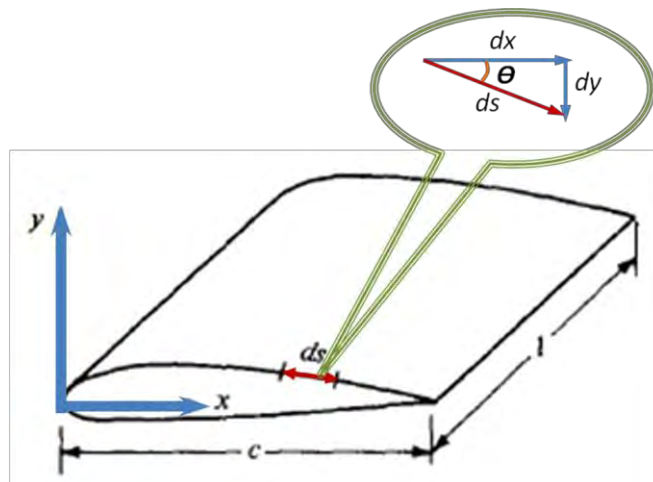


Figure 4.7: Geometrical Relationship of Differential Lengths [39, 48].

The most useful forms of Equations (4.13) and (4.14) are in terms of the dimensionless coefficients introduced above. From the geometry shown in Figure 4.7,

$$\begin{aligned} dx &= ds \cos \theta \\ dy &= -ds \sin \theta \\ S &= c(l) = c \end{aligned}$$

Substituting the above expressions of dx , dy and S into Equations (4.13) and (4.14), dividing by q_∞ , we obtain the following integral forms for the force and moment coefficients:

$$C_n = \frac{1}{c} \int_0^c (c_{p,l} - c_{p,u}) dx + \frac{1}{c} \int_0^c \left(c_{f,u} \frac{dy_u}{dx} + c_{f,l} \frac{dy_l}{dx} \right) dx \quad (4.19)$$

$$C_a = \frac{1}{c} \int_0^c \left(c_{p,u} \frac{dy_u}{dx} - c_{p,l} \frac{dy_l}{dx} \right) dx + \frac{1}{c} \int_0^c (c_{f,u} + c_{f,l}) dx \quad (4.20)$$

Here, y_u is directed above the x axis, and hence is positive, whereas y_l is directed below the x axis, and hence is negative. Also, dy/dx on both the upper and lower surfaces follow the usual rule from calculus, i.e., positive for those portions of the body with a positive slope and negative for those portions with a negative slope. When shear stress due to viscous effect is neglected, an integration of a pressure distribution over an airfoil chord for both upper and lower surfaces is known to provide normal and axial force acting on an airfoil section [39, 51] as follows:

$$C_n = \frac{1}{c} \int_0^c (c_{p,l} - c_{p,u}) dx \quad (4.21)$$

$$C_a = \frac{1}{c} \int_0^c \left(c_{p,u} \frac{dy_u}{dx} - c_{p,l} \frac{dy_l}{dx} \right) dx \quad (4.22)$$

The known pressure coefficients from the experiment can be calculated for the normal and axial force by using a numerical integration of the above equations in the Trapezoidal approximating forms.

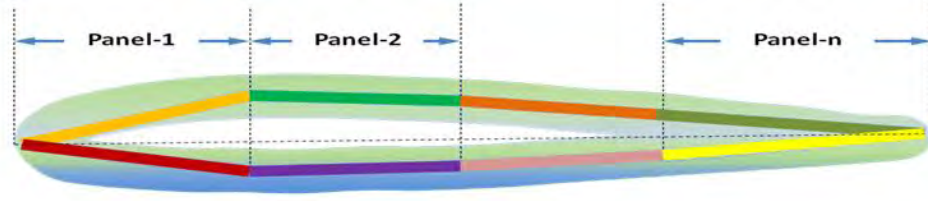


Figure 4.8: Paneling of the Wing Surface [39, 48].

As shown in Figure 4.8, both the surfaces of the wing section can be divided into small panels corresponding to a total of gaps between each pressure tap location [42]. When n is a number of panels, the equations can be converted to:

$$C_n = \sum_{i=1}^n \left[(c_{p,l,i} - c_{p,u,i}) \Delta \left(\frac{x_i}{c} \right) \right] \quad (4.23)$$

$$C_a = \sum_{i=0}^n \left[\left(c_{p,u,i} \frac{\Delta y_{u,i}}{\Delta x_i} - c_{p,l,i} \frac{\Delta y_{l,i}}{\Delta x_i} \right) \Delta \left(\frac{x_i}{c} \right) \right] \quad (4.24)$$

The interpolated and extrapolated pressure coefficients would be applied to Equation (4.23) and (4.24) in order to get the normal and axial force at a section of interest. Lift and drag coefficient can be obtained from:

$$c_l = c_n \cos \alpha - c_a \sin \alpha \quad (4.25)$$

$$c_d = c_n \sin \alpha + c_a \cos \alpha \quad (4.26)$$

The over-all value of the coefficients for the whole wing can be found out by averaging the same values of each segments of the wing along the span. Now from the value of C_l induced drag can be calculated from:

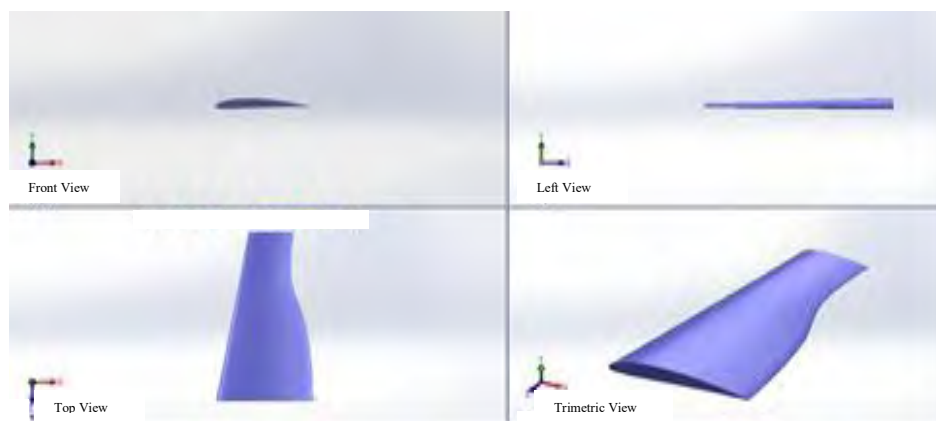
$$C_{D,i} = \frac{C_l^2}{\pi e AR} \quad (4.27)$$

Where e is span efficiency factor and for elliptical planforms, $e = 1$; for all other planforms, $e < 1$. For typical subsonic aircraft, e ranges from 0.85 to 0.95. AR is the aspect ratio of wing.

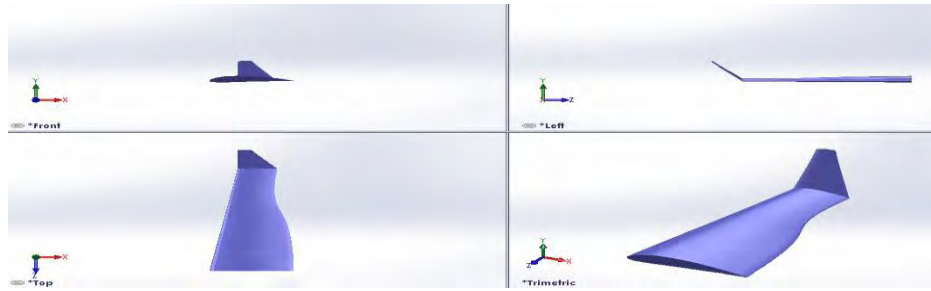
EXPERIMENTAL SETUP AND METHODOLOGY

5.1 Design and Construction

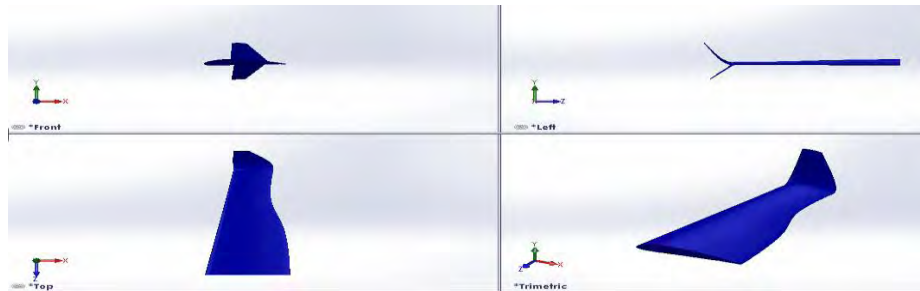
While manufacturing the wing and winglet model for taking data it is important to maintain extreme precision. To obtain that objective wing and winglet models are designed in Solidworks as shown in Figure 5.1 and then the aerofoil shape and projected planform area of the wing are cut using CNC milling machine to get precise size and shape. Finally, wooden wing models are prepared from those formats. The aerodynamic characteristics (C_L , C_D and L/D) can be calculated from the surface pressure distribution of the wing as discussed in the previous chapter. To obtain the pressure distribution over the surfaces, wooden wing and winglet models are prepared with a specific aerofoil, suitable fixture is prepared to set the models in the wind tunnel and a multi-tube manometer is fabricated to take the pressure readings from the surfaces of the wing models.



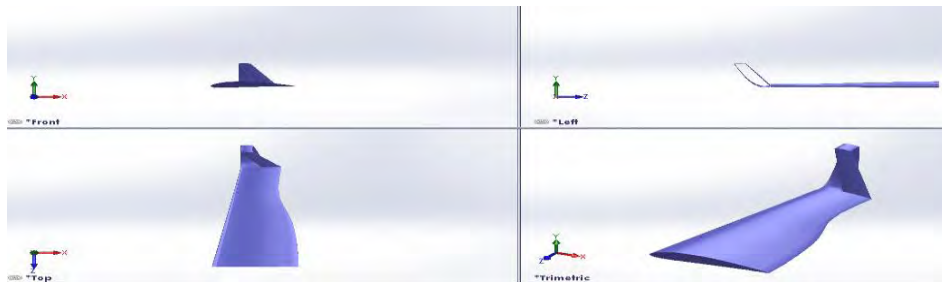
(a) Model-1: Curved Trailing Edge Tapered Wing without Winglet



(b) Model-2: Curved Trailing Edge Tapered Wing with Blended Winglet.



(c) Model-3: Curved Trailing Edge Tapered Wing with Double Blended Winglet.



(d) Model-4: Curved Trailing Edge Tapered Wing with Spiroid Winglet.

Figure 5.1: Solidworks design of Wing Models

5.1.1 Wing Models

Using NACA 4412 aerofoil, wooden models for four wings are prepared having the equal surface area (33407 mm^2) as shown in Figure 5.2. Winglets are made such that all three wings with winglet have same aspect ratio (AR 3.43) as shown in Figure 5.3. Each model is provided with 32 pressure tapings along the span and chord (16 at upper surface and 16 at lower surface). Along the span the wings are divided into four equal segments (A, B, C and D) as per the Figure 5.2. For wing, the chord

length at the root and the span length are 150 mm and 300 mm respectively. Four pressure tapping points at upper surface and four pressure tapping points at lower surface are made at 20%, 40%, 60% and 80% of the average chord length of each segment of all the wing models.

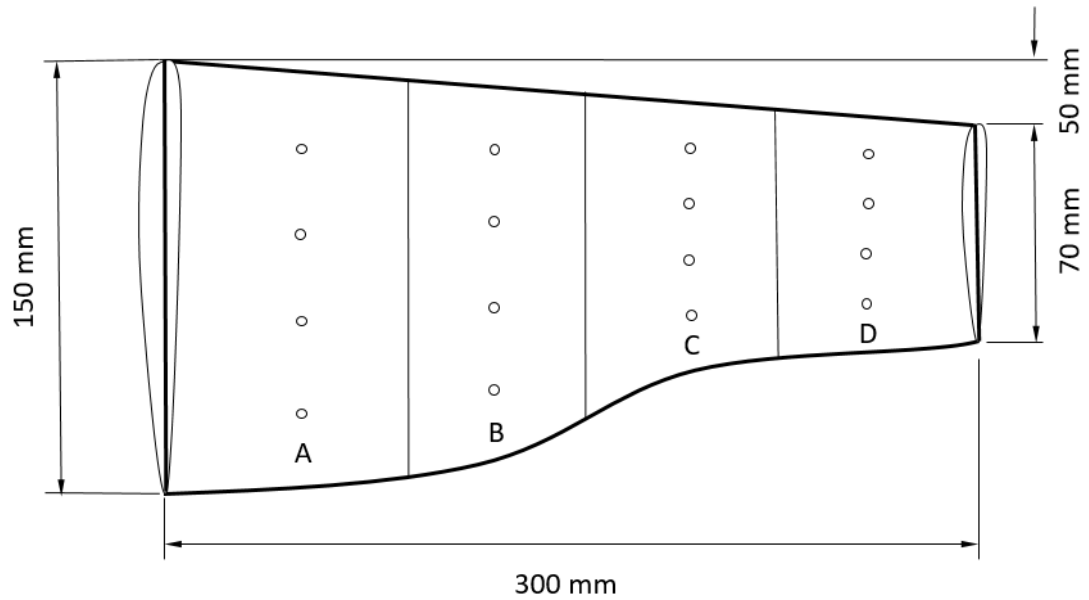
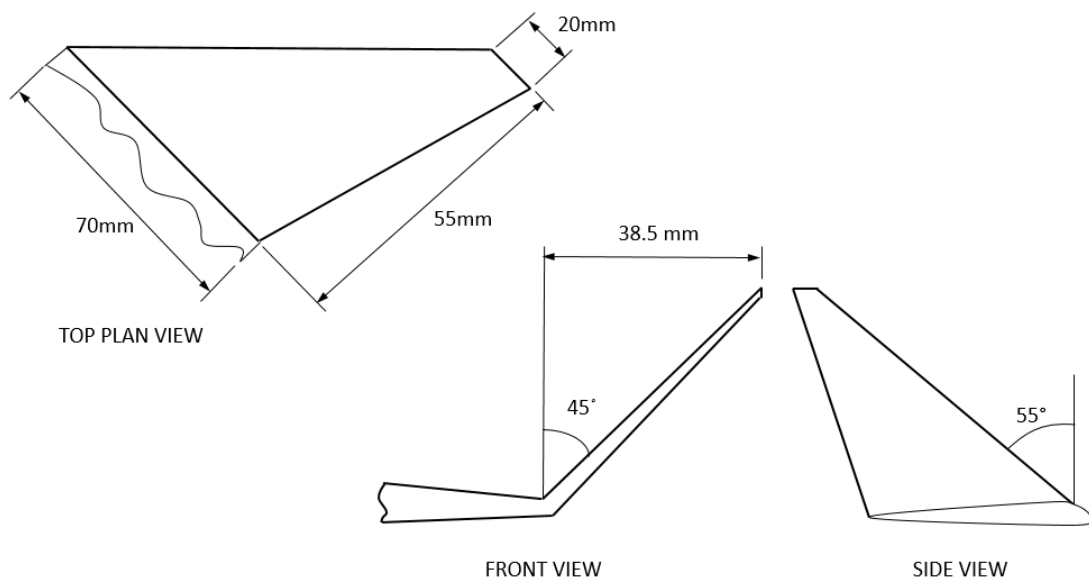
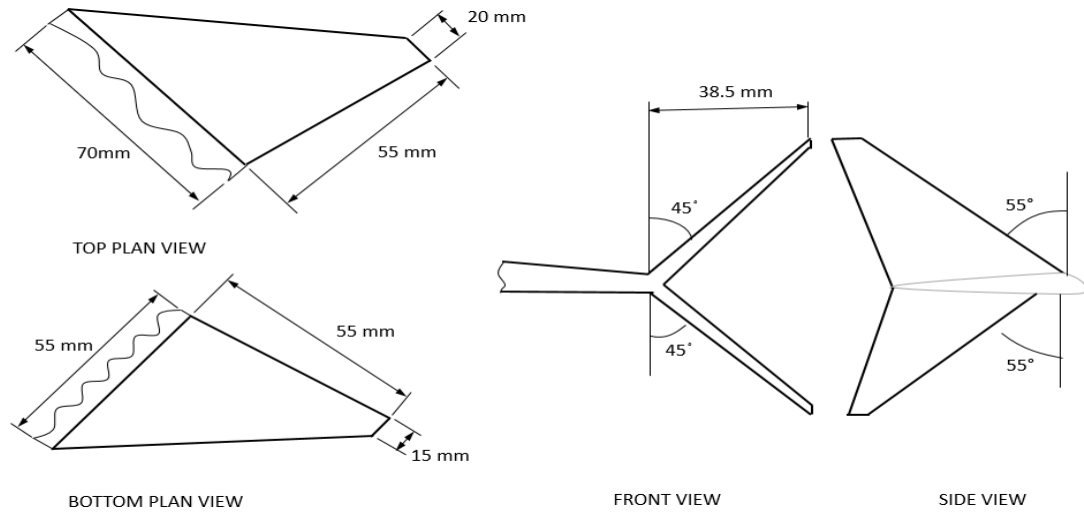


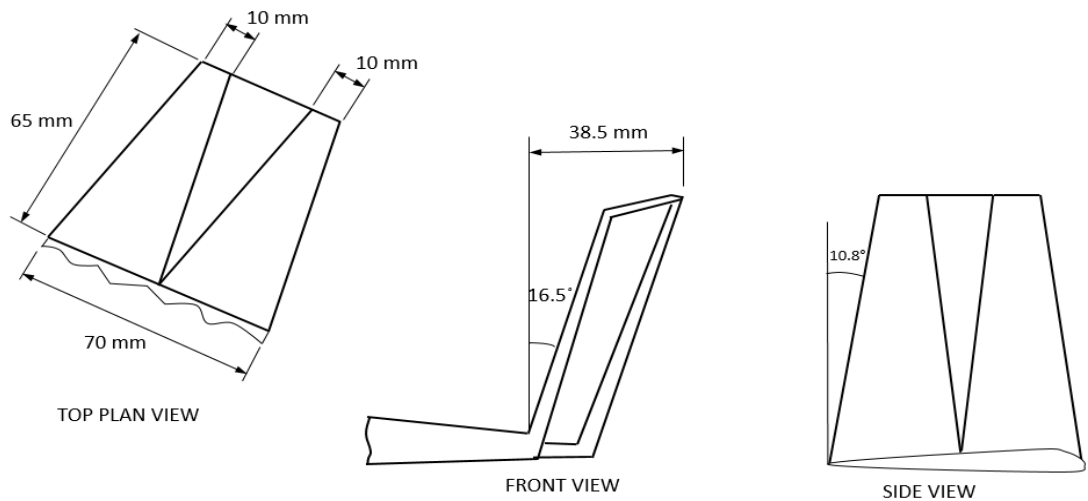
Figure 5.2: Curved Trailing Edge Tapered Planform (Reference Wing)



(a) Model-1: Blended Winglet.



(b) Model-2: Double Blended Winglet.



(d) Model-3: Spiroid Winglet.

Figure 5.3: Experimental Winglet Models

Table 2: Dimensions of Three Winglet Models

Model No	Type of Model	Cant angle, degree	Sweepback, degree	Ratio of winglet root chord to wing tip chord
1	Blended Winglet	45	55	0.29
2	Double Blended Winglet	45	55	0.29
3	Spiroid Winglet	16.5	10.8	0.29

5.1.2 Pressure Measuring Device

The arrangement of multi-tube manometer for measuring the pressures is shown in Figure 5.4. The multi-tube manometer mainly consists of a water tank and 36 manometer glass tubes (in this experiment, 32 glass tubes are used) connected to the tapping points in wing model surfaces. The water tank is used to store the distilled water. Each limb is fitted with a scale graduated in mm to measure the difference of water height. The static pressure is calculated from the difference in water height in glass tube.

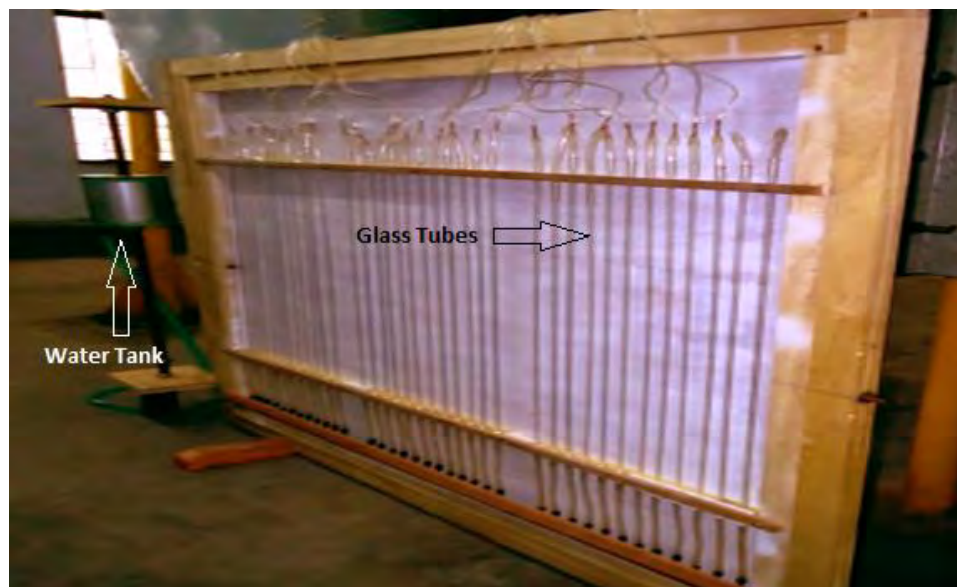


Figure 5. 4: Multi-tube Manometer

5.2 Experimental Setup

5.2.1 Wind Tunnel

The experiment is carried out in a 700 mm×700 mm closed circuit wind tunnel as shown in Figure 5.5 available at turbulence lab of Department of Mechanical Engineering, BUET.

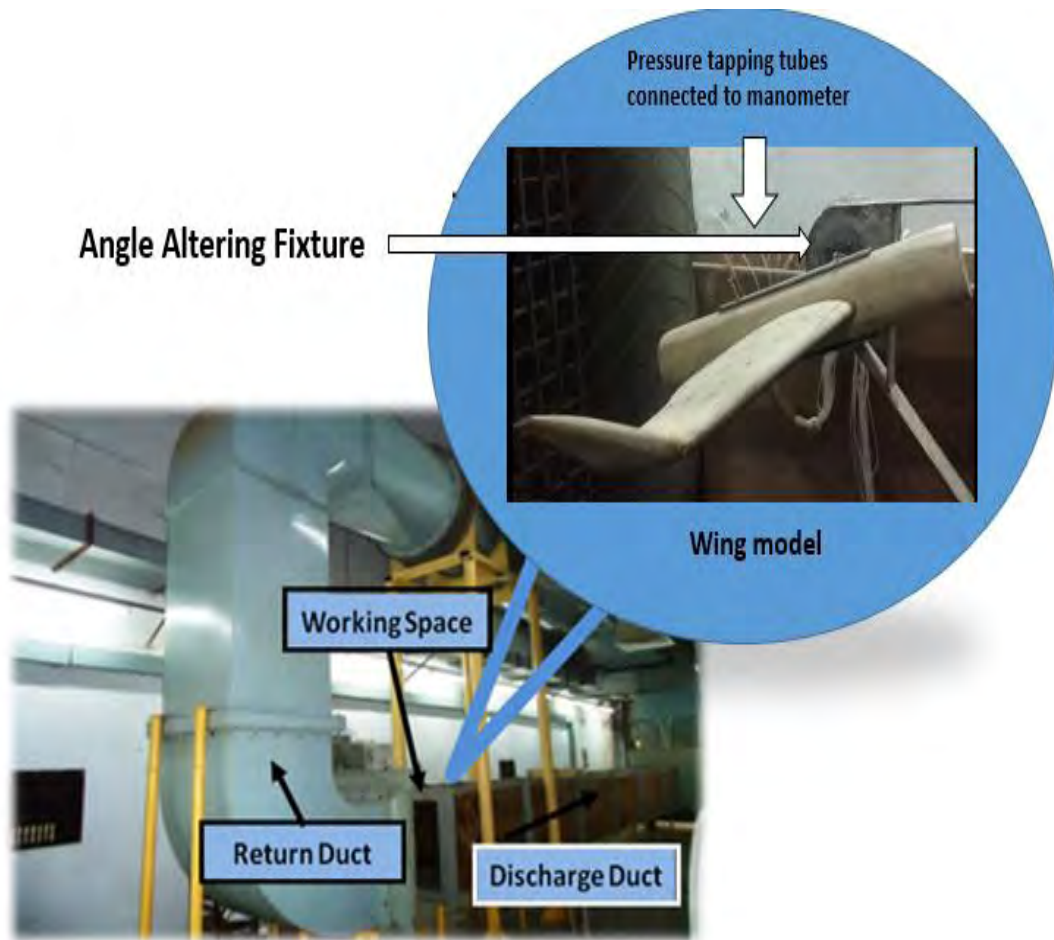


Figure 5. 5: Photograph of Experimental Set-up.

The wind speed is created by the two 700 mm counter rotating fans. At the discharge of the fans there is a silencer to reduce the sound level. From the silencer air flow passes through the flow controlling butterfly valve, diffuser and the plenum chamber to stabilize the flow. The fan motors are powered by 400V-3 Φ -50Hz power supply through motor speed controller. Thus the wind speed in the tunnel can be varied both by controlling the fan motor speed as well as by controlling the butterfly valve [49]. To facilitate the present experiment in the open air condition the diffuser at the end of the test section is taken out and the discharge side of the test section is fitted with a 700 mm \times 700 mm discharge duct and a 1000 mm \times 1000 mm to 762 mm \times 762 mm bell mouth entry is added at the return duct to have smooth entry. Thus the 406 mm open flow field created between the discharge duct and bell mouth entry become the experimental space as shown in Figure 5.6 where desired velocity is obtained.

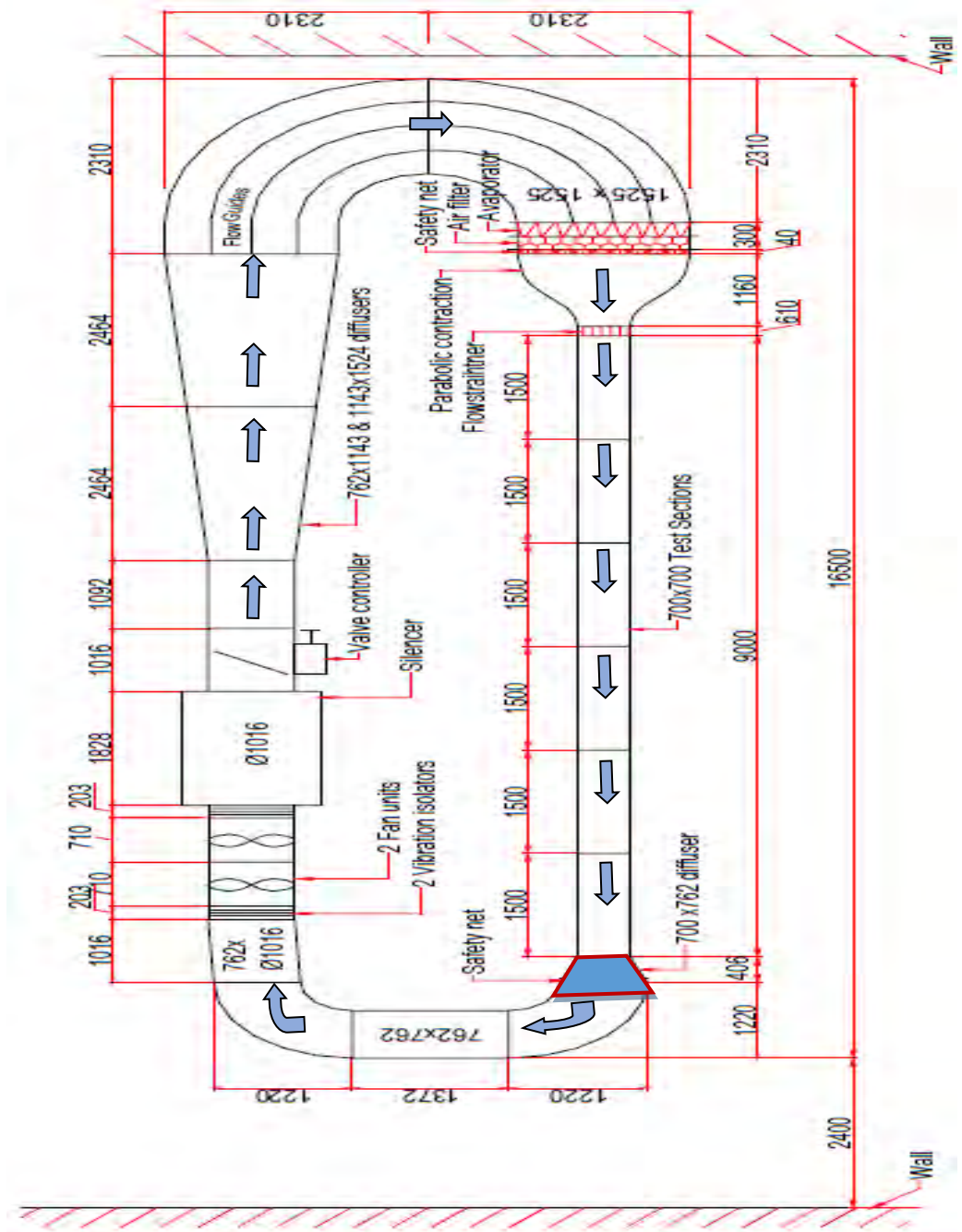


Figure 5. 6: Schematic Diagram of the Wind Tunnel at BUET's Turbulence Lab [49]

5.2.2 Fixture for Altering Angle of Attack

The details of wind tunnel are shown in Figure 5.6. A fixture is fabricated and fixed in the test section of the wind tunnel as shown in Figure 5.7. The fixture facilitates the wing models to rotate and fixes at any angle of attack. The wing models are tested at angle of attack from -4° to 24° with a step of 4° . Each model is rotated and fixed at the desired angle by seeing the preset scales (in degrees) pasted with glue on the frame.

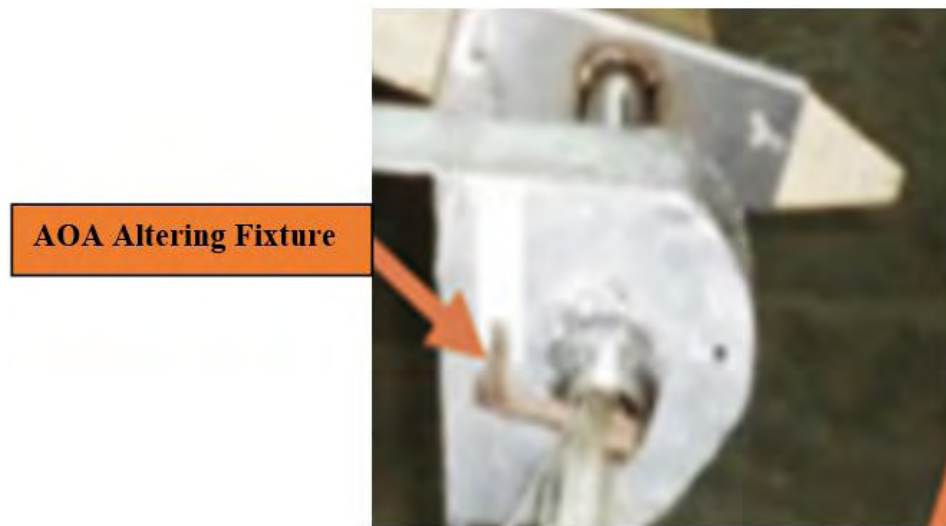


Figure 5.7: AOA Altering Fixture

5.2.3 Experimental Parameters

All the experimental data are taken at room temperature of 20°C and at air speed of 27.4 m/s (98.64 kph) and the air flow is considered incompressible throughout the experiment. The Reynold number and Mach number are 2.05×10^5 and 0.08 respectively. The density of both air and water corresponding to room temperature is 1.204 kg/m^3 and 998.29 kg/m^3 respectively.

5.3 Methodology

- a. Initially, the static pressure at different angles of attack ($\alpha = -4^\circ, 0^\circ, 4^\circ, 8^\circ, 12^\circ, 16^\circ, 20^\circ$ and 24°) are measured from both upper and lower surfaces of the wing models through different pressure tapings by using a multi-tube manometer during wind tunnel testing.
- b. From the static pressure data, the respective coefficient of pressure (C_p) is calculated using equation (4.1) to (4.6).
- c. The values of C_p of both surfaces of individual planforms are plotted in C_p versus %C graph to observe the pressure pattern of different segments of each planform along the chord length.
- d. C_L and C_D of all the wing planforms at every angle of attack are determined from equation (4.23) to (4.26).
- e. L/D at different angle of attack for all the wing models are obtained from the ratio of C_L to C_D at respective angle of attack.
- f. Induced drag coefficients $C_{D,i}$ of all wing models are calculated from the value of C_L at respective angle of attack.
- g. Finally, the lift characteristics, drag characteristics, lift to drag ratio and induced drag of the wing models are analyzed and compared with each other from C_L versus α , C_D versus α , L/D versus α and $C_{D,i}$ versus α graphs.

RESULTS AND DISCUSSIONS

6.1 Introduction

In order to analyze aerodynamic characteristics, the pressure coefficients of both upper and lower surfaces of different wings with winglets are measured through the wind tunnel testing. Then the pressure coefficients are plotted along chord wise positions (% C) at different angles of attack for each of the four segments. The pressure coefficients of a wing without winglet are also measured and plotted. Then surface pressure distribution of all the wing planforms are discussed and compared. The data taken from the pressure distribution are used to calculate normal and axial forces on the wing models. These normal and axial forces are used to determine coefficient of lift (C_L), coefficient of drag (C_D) and lift to drag ratio (L/D) of individual wing. Then the effect of angle of attack on C_L , C_D and L/D is studied and used in comparison. Calculated values of pressure coefficients of wings with and without winglet from -4° to 24° angles of attack are shown in Appendix-I. Uncertainties of experimental results are also analyzed in light of the procedure suggested by Cimbala [49]. The details of uncertainty analysis are shown in Appendix-II.

6.2 Surface Pressure Distributions

The pressure distributions of both upper and lower surfaces along the chord length of four segments (Segment- A, B, C and D) of four experimental wing models at -4° , 0° , 4° , 8° , 12° , 16° , 20° and 24° angle of attack (AOA) are shown in Fig. 6.1 to 6.32. In the figures, the horizontal axis represents the percentage of the chord length (%C) and the vertical axis represents the surface pressure coefficient (C_p). The vertical axis above the zero line (horizontal axis) denotes the negative pressure coefficients or suction pressure coefficients and the vertical axis below the zero line denotes the

positive pressure coefficients. All the graphs are discussed in details in the subsequent sub-paragraphs.

6.2.1 Pressure Distributions at - 4° AOA

Figures 6.1, 6.2, 6.3 and 6.4 represent the surface pressure distribution in terms of pressure coefficient of four segments (A, B, C and D) of (i) wing without winglet, (ii) wing with blended winglet, (iii) wing with double blended winglet and (iv) wing with spiroid winglet at - 4° AOA. In the figures, both upper and lower surface pressure coefficient, C_{pu} and C_{pl} are plotted along the chord length (C).

The surface pressure coefficients of segment A at -4° are shown in Figure 6.1. It is observed from the graph that the pressure on the wing near the root is very low for all wing models. Near the leading edge the lower surfaces of all the wing models are experiencing higher negative pressure than the upper surfaces. But after 25% C towards the trailing edge the upper surfaces are having more negative pressure compared to lower surfaces. It is also observed that the lower surface pressure increases from 20% to 40% C and then increases slowly up to 80% C for all wing models. The upper surface pressure decreases initially from 20% up to 40% C and then rises gradually up to 80% C except for wing with double blended winglet whose upper surface pressure remains almost constant.

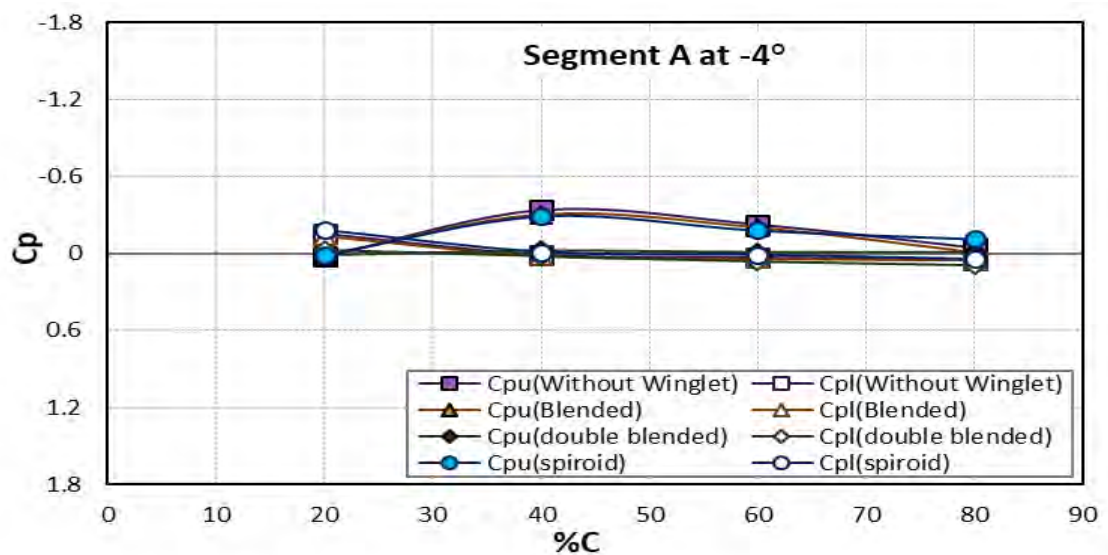


Figure 6.1: C_p Distribution of Segment-A at $\alpha = -4^\circ$

Figure 6.2 illustrates the surface pressure distribution of segment B for four wing models. It is seen that near the leading edge, both upper and lower surface pressure of all the wing models at segment B are also almost at the negative side. For all wing models lower surfaces are having higher negative pressure than the upper surfaces near the leading edge. But from about 25% of C towards the trailing edge the negative pressures of the upper surfaces are more than the negative pressure of lower surfaces. The overall pressure difference between upper and lower surface is highest for wing with blended winglet, lowest for wing with double blended winglet and in between for wing without winglet and wing with spiroid winglet. The lower surface pressures for wing without winglet and wing with blended winglet are almost equal from leading edge to trailing edge. But these two wing models are having greater pressure at lower surface than wing with double blended winglet and wing with spiroid winglet.

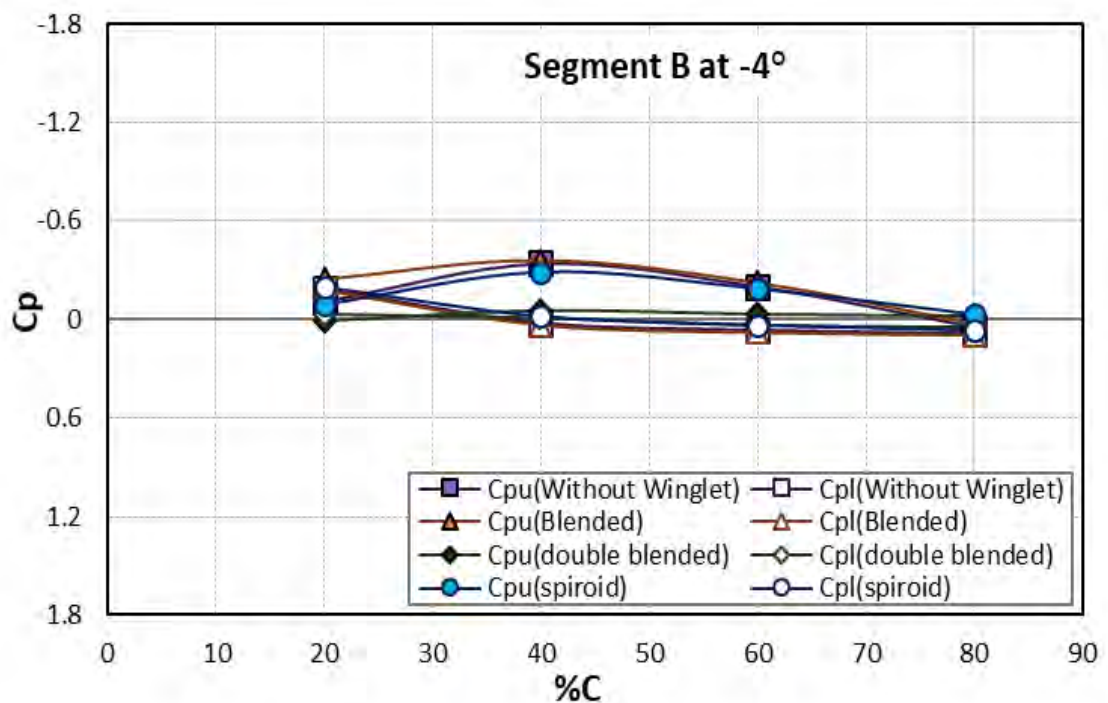


Figure 6.2: C_p Distribution of Segment-B at $\alpha = -4^\circ$

Up to 40% C, the upper surface pressure of wing with blended winglet is lowest and highest for wing with double blended winglet. The upper surface pressure of wing

without winglet and wing with spiroid winglet are in between the wing with blended and wing with double blended winglet up to 40% C. From 40% C to 60% C, upper surface pressure of wing with blended winglet and wing without winglet are almost overlapping with each other. These two wing models are having lower pressure than other two wing models from 40% C to 60% C. Between the other two wing models that is wing with double blended and wing with spiroid winglet, the upper surface pressure for wing with spiroid winglet is lower than wing with double blended winglet from 40% to 60% C. Then in between 60~ 75% C, the upper surface pressure for wing with double blended winglet is still highest. For other three wing models, the upper surface pressures are passing through almost same line within 60~ 75% of C. Beyond 75% C up to the trailing edge, all the curves are almost overlapping each other following similar pattern.

Figure 6.3 shows the upper and lower surface pressure distribution for Segment-C of the wing models. For wing without winglet, the lower surface is having higher negative pressure than upper surface near the leading edge. The lower surface pressure increases rapidly from up to 40% C and then again decreases slowly up to the trailing edge.

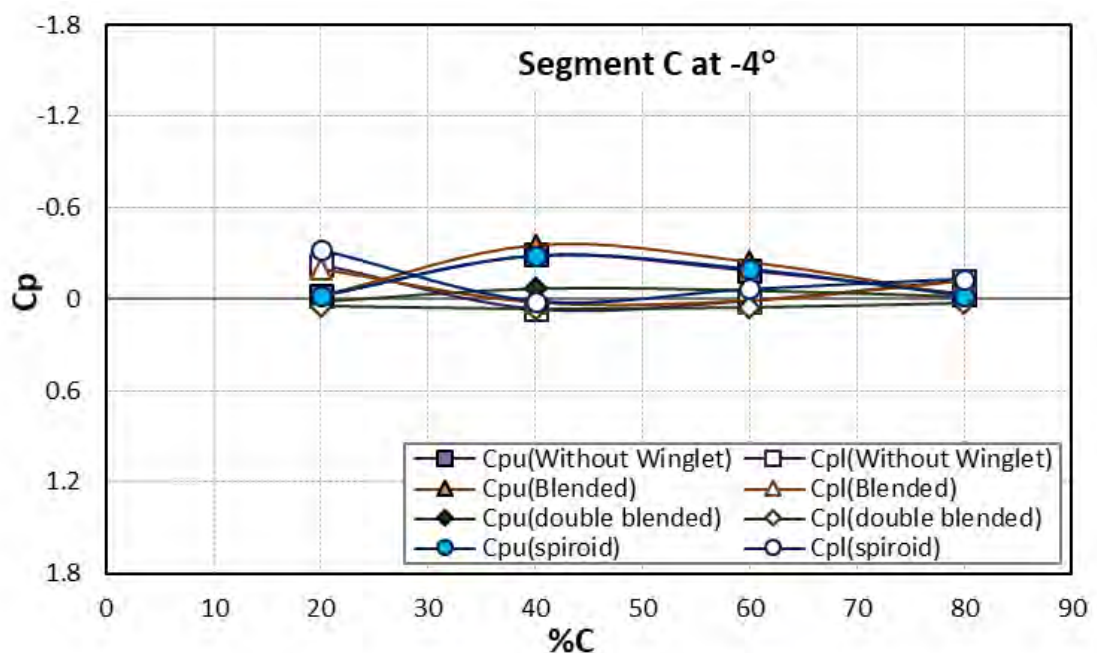


Figure 6.3: C_p Distribution of Segment-C at $\alpha = -4^\circ$

But the upper surface pressure decreases up to 40% C and then increases slowly up to the trailing edge. For wing with blended winglet and wing with spiroid winglet, the lower surface negative pressure is greater than the upper surface negative pressure near the leading edge. Then from almost 25% of C up to the trailing edge, upper surface is having greater negative pressure than lower surface. The lower surface pressures of the two wing models increase up to 40% C and then decrease slowly up to the trailing edge. But the upper surface pressures decrease up to 40% C and then gradually increase towards the trailing edge. The differences between upper and lower surface pressure of wing with blended winglet and wing with spiroid winglet are highest at 40% C and these differences gradually decrease up to the trailing edge. For wing with double blended winglet, the upper surface is having more negative pressure than the lower surface throughout the chord length. The lower surface pressure remains almost constant whereas the upper surface pressure decreases slightly up to 40% C and then increases towards the trailing edge.

In Figure 6.4, the surface pressure distributions for Segment-D of the wing models are shown. For wing without winglet, the upper surface is having higher negative pressure than the lower surface throughout the chord length. The upper surface pressure decreases from 20% C to 40% C and then increases gradually up to the trailing edge. The lower surface pressure decreases up to 40% C and then increases up to the trailing edge. The difference between upper and lower surface of wing without winglet is highest at 40% C. Similarly, for wing with blended winglet and wing with spiroid winglet, the upper surfaces are having greater negative pressure than the lower surfaces throughout the chord length. Up to 40% C the upper surface pressures decrease rapidly and then increases gradually up to the trailing edge. The differences between upper and lower surface pressure of wing with blended winglet and wing with spiroid winglet are highest at 40% C and these differences gradually decrease up to the trailing edge. For wing with double blended winglet, the upper surface is having higher negative pressure than the lower surface from leading edge to trailing edge. The upper surface pressure decreases up to 40% C and then increases gradually up to the trailing edge. The lower surface pressure decreases gradually from leading edge to trailing edge. The overall pressure difference

between the two surfaces is highest for wing with blended winglet and lowest for wing with double blended winglet in segment D.

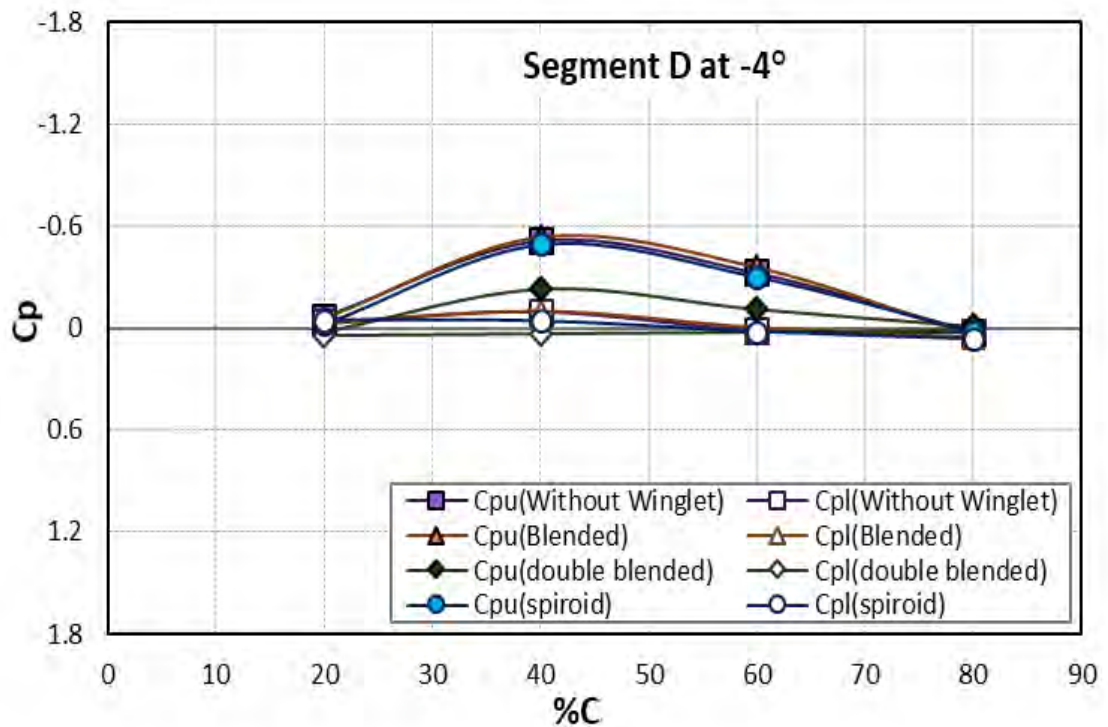


Figure 6.4: C_p Distribution of Segment-D at $\alpha = -4^\circ$

6.2.2 Pressure Distributions at 0° AOA

Figures 6.5, 6.6, 6.7 and 6.8 represent the surface pressure distribution in terms of pressure coefficient of four segments (A, B, C and D) of wing without winglet and wing with different winglet models at 0° AOA. In the figures, both upper and lower surface pressure coefficient, C_{pu} and C_{pl} are plotted along the chord length (C).

In Figure 6.5, the surface pressure distributions for segment-A of the wing models at 0° AOA are shown. From the figure it is observed that upper surfaces of four wing models are having higher negative pressure than the lower surfaces. The upper surface pressures for wing models decrease up to 40% C and then increase gradually towards the trailing edge. Among the four wing models, the upper surface pressure

is lowest for the wing without winglet and highest for wing with double blended winglet. For wing with blended winglet and wing with spiroid winglet, the upper surface pressures are almost same. The lower surface pressure for wing without winglet increases up to 60% C and then decreases slowly towards the trailing edge. For wing with blended winglet as well, lower surface pressure increases from 20% C to 60% C and then decreases up to the trailing edge. For wing with spiroid winglet the lower surface pressure increases slowly from leading edge to trailing edge. The lower surface pressure for wing with double blended winglet is almost constant throughout the chord length. The pressure difference between upper and lower surfaces for wing without winglet and wing with blended winglet is highest from 40% C to 60% C and then this difference decreases gradually towards the trailing edge. For wing with spiroid winglet and wing with double blended winglet, the difference between upper and lower surface becomes maximum at 40% C.

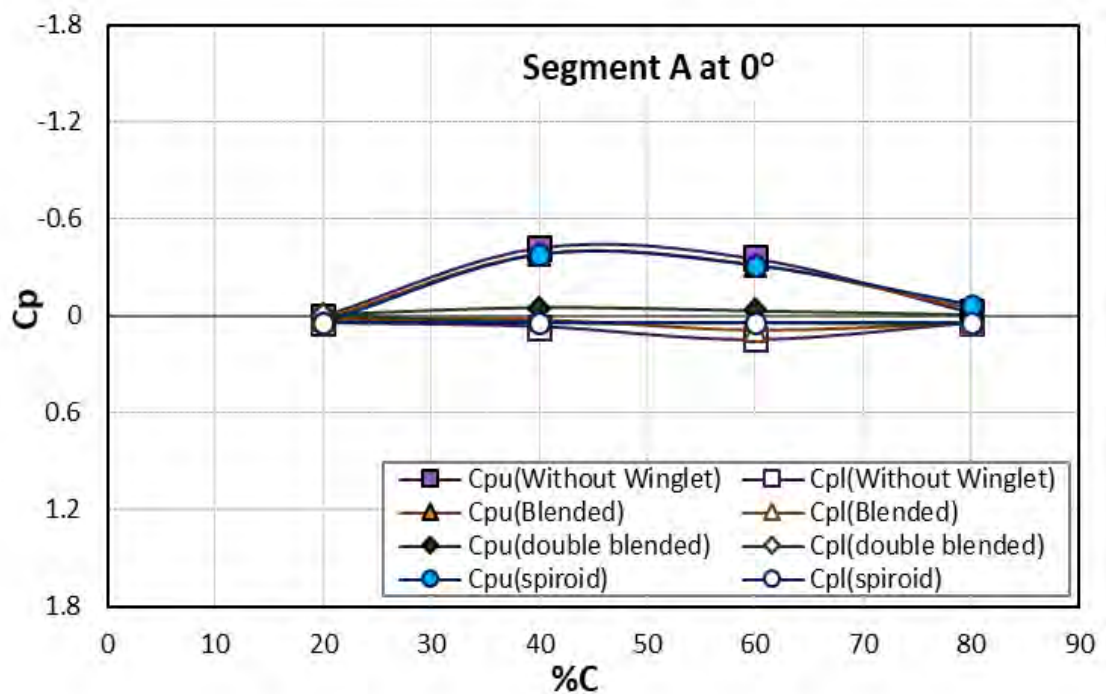


Figure 6.5: C_p Distribution of Segment-A at $\alpha = 0^\circ$

In Figure 6.6, the surface pressure distributions for Segment-B of the wing models at 0° AOA are shown. It is observed that upper surfaces of all the four planforms are

having higher negative pressure than the lower surfaces of the respective wing models. For wing without winglet, the upper surface pressure increases from leading edge to the trailing edge. The lower surface pressure increases from 20% C to 80% C as well. The difference between upper and lower surface pressure of wing without winglet reaches maximum at 20% C. For wing with blended winglet, upper surface pressure gradually increases from leading edge to the trailing edge and lower surface pressure increases slowly up to the trailing edge. The difference between upper and lower surface pressure of wing with blended winglet is highest at 20% C. For wing with spiroid winglet, upper surface pressure increases as well from leading edge to the trailing edge. But the lower surface pressure decreases up to 40% C and after that it increases towards the trailing edge. For wing with double blended winglet, upper surface pressure increases from 20% C to 80% C and lower surface pressure remains almost constant throughout the chord length. The overall pressure difference between upper and lower surface is highest for wing with blended winglet at Segment B.

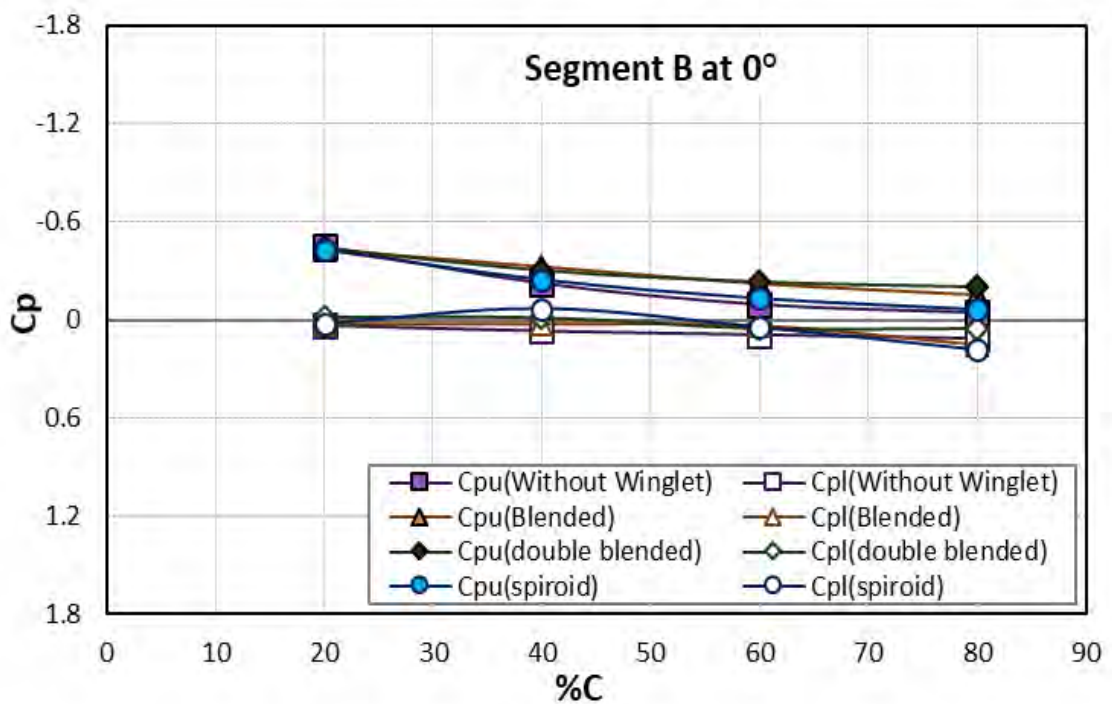


Figure 6.6: C_p Distribution of Segment-B at $\alpha = 0^\circ$

Figure 6.7 shows the upper and lower surface pressure distribution for segment- C of wing models. For wing without winglet, the upper surface is having higher negative pressure than the lower surface throughout the chord length except near the leading edge. The upper surface pressure decreases up to 40% C and then increases gradually up to the trailing edge. The lower surface pressure increases slowly from leading edge to the trailing edge. For wing with blended winglet, the upper surface is having greater negative pressure than the lower surface throughout the chord length. The upper surface pressure decreases up to 40% C and then increases towards the trailing edge. The lower surface pressure increases from leading edge to trailing edge. For wing with spiroid winglet, the upper surface negative pressure is higher than the lower surface throughout the chord length except near the leading edge. The upper surface pressure decreases up to 40% C and then increases gradually up to the trailing edge. The lower surface pressure increases slowly from 20% C to 80% C. For wing with double blended winglet, the upper surface negative pressure is higher than the lower surface throughout the chord length. The upper surface pressure decreases up to 40% of C and then increases slightly towards the trailing edge. But lower surface pressure remains almost constant throughout the chord length.

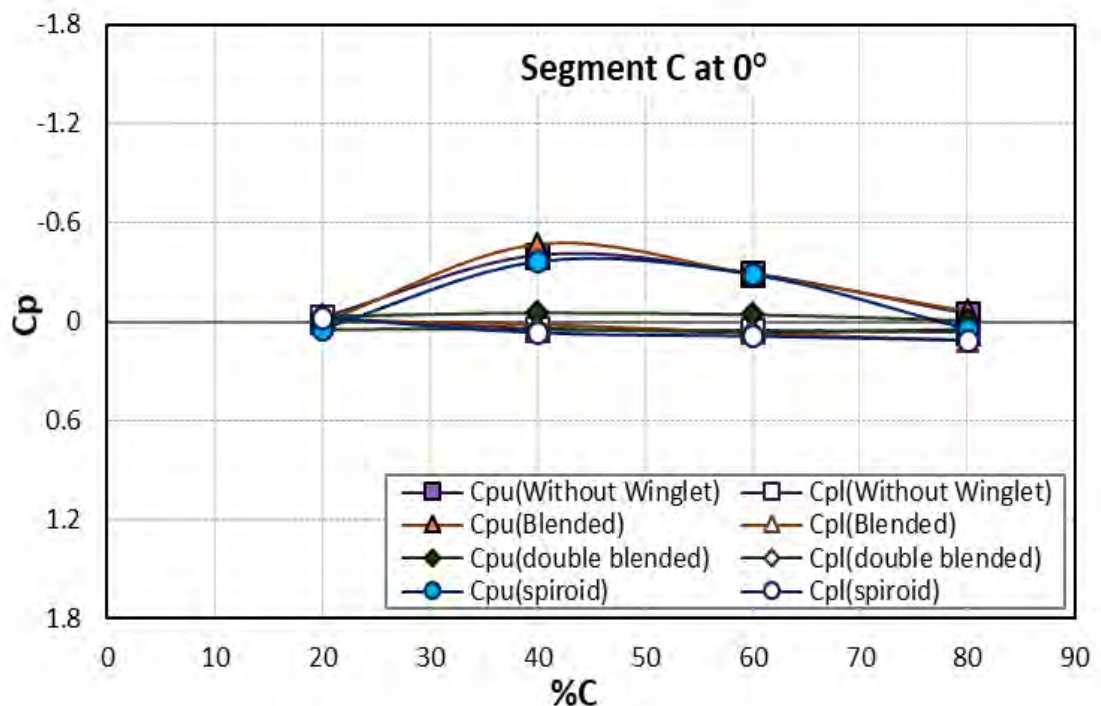


Figure 6.7: C_p Distribution of Segment-C at $\alpha = 0^\circ$

In Figure 6.8, the surface pressure distributions for Segment-D of wing models at 0° angle of attack are shown. From the figure, it is observed that upper surface of all wing models are having higher negative pressure than the lower surface pressure of the respective wing models except wing with spiroid winglet near the leading edge. For wing without winglet, the upper surface pressure decreases from 20% C to 40% C and then again increases up to the trailing edge. The lower surface pressure also reduces up to 40% C and then increases up to the trailing edge. For wing with blended winglet, the upper surface pressure decreases up to 40% C and then rises up to the trailing edge. The lower surface pressure increases from leading edge to trailing edge. For wing with spiroid winglet, the upper surface pressure decreases up to 40% C and then increases sharply towards the trailing edge. The lower surface pressure increases gradually from 20% C to 80% C. In case of the wing with double blended winglet, the upper surface pressure decreases up to 40% C and afterwards increases up to the trailing edge. But the lower surface pressure decreases slightly towards the trailing edge. The difference between upper and lower surface pressure is observed maximum at 40% C for all wing models.

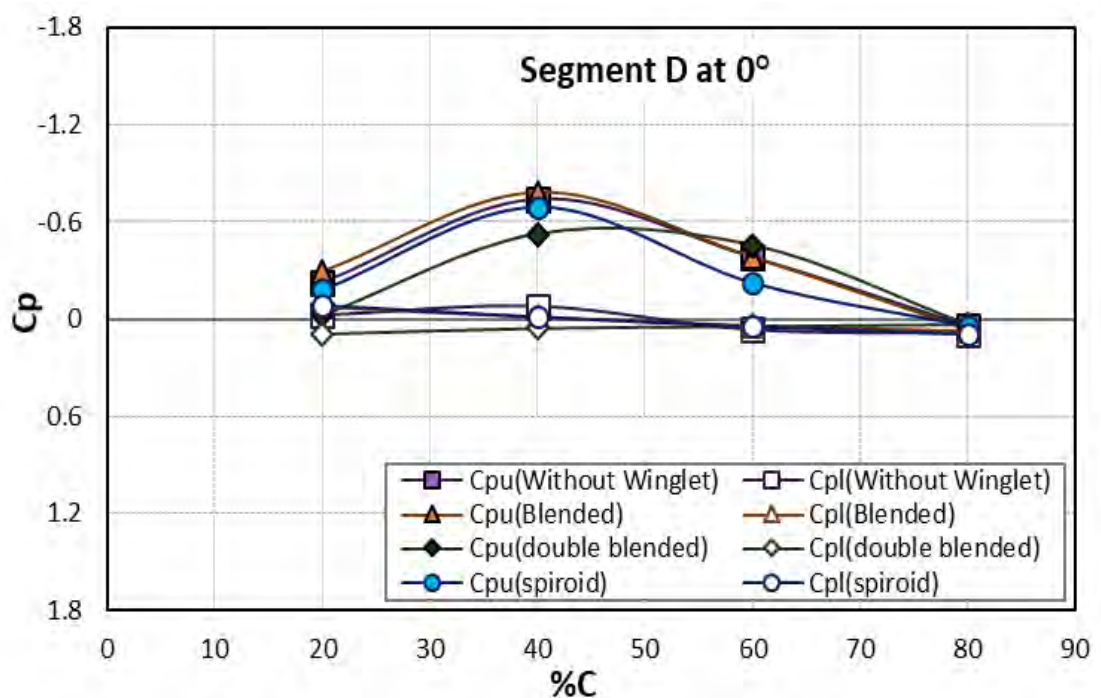


Figure 6.8: C_p Distribution of Segment-D at $\alpha = 0^\circ$

6.2.3 Pressure Distributions at 4° AOA

Figures 6.9, 6.10, 6.11 and 6.12 represent the surface pressure distribution in terms of pressure coefficient of four segments (A, B, C and D) of wing without winglet and wing with different winglet models at 4°. In the figures, both upper and lower surface pressure coefficient, C_{pu} and C_{pl} are plotted along the chord length (C).

From Figure 6.9 it is observed that pressure difference between the upper and lower surface of wing without winglet in segment A is highest amongst all the four wing models. The reason for this is that the upper surface pressure of wing without winglet is lower than that of other three wing models from 40% C to the trailing edge. It is also observed that the pressure difference between the two surfaces of wing with double blended winglet is the lowest as it's the upper surface pressure is higher than that of other wing models.

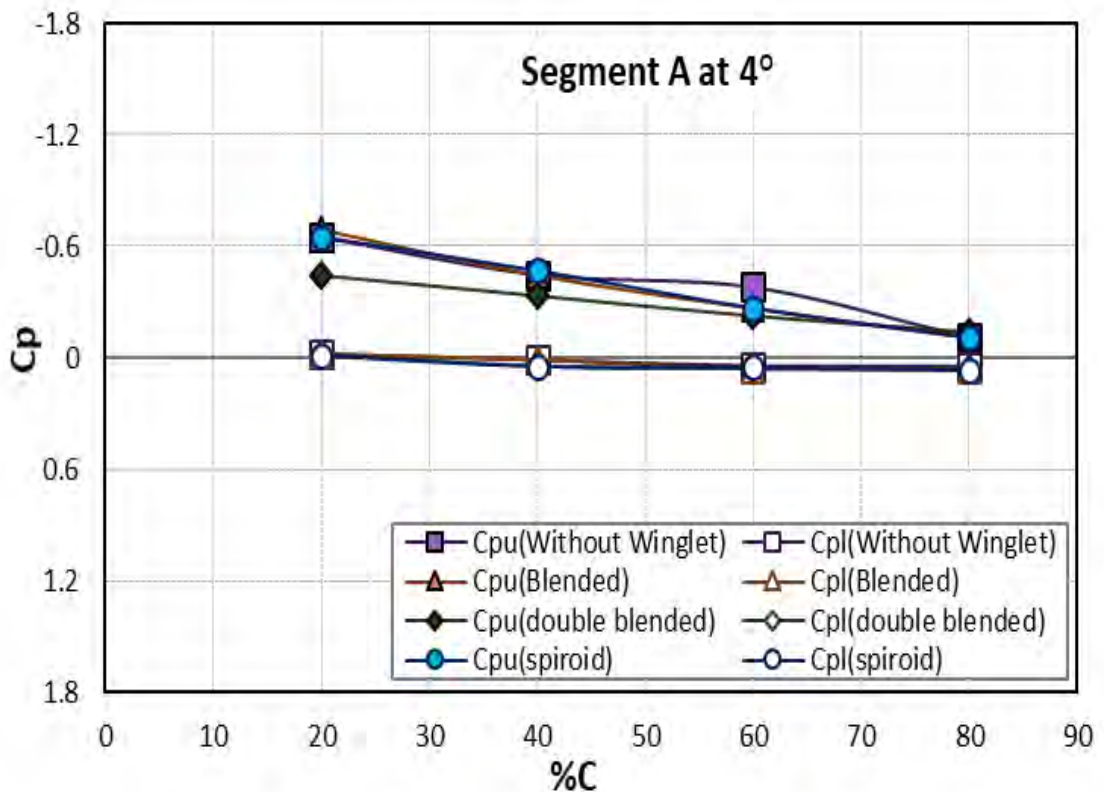


Figure 6.9: C_p Distribution of Segment-A at $\alpha = 4^\circ$

In Figure 6.10, it is observed that the upper surface of all wing models is having higher negative pressure than the lower surface of the respective wing model. The difference between upper and lower surface pressure is observed lowest for wing with double blended winglet and highest for wing without winglet. The upper surface pressure for all the wing models increases from leading edge to trailing edge. The upper surface pressure of wing without winglet is lowest amongst four wing models, highest for wing with spiroid winglet and in between these two for wing with blended winglet and wing with double blended winglet. Between wing with blended winglet and wing with double blended winglet, the upper surface pressure is lower for wing with blended winglet. The lower surface of wing with spiroid winglet is having higher positive pressure than that of other three wing models.

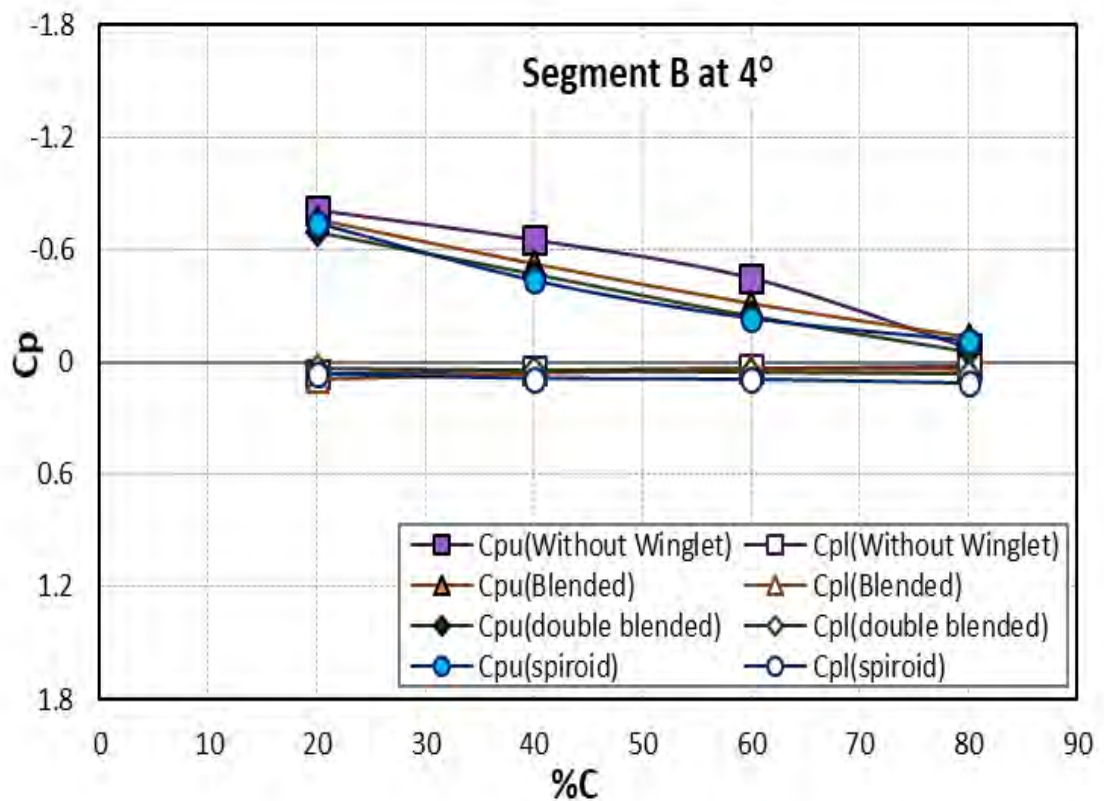


Figure 6.10: C_p Distribution of Segment-B at $\alpha = 4^\circ$

Figure 6.11 shows the pressure distribution for segment-C of wing models. From the figure, it is observed that the upper surface pressure is lowest for wing with blended winglet throughout the chord and highest for the wing with double blended winglet. The lower surface pressures of all the wing models remain at the positive pressure side throughout the chord length and are close to each other. As a result, the pressure difference between the upper and lower surface of the wing with blended winglet is highest. In figure 6.12, almost similar type of pressure distribution of wing models for segment D are observed as in segment C. At segment D as well, the difference between upper and lower surface is observed maximum for wing with blended winglet. But the pressure difference between two surfaces of respective wing models is higher than that of segment C.

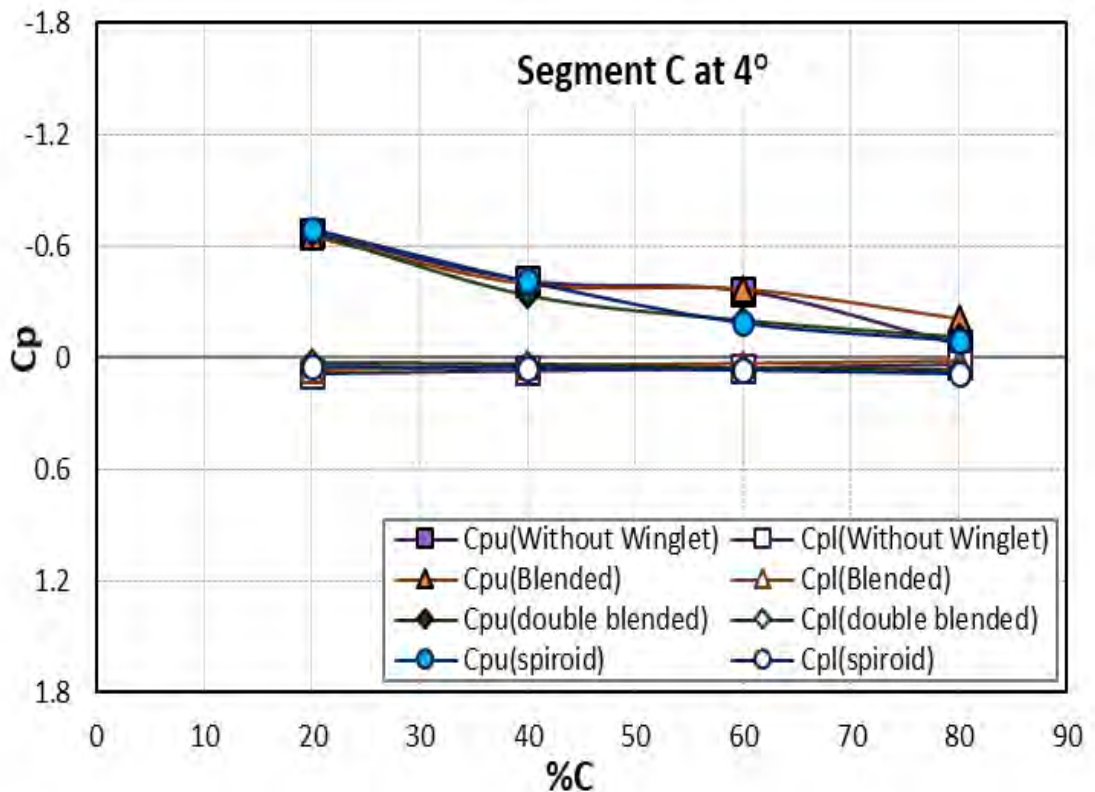


Figure 6.11: C_p Distribution of Segment-C at $\alpha = 4^\circ$

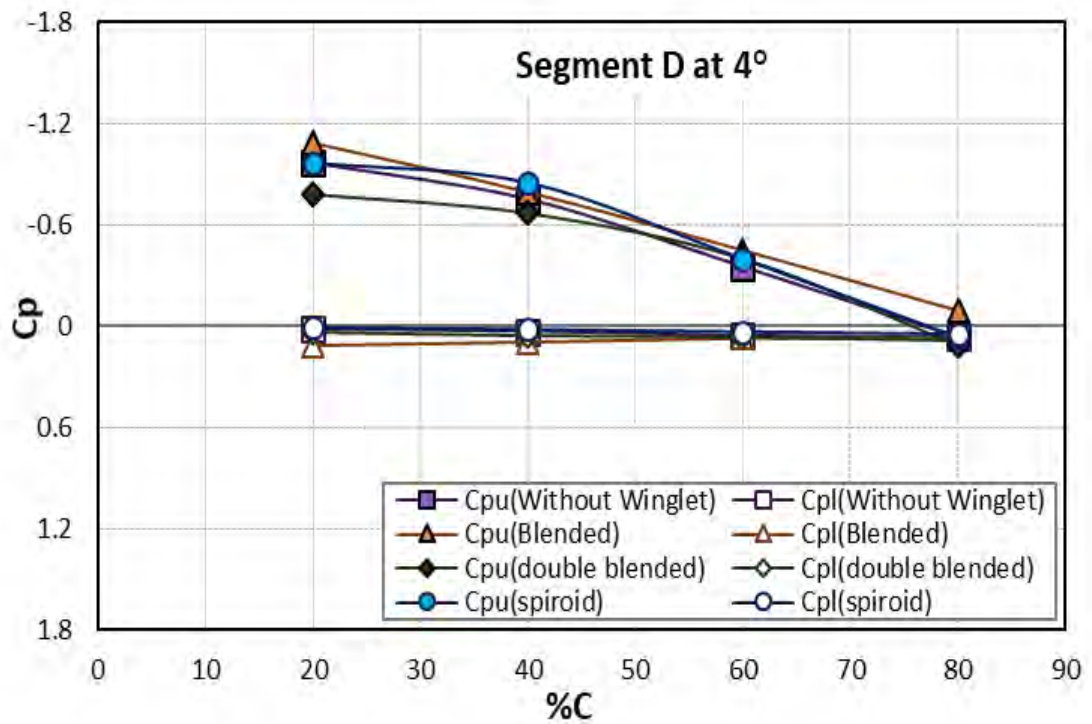


Figure 6.12: C_p Distribution of Segment-D at $\alpha = 4^\circ$

6.2.4 Pressure Distributions at 8° AOA

Figures 6.13, 6.14, 6.15 and 6.16 represent the surface pressure distribution in terms of pressure coefficient of four segments (A, B, C and D) of wing without winglet and wing with different winglet models at 8° AOA.

The surface pressure distributions for segment-A of wing models at 8° angle of attack are shown in Figure 6.13. From the figure it is seen that the upper surface of all wing models are having higher negative pressure than the lower surface pressure of the respective wing models. For all wing models, upper surface pressure increases gradually from leading edge to trailing edge. But lower surface pressure decreases slowly from leading edge to trailing edge. The upper surface pressure is observed to be lowest for wing with blended winglet and highest for wing with double blended winglet. But the lower surface pressure is greatest for wing with blended winglet. As a result, the difference between the upper and lower surface pressure of wing with

blended winglet becomes highest among four wing models. For all wing models, the largest difference between upper and lower surface is observed at 20% C.

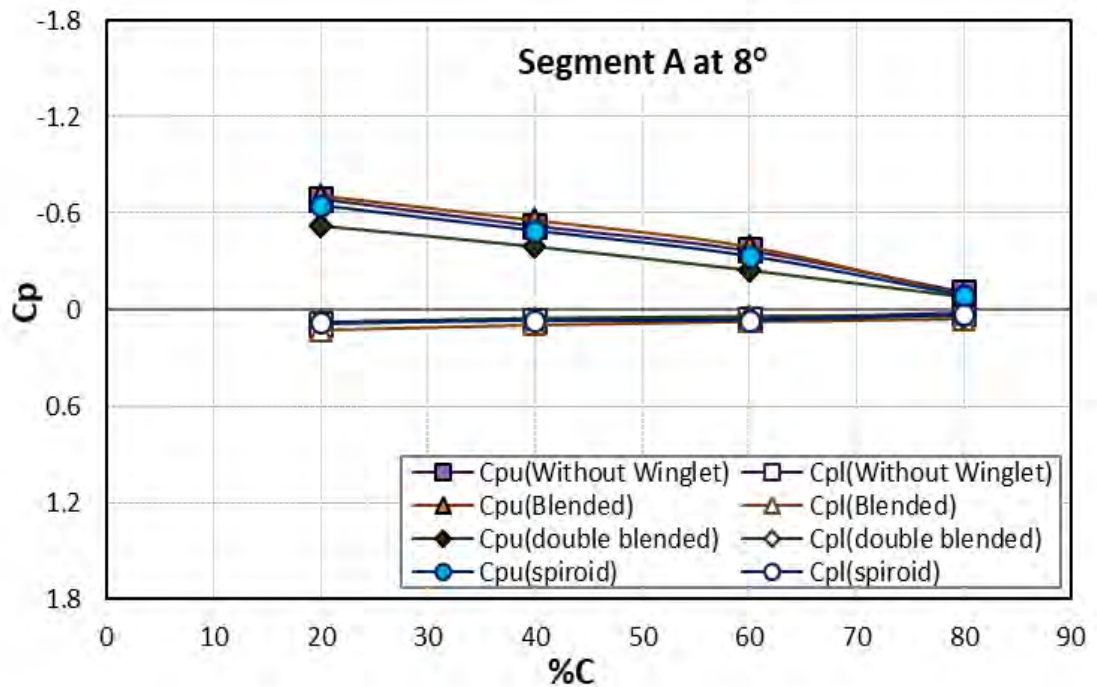


Figure 6.13: C_p Distribution of Segment-A at $\alpha = 8^\circ$

In Figure 6.14, the surface pressure distribution of segment B of wing models at 8° AOA is illustrated. It is observed that the upper surface of all wing models are having higher negative pressure than lower surface of the respective wing models. The difference between upper and lower surface pressure is observed lowest for wing with double blended winglet and highest for wing with blended winglet. The upper surface pressures for all wing models increase from 20% C to 80% C. But lower surface pressures decrease from leading edge to trailing edge. The upper surface pressure for wing with double blended winglet is highest and lowest for wing with blended winglet among four wing models. Between the wing with spiroid winglet and wing without winglet, the upper surface pressure is lower for wing without winglet. The lower surface pressure for wing with blended winglet is higher than that of other three wing models.

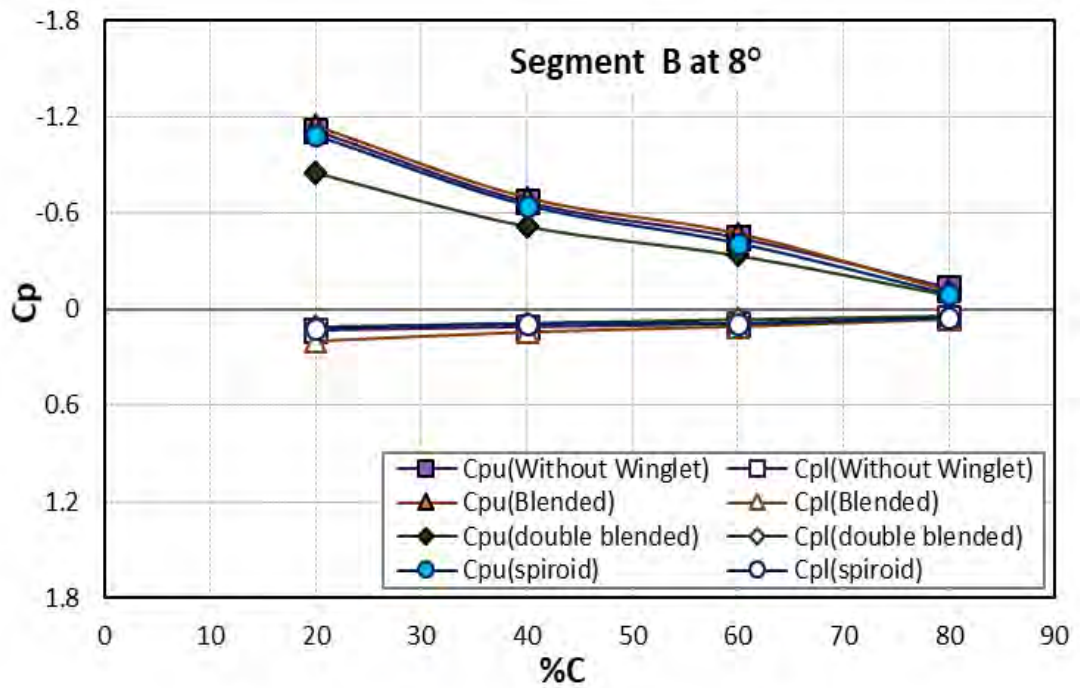


Figure 6.14: C_p Distribution of Segment-B at $\alpha = 8^\circ$

Figure 6.15 and Figure 6.16 show the pressure distribution of segment-C and segment-D of wing models respectively. From the figure 6.15, it is observed that upper surface pressure of all wing models increase from leading edge to trailing edge in segment-C. But lower surface pressures decrease from leading edge to trailing edge. It is also seen that the upper surface pressure is lowest for wing with blended winglet throughout the chord and highest for wing with double blended winglet. But the lower surface pressure of wing with blended winglet is highest amongst four wing models. As a result, the pressure difference between the upper and lower surface of wing with blended winglet is also at the highest level. Besides, the upper and lower surface pressure differences for wing without winglet is higher than wing with spiroid winglet and double blended winglet. From figure 6.16, it is observed that the difference between upper and lower surface pressures in segment-D is highest for wing with spiroid winglet. In segment-D, the pressure difference between two surfaces of respective wing models are lower than those of segment-C. The difference between upper and lower surfaces for all wing models become maximum at 20% C in both segment C and segment D.

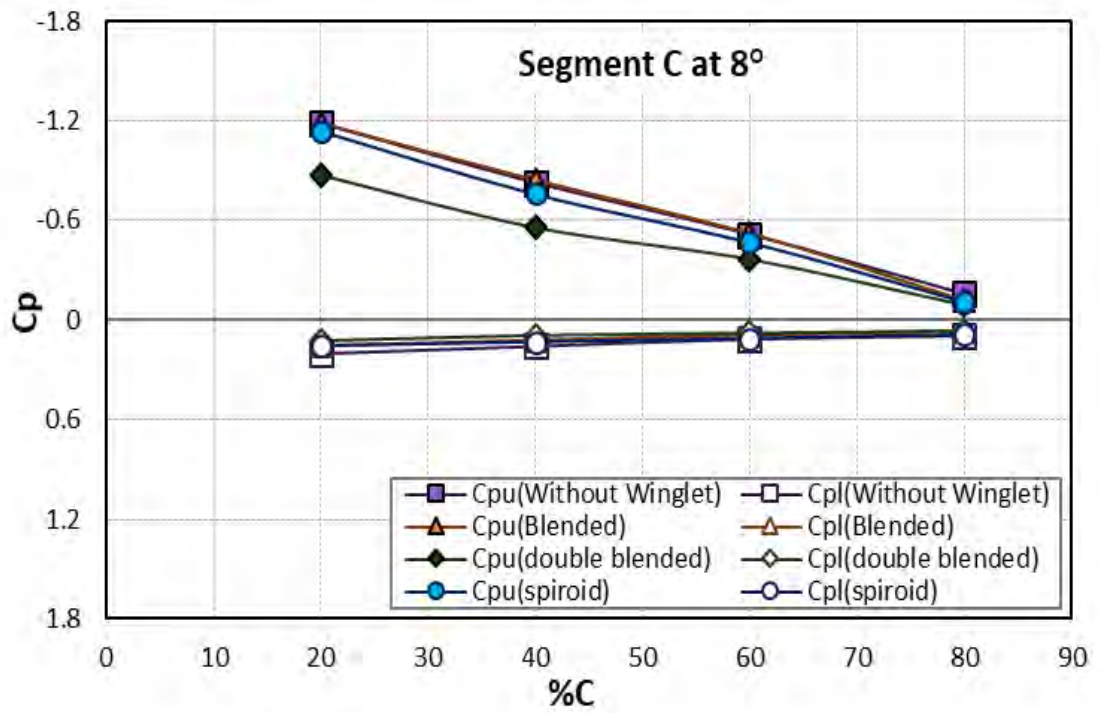


Figure 6.15: C_p Distribution of Segment-C at $\alpha = 8^\circ$

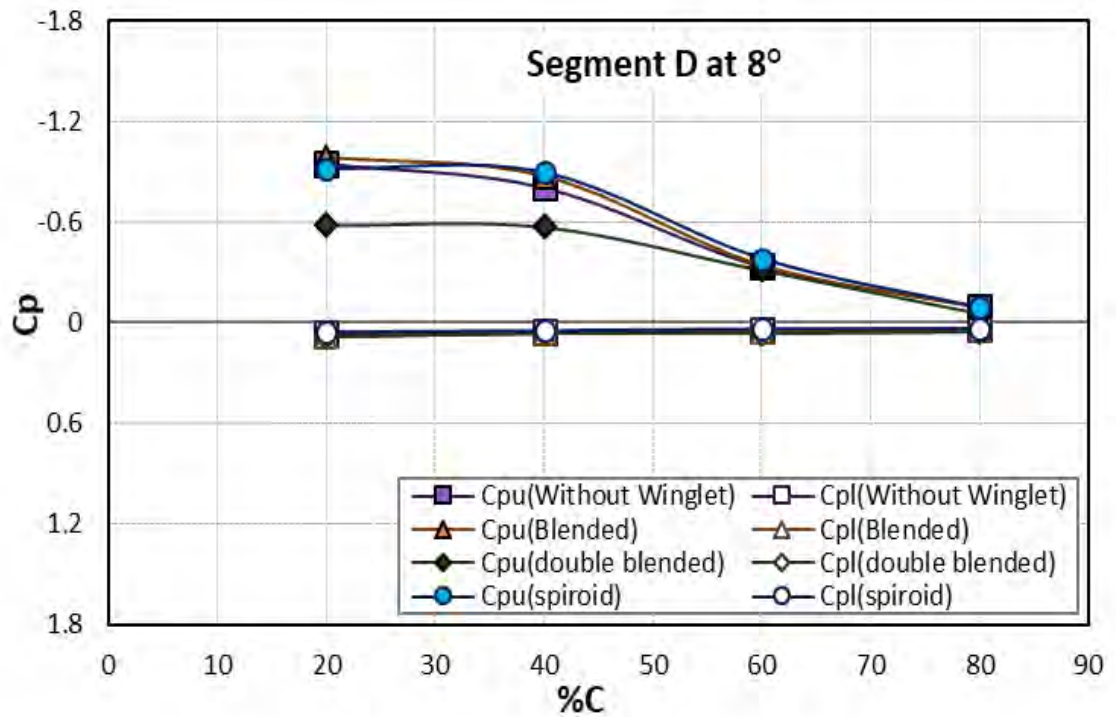


Figure 6.16: C_p Distribution of Segment-D at $\alpha = 8^\circ$

6.2.5 Pressure Distributions at 12° AOA

Figures 6.17, 6.18, 6.19 and 6.20 represent the surface pressure distribution in terms of pressure coefficient of four segments (A, B, C and D) of wing without winglet and wing with different winglet models at 12° AOA.

The surface pressure distributions for segment-A of wing models at 12° angle of attack are shown in Figure 6.17. From the figure, it is observed that upper surfaces of all wing models are having higher negative pressure than the lower surface pressure of the respective wing models. For wing without winglet, the lower surface pressure decreases slowly from 20% C to 80% C. The upper surface pressure increases gradually from leading edge to trailing edge. For wing with blended winglet as well, upper surface pressure increases and lower surface pressure decreases from leading edge to the trailing edge.

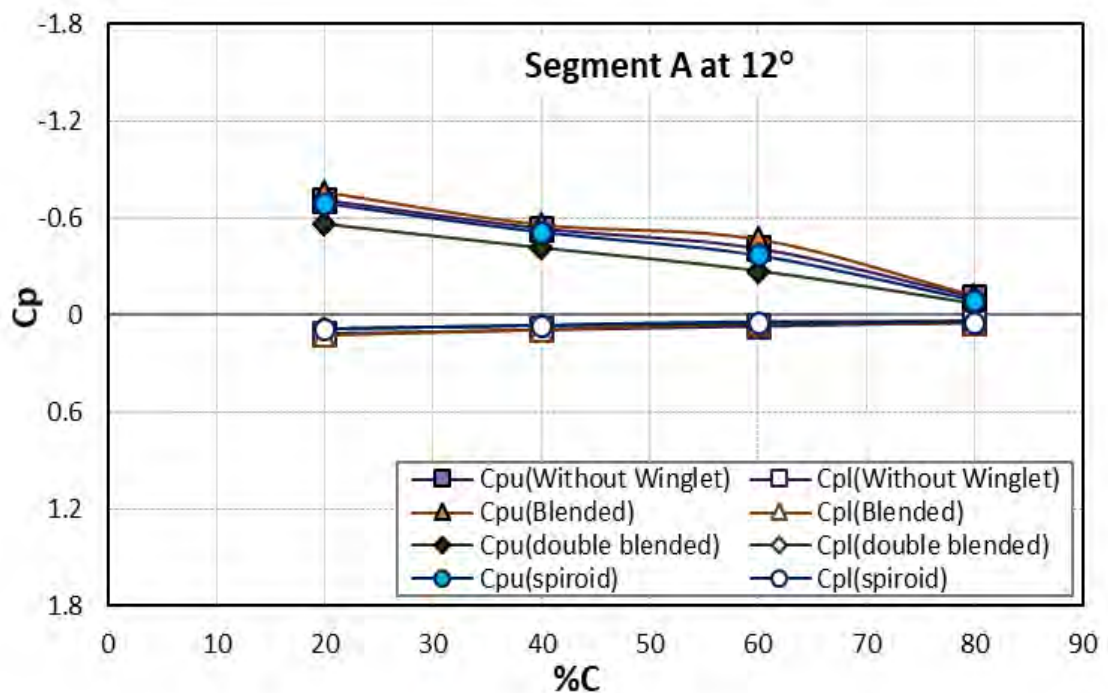


Figure 6.17: C_p Distribution of Segment-A at $\alpha = 12^\circ$

Similarly, for wing with spiroid winglet and wing with double blended winglet upper surface pressure rises gradually and lower surface pressure decreases slowly from leading edge to trailing edge. But the upper surface pressure is lowest for wing with blended winglet and lower surface pressure is highest for wing with blended winglet as well. As a consequence, the difference between upper and lower surface pressure is observed maximum for wing with blended winglet.

From Figure 6.18, it is seen that the upper surface pressures of wing models increase from leading edge to trailing edge and the lower surface positive pressures reduce from leading edge to trailing edge in segment-B. Thus the pressure difference between upper and lower surface is maximum near the leading edge at 20% C. Also, the overall pressure difference between upper and lower surface is maximum for wing with blended winglet and lowest for wing double blended winglet in segment-B.

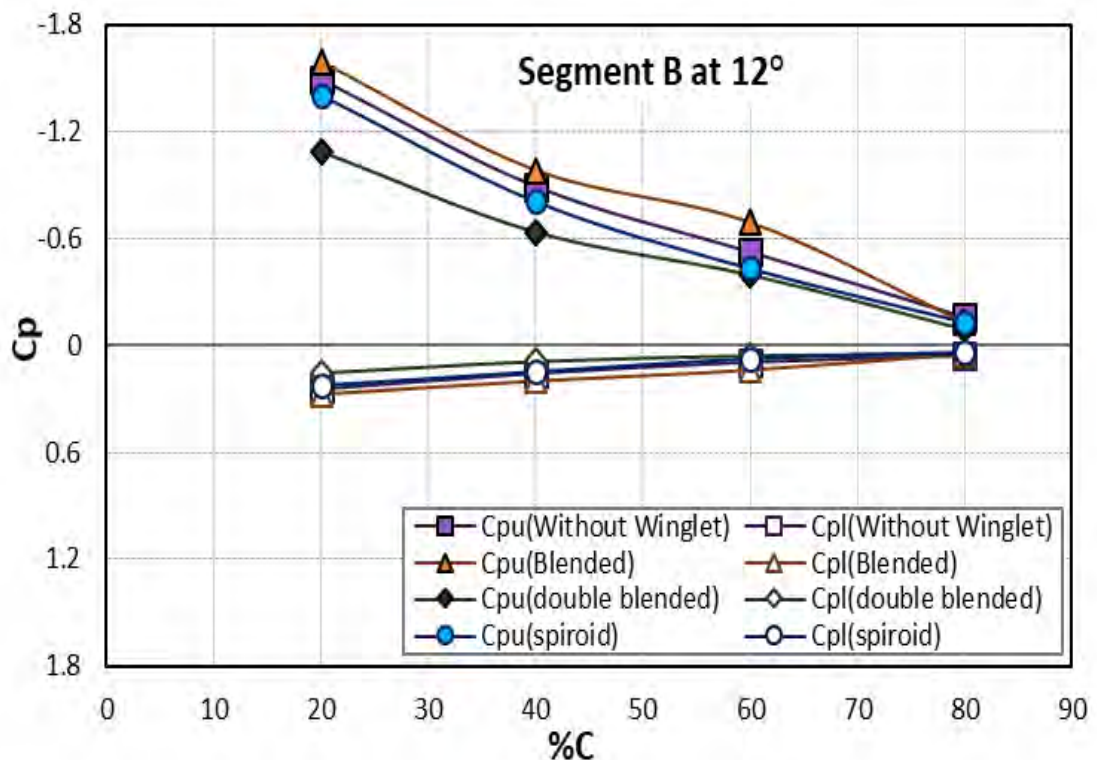


Figure 6.18: C_p Distribution of Segment-B at $\alpha = 12^\circ$

Figures 6.19 and 6.20 show the pressure distribution of segment C and segment D of wing models. In segment-C, the difference between upper and lower surface pressure becomes maximum again for wing with blended winglet as shown in Figure 6.19. In this segment as well, both the upper surface negative pressure and lower surface pressure of wing with blended winglet is greater than that of other wing models. In segment-D, overall pressure differences between upper and lower surfaces of wing models seem to be smaller than other segments as shown in Figure 6.20. For wing with spiroid winglet, the difference between upper and lower surface pressure is greatest among all wing models in segment D. From Figure 6.20, it is also seen that the upper surface pressure of wing models increases rapidly up to 60% C but the lower surface pressure decreases slowly from leading edge to trailing edge. From 60% C to 80% C, the difference between two surfaces' pressures of individual wing model changes very slowly.

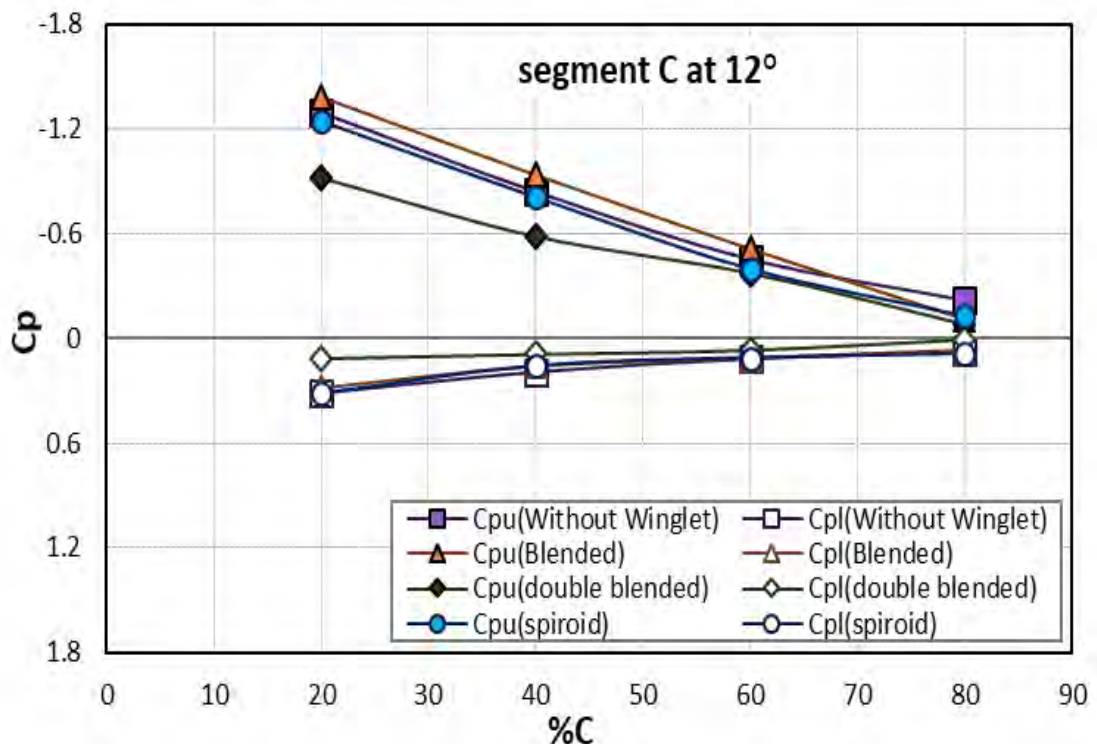


Figure 6.19: C_p Distribution of Segment-C at $\alpha = 12^\circ$

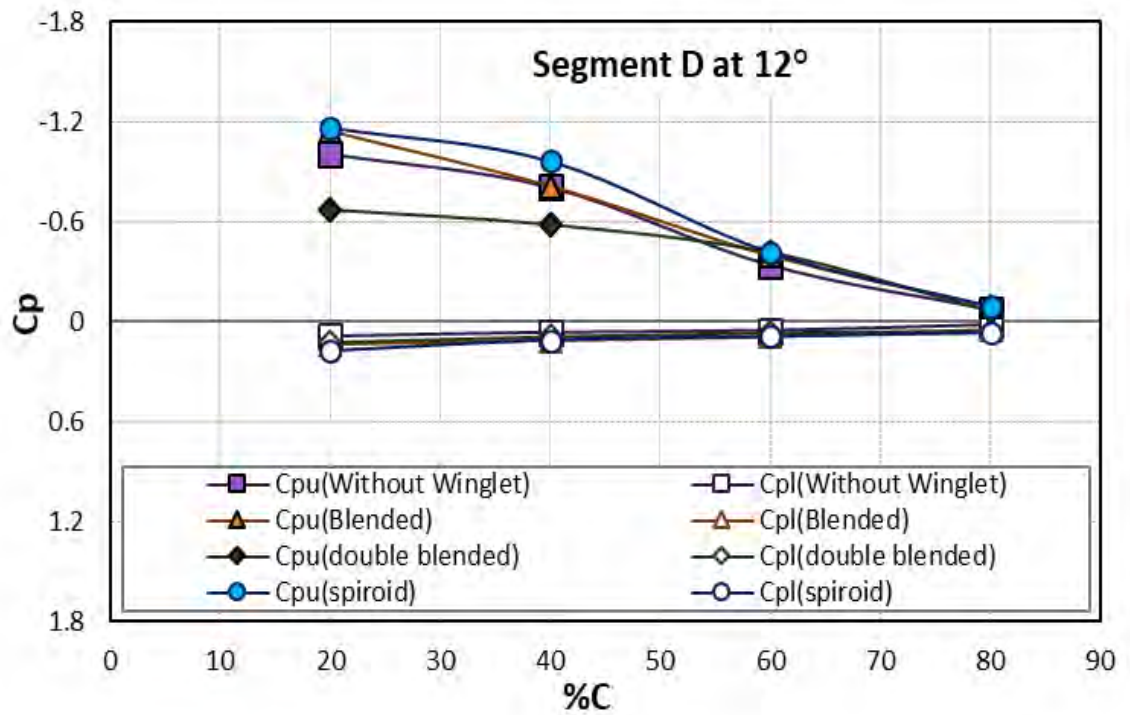


Figure 6.20: C_p Distribution of Segment-D at $\alpha = 12^\circ$

6.2.6 Pressure Distributions at 16° AOA

Figures 6.21, 6.22, 6.23 and 6.24 represent the surface pressure distribution in terms of pressure coefficient of four segments (A, B, C and D) of wing without winglet and wing with different winglet models at 16° AOA.

Pressure distribution along the chord for segment A is shown in Figure 6.21. From the graph, it is observed that upper surface pressure of wing models increases from 20% C to 60% C rapidly, then increases slowly up to 80% C. The lower surface positive pressure gradually decreases up to 60% C and finally reaches to almost constant pressure from 60% C to 80% C. The largest upper and lower surface pressure difference occurs at 20% of C for all wing models which reduces gradually towards the trailing edge. Wing with blended winglet has the highest surface pressure difference between upper and lower surfaces while wing with double blended winglet has the lowest pressure difference between upper and lower surfaces.

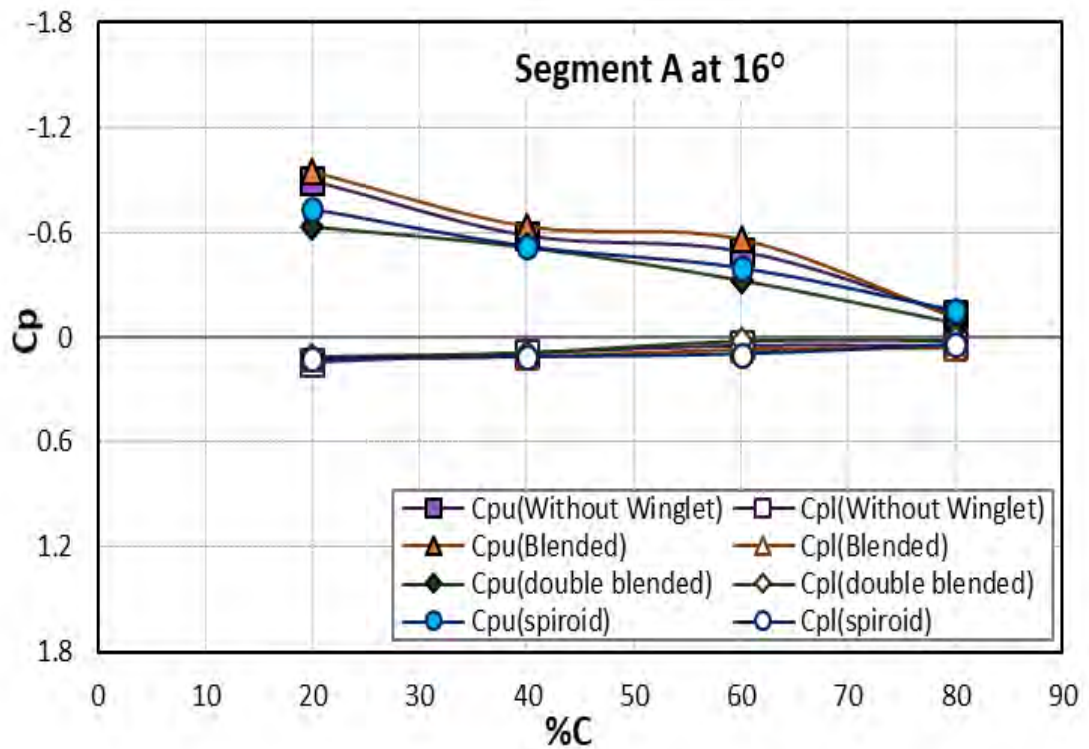


Figure 6.21: C_p Distribution of Segment-A at $\alpha = 16^\circ$

Similarly, Figures 6.22, 6.23 and 6.24 show the surface pressure distribution of segment B, C and D respectively for wing models at 16° angle of attack. In segment B, upper surface pressure increases gradually from leading edge to trailing edge for wing without winglet, wing with blended winglet and wing with double blended winglet. But for wing with spiroid winglet, upper surface pressure rises suddenly up to 40% C and then increases slowly towards the trailing edge. In segment C, upper surface pressure increases gradually from 20% C to 80% C for wing with blended winglet and wing with double blended winglet. But upper surface pressures of wing without winglet and wing with spiroid winglet increase rapidly up to 60% C and then increase slowly up to the trailing edge. In segment D, upper surface pressure increase gradually and lower surface pressure decrease slowly from leading edge to trailing edge. From the figures, it is also observed that overall pressure difference between the upper and lower surface of wing with blended winglet is higher than that of other wing models in segment B and C. But in segment-D pressure difference between the surfaces is highest for wing with spiroid winglet..

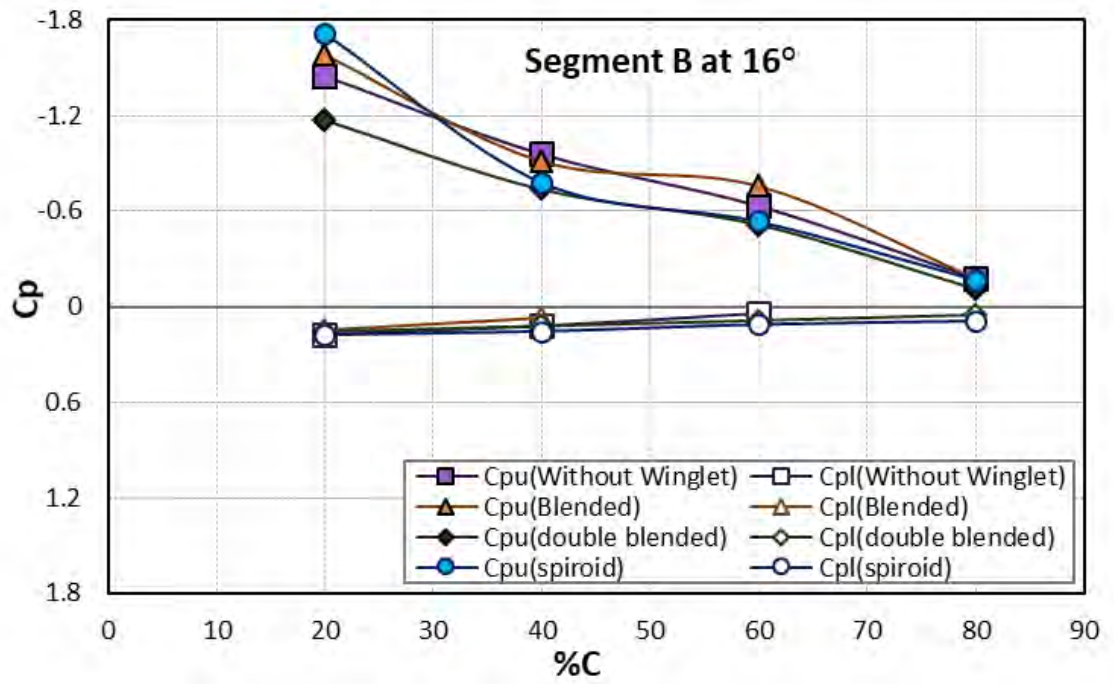


Figure 6.21: C_p Distribution of Segment-B at $\alpha = 16^\circ$

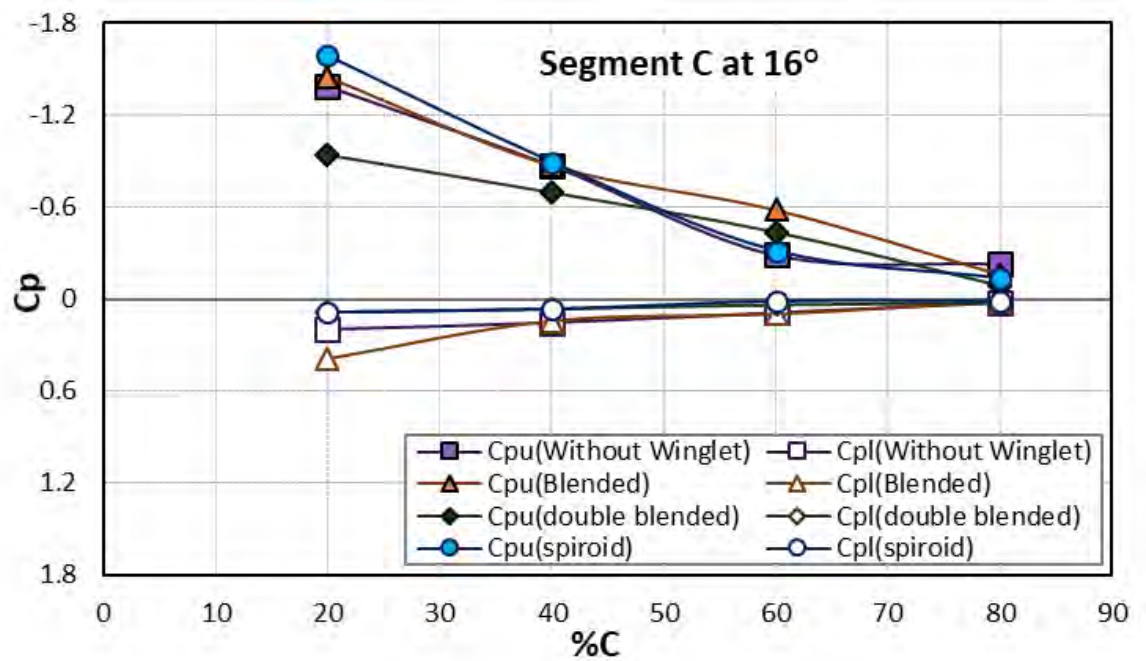


Figure 6.23: C_p Distribution of Segment-C at $\alpha = 16^\circ$

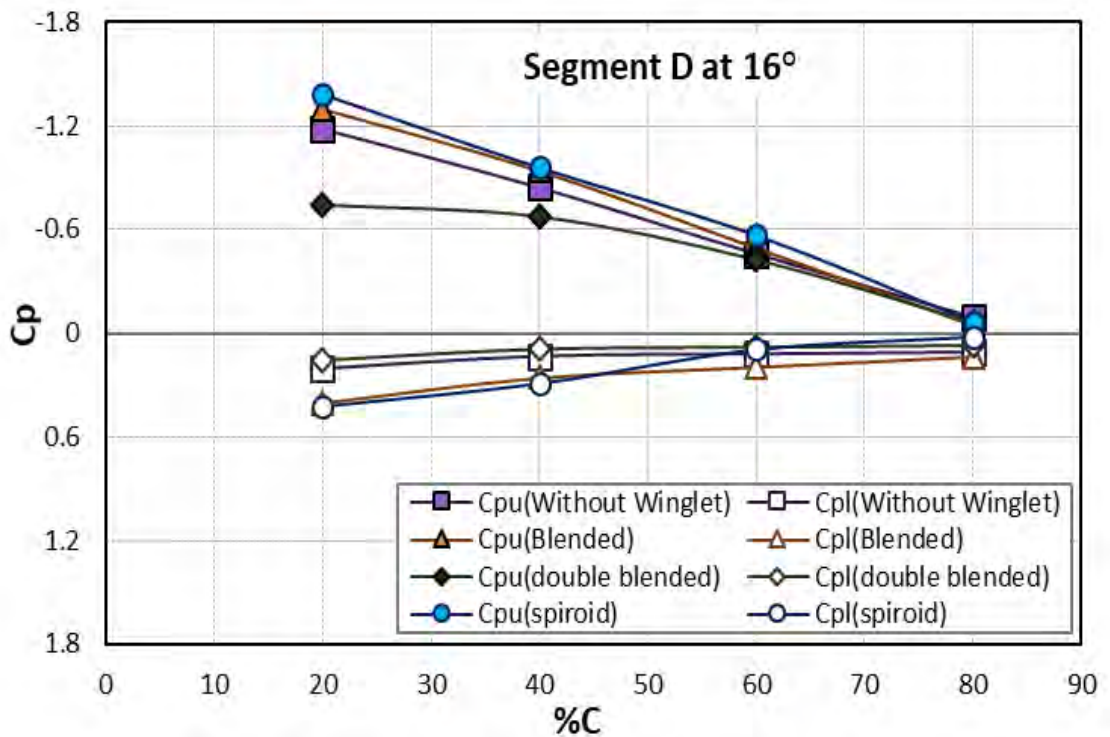


Figure 6.24: C_p Distribution of Segment-D at $\alpha = 16^\circ$

6.2.7 Pressure Distributions at 20° AOA

The surface pressure distributions along the chord length at 20° angle of attack for four segments of wing models are shown in Figures 6.25, 6.26, 6.27 and 6.28. From all the four figures, it is observed that in all segments the upper surface pressures of the wing models are much higher than the upper surface pressure at previous angle of attack (16° and below) as shown in the previous figures. Upper surface pressures of the models tend to increase at a much slower rate compared to the upper surface pressure rise at smaller angle of attack. The surface pressure difference between upper and lower surface of wing models is highest at 20% of C which decreases slowly up to the trailing edge in four segments. In Figure 6.25 and Figure 6.26 it is observed that, the overall differences between upper and lower surface pressure of wing with blended winglet and wing with spiroid winglet are observed maximum at segment A and segment B respectively. But in segment C and segment D, the said difference is maximum for wing with blended winglet and wing without winglet respectively as shown in Figure 6.27 and Figure 6.28.

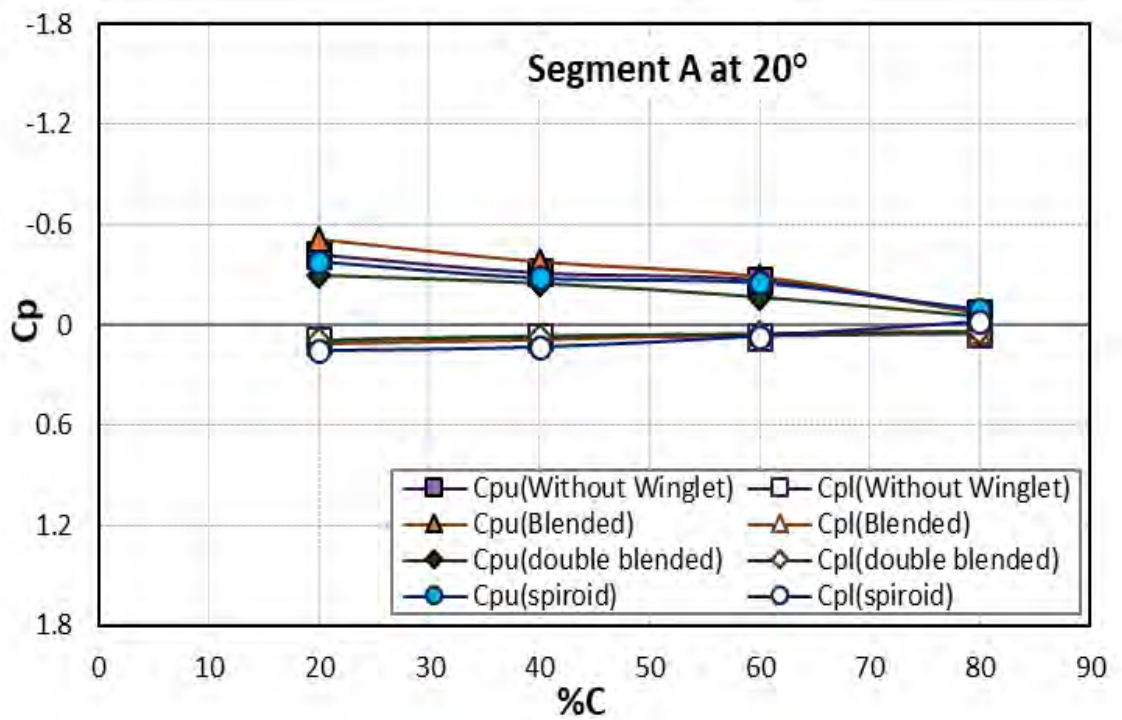


Figure 6.25: C_p Distribution of Segment-A at $\alpha = 20^\circ$

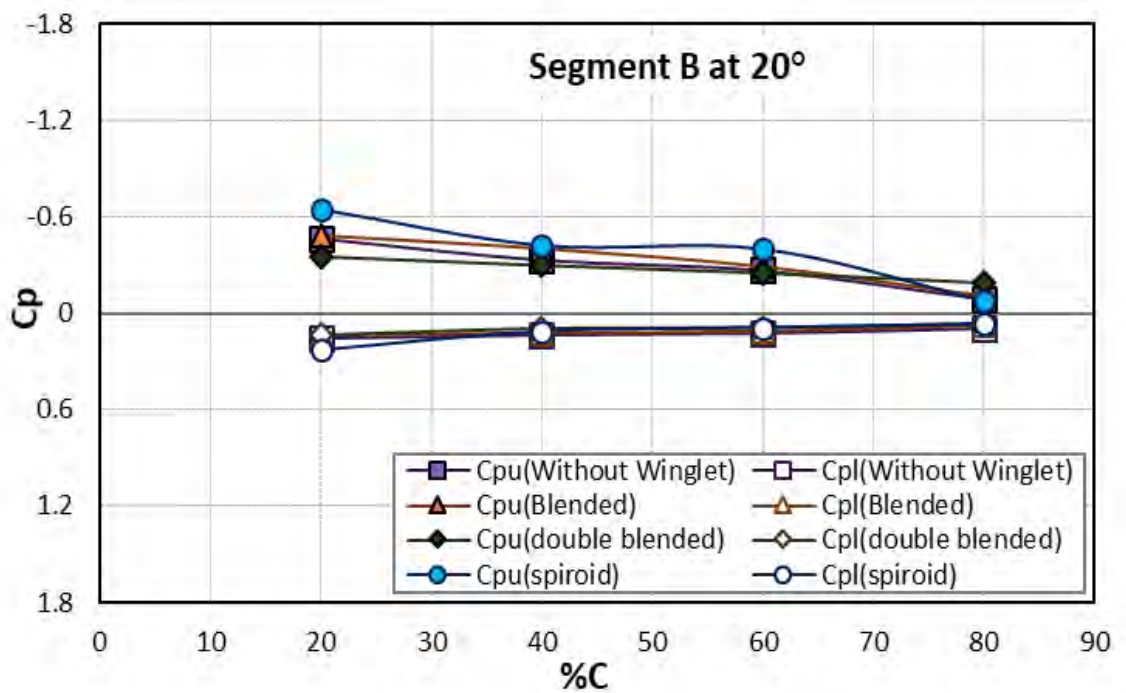


Figure 6.26: C_p Distribution of Segment-B at $\alpha = 20^\circ$

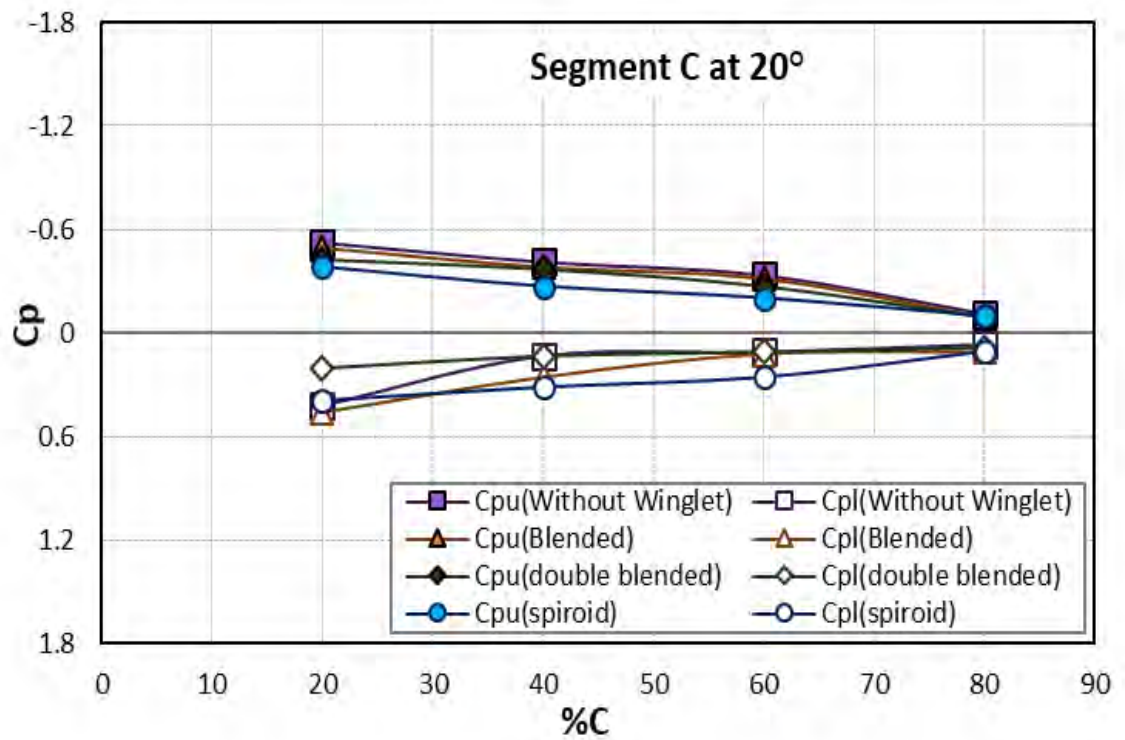


Figure 6.27: C_p Distribution of Segment-C at $\alpha = 20^\circ$

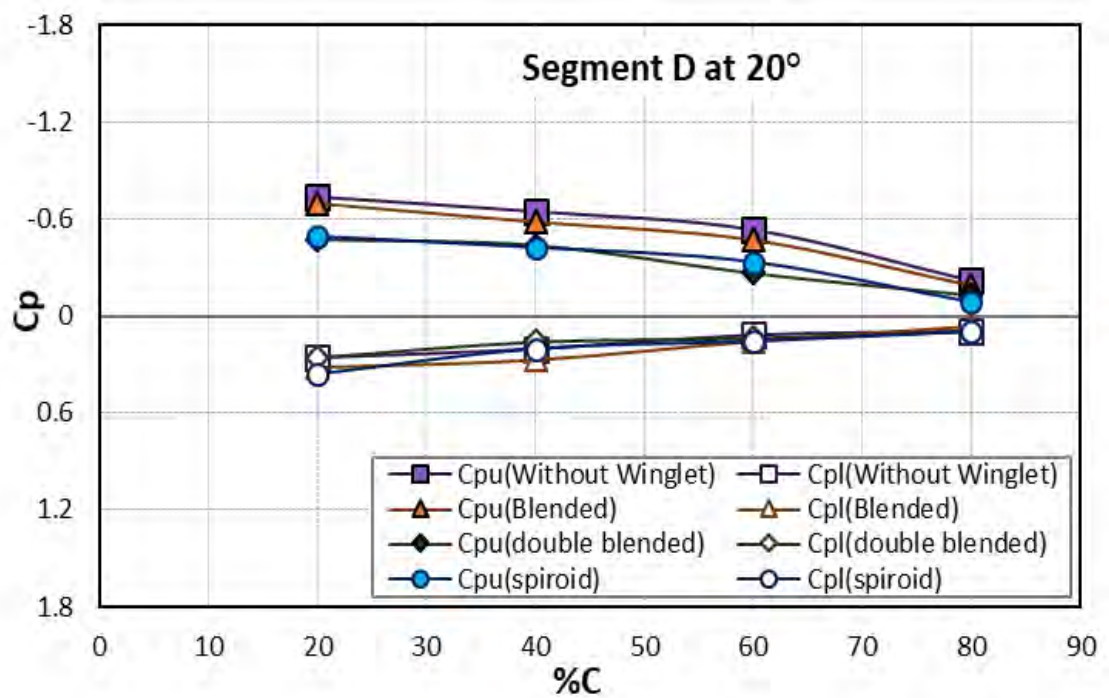


Figure 6.28: C_p Distribution of Segment-D at $\alpha = 20^\circ$

From Figures 6.25, 6.26, 6.27 and 6.28, it is also observed that pressure difference between upper and lower surfaces of wing models are higher in segment C and segment D compared to the pressure difference of the surfaces in segment A and segment B. Another observation from the figures is that the upper and lower surface pressures of wing models follow almost similar pattern in four segments.

6.2.8 Pressure distribution at 24° AOA

Figures 6.29, 6.30, 6.31 and 6.32 represent the surface pressure distribution in terms of pressure coefficient of four segments (A, B, C and D) of wing without winglet and wing with different winglet models at 24°. In the figures, both upper and lower surface pressure coefficient, C_{pu} and C_{pl} are plotted along the chord length (C).

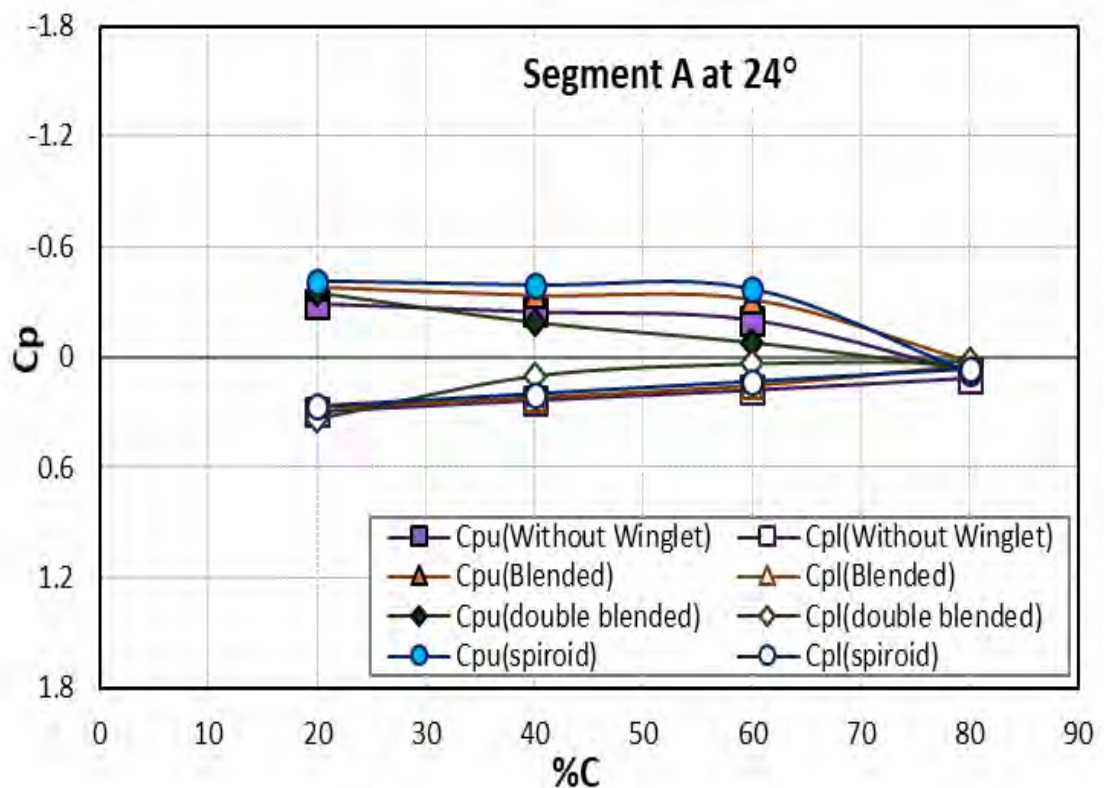


Figure 6.29: C_p Distribution of Segment-A at $\alpha = 24^\circ$

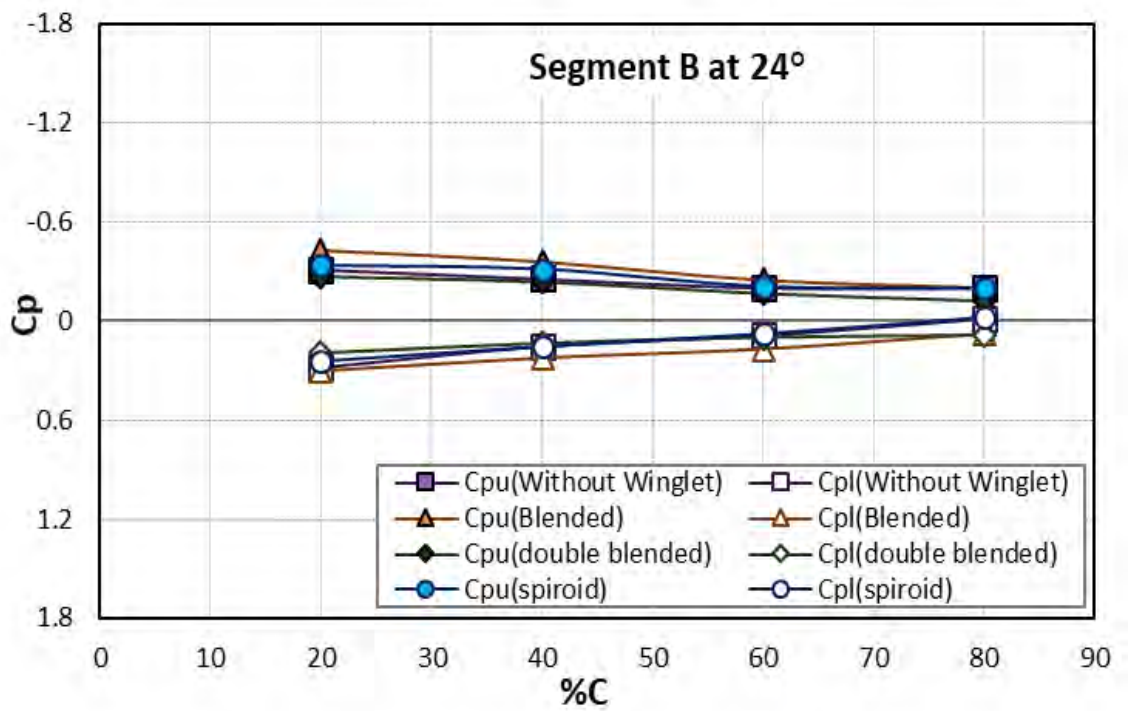


Figure 6.30: C_p Distribution of Segment-B at $\alpha = 24^\circ$

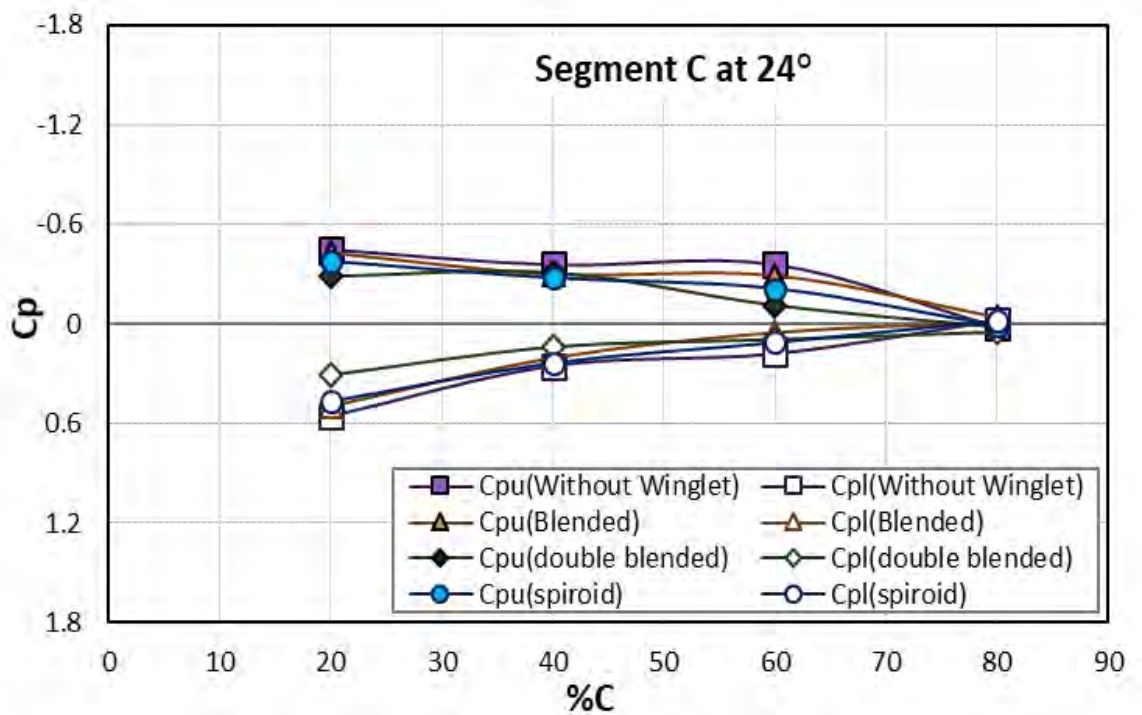


Figure 6.31: C_p Distribution of Segment-C at $\alpha = 24^\circ$

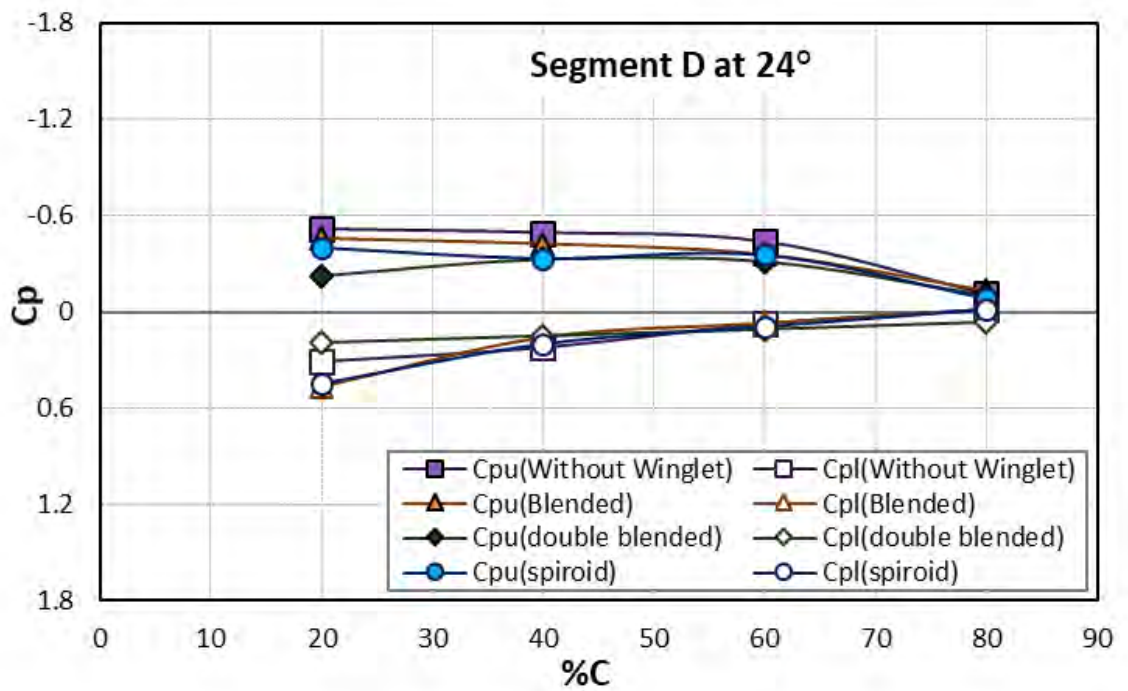


Figure 6.32: C_p Distribution of Segment-D at $\alpha = 24^\circ$.

In all the four segments at 24° angle of attack, it is observed that the pressure difference between upper and lower surface of all wing models are much lower compared to those at previous angle of attack. Among four wing models, wing with spiroid winglet is having higher pressure difference between upper and lower surfaces in segment A. But in segment B, the pressure difference between the two surfaces are found maximum for wing with blended winglet. The said difference is highest for wing without winglet in both segment C and segment D as shown in Figures 6.31 and 6.32.

6.3 Lift Characteristics

The lift characteristics of wing models at different angles are shown in Figure 6.33. The lift increases with increase in angle of attack to a maximum value. After this maximum value of angle of attack, lift decreases drastically due to flow separation over the aerofoil surface. From the figure, it is seen that the lift coefficient curve goes up from -4° angle of attack up to 16° angle of attack for all the wing models and then drops suddenly after 16° angle of attack. Thus, the critical angle of attack of all wing models is around 16° beyond which the stall happens. It is also observed that the lift coefficient for wing with blended winglet is much higher than other wing models. These statistics show the similar nature to Nazmul analysis [40], National Aerofoil Data NACA 4412 [50], Pinkerton analysis [51] and Agarwal analysis [52]. But in case of Pinkerton analysis, stall occurs at around 12° AOA because aspect ratio of the wing in Pinkerton analysis is 6 whereas aspect ratio of the wing in present analysis is 2.69. It is known that low aspect ratio wing has lower lift slope and stalls at higher AOA than high aspect ratio wing [53]. As a result, stall occurs at higher AOA i.e. at around 16° in present analysis.

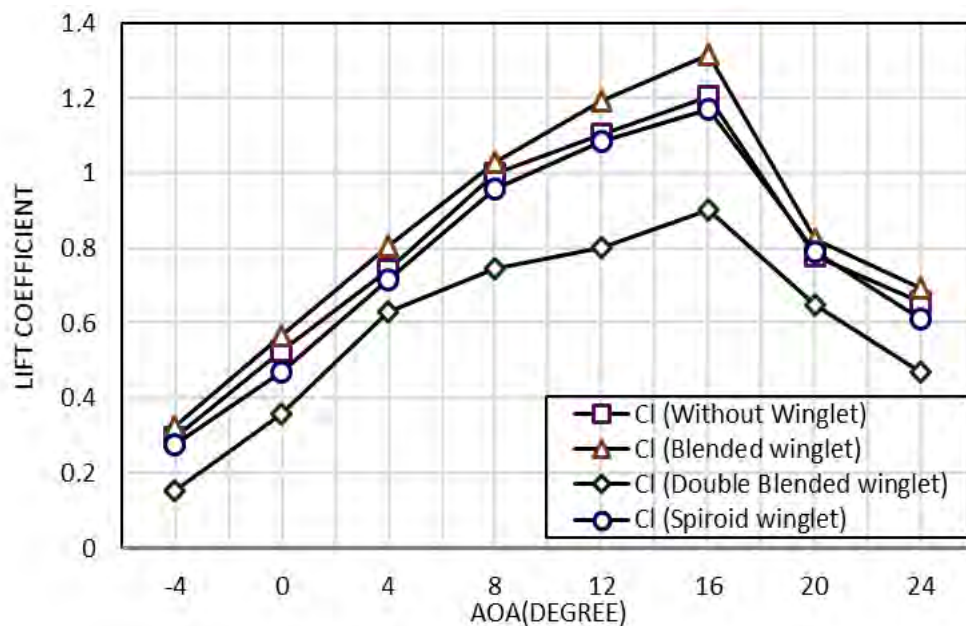


Figure 6.33: Variation of Lift Coefficient with Angle of Attack.

6.4 Drag Characteristics

Figure 6.34 illustrates the drag coefficients of the wing models under test for different angle of attack (AOA). It is observed that the values of drag coefficient for wings with spiroid winglet and double blended winglet are much lower than that of the wing without winglet and wing with blended winglet. The drag increases with a slower rate initially from -4° to 8° angle of attack. But from 8° to 24° angle of attack significant rise in drag is observed. It is seen that the coefficient of drag starts to rise suddenly after critical angle of attack at 16° . This sudden increase in drag coefficient occurs because the air detaches from the surface of the airfoil due to strong adverse pressure gradient after stalling angle of attack. These results are in terms with Nazmul analysis [40] and National Aerofoil Data NACA 4412 [50].

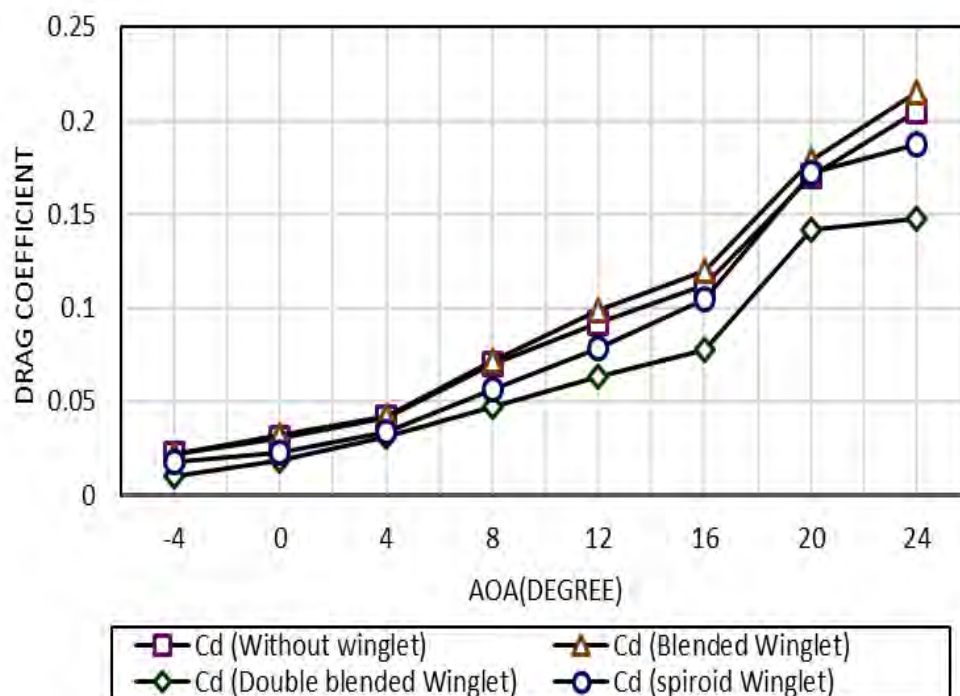


Figure 6.34: Variation of Drag Coefficient with Angle of Attack.

6.5 Lift to Drag Ratio

The values of lift to drag ratio are plotted for various angle of attack in Figure 6.35. From this graph it is observed that the lift to drag ratio for wing with spiroid winglet and wing with double blended winglet is remarkably higher (wing with spiroid winglet is higher than double blended winglet) than other two wing models. It is also evident that the wing without winglet has the lowest lift to drag ratio compared to wing with winglet models. It can be found that the pattern of the lift to drag ratio shows similar trend with National Aerofoil Data NACA 4412 [50].

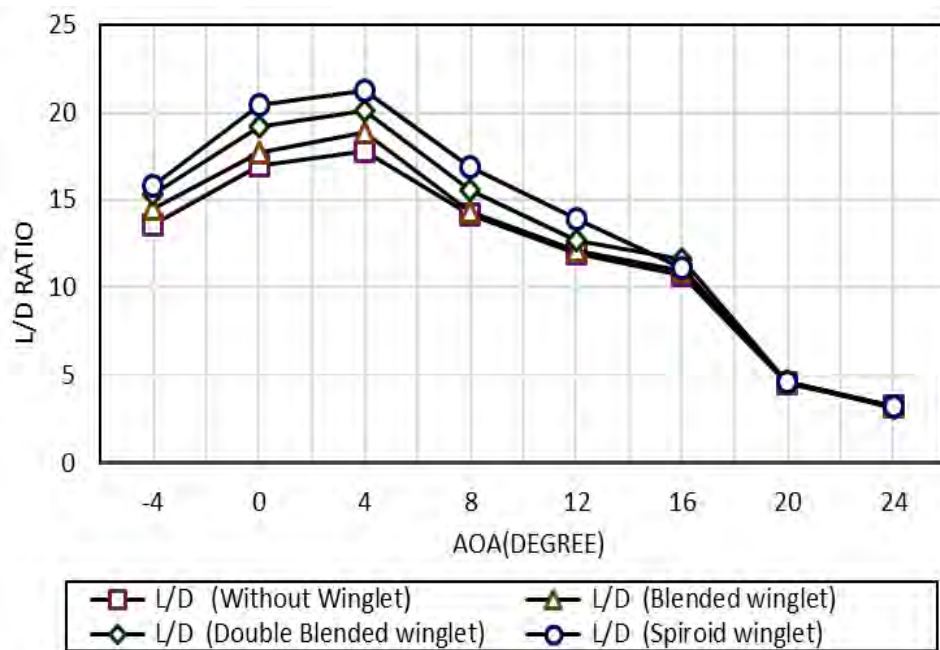


Figure 6.35: Variation of Lift to Drag Ratio with Angle of Attack

6.6 Induced Drag

Figure 6.36 shows the induced drag coefficients of the wing models under test for different angle of attack(AOA). The figure shows that the induced drag for wing without winglet is greater than wing with winglets. Among the three wing with winglets, induced drag is lowest for wing with double blended winglet. In comparison to induced drag for wing with blended winglet, induced drag is lower for wing with spiroid winglet.

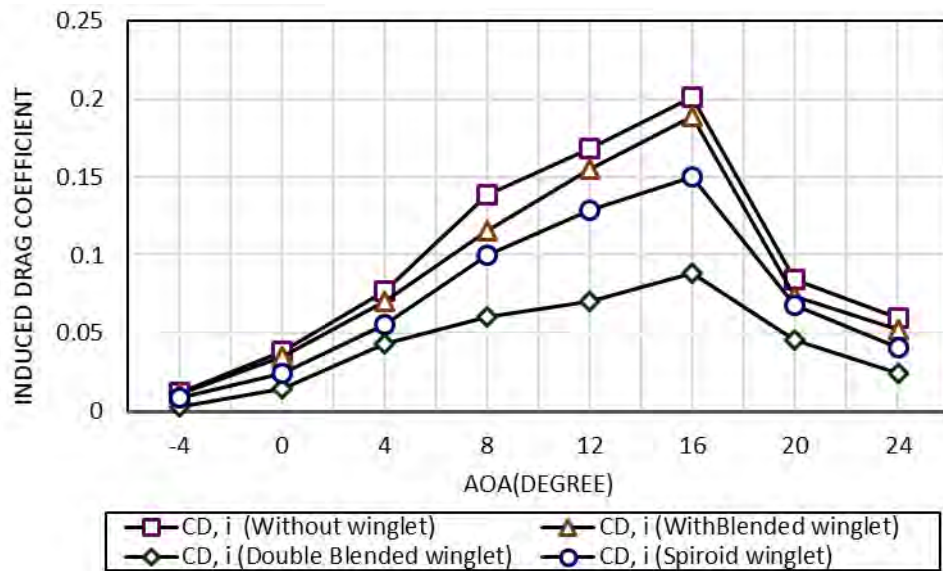


Figure 6.36: Variation of Induced Drag Coefficient with Angle of Attack

CONCLUSIONS AND RECOMMENDATIONS

7.1 Conclusions

Present study investigates experimentally whether introducing winglet at the wing tip improves aerodynamic performance of wing planform. The experiment is done on curved trailing edge tapered wing planform. The reason behind using this specific wing shape is that it has been proven to provide better aerodynamic characteristics by previous research work on wing shape [40]. Then further experiment is conducted by adding winglet at the wing tip of the reference wing. Three types of winglets are studied such as blended winglet, double blended winglet and spiroid winglet. The winglets are added in such a way that all the three wing with winglets have same aspect ratio. By present investigation the following conclusions can be drawn regarding the effects of winglets.

- i. It is observed that, the difference between upper and lower surface pressure of wing with blended winglet is comparatively higher than that of other wing models at most of the angle of attack. This phenomenon happens because the blended winglet reduces the strength of the vortices at the wingtip by reducing the tip vortex.
- ii. From the analysis of variation of lift coefficient with angle of attack, it is observed that the critical angle of attack for wings with winglets remains around 16° as that of the wing without winglet. So, stalling occurs after 16° angle of attack for all wing models.

- iii. The wing with blended winglet provides the best lift characteristics among the four wing models. But both wing with spiroid winglet and wing with double blended winglet provide lower lift than wing without winglet.
- iv. It is found that the drag is lowest for the wing with double blended winglet among the four experimental wing models. The wing with spiroid winglet also exhibits lower drag than wing without winglet. But wing with blended winglet provides higher drag than wing without winglet.
- v. From the lift to drag ratio versus angle of attack curve, it is evident that the wing with spiroid winglet exhibits higher lift to drag ratio than three other wing models. The wing with double blended winglet and wing with blended winglet also provide larger lift to drag ratio than wing without winglet.
- vi. Induced drag coefficient versus angle of attack curve shows that induced drag is lower for wings with winglets than wing without winglet.
- vii. Thus, wing with blended winglet exhibits better aerodynamic performance as it increases lift and at the same time increases lift to drag ratio of curved trailing edge tapered wing planform.

7.2 Recommendations for Future Works

The following recommendations can be made for future work in this field:

- a. The research on the effect of surface roughness of the wing models on aerodynamic characteristics are required to conduct. Same wing models as present study but with materials having low friction coefficient such as fiberglass may be manufactured and tested inside wind tunnel. The results may then be compared with the present study.
- b. The winglet models can be incorporated at other types of wing planforms and then be analyzed to make comparison with each other.
- c. Different types of airfoils may be used for the winglets' cross section to analyze the aerodynamic characteristics of the winglets experimentally and then compare the experimental results with the results of simulations.
- d. The research may be conducted at higher wind tunnel speed to analyze the variation of aerodynamic characteristics of curved trailing edge tapered wing planform with winglets at various air speed or Mach number.

REFERENCES

- [1] Lynch, F.T., “Commercial Transports- Aerodynamic Design for Cruise Performance Efficiency”, *Progress in Astronautics and Aeronautics*, Vol. 81, pp. 81-144, 1982.
- [2] Jenkinson, L. R., Rhodes, D., Simpkin, P. (1999) *Civil jet aircraft design*, Elsevier Ltd., London.
- [3] Thiede, P., “Aerodynamic Drag Reduction Technologies,” Proceedings of the CEAS/ DragNet European Drag Reduction Conference, Vol. 76, June 2000.
- [4] Mclean, D., “Wingtip Devices: What they Do and How They Do it”, presented at the Boeing Performance and Flight Operations Engineering Conference, 2005.
- [5] Whitcomb, R. T., “A Design Approach and Selected Wind-Tunnel Result at High Subsonic Speed for Wing Tip Mounted Winglets”, NASA TN D-8260, 1976.
- [6] Gratzler, L. B., “Blended Winglet,” ed: Google Patents, 1994.
- [7] Gratzler, L. B., “Spiroid-tipped wing,” ed: Google Patents, 1992.
- [8] Roche, U. L., “Wing with a wing grid as the end section,” ed: Google Patents, 1998.
- [9] Henrick, L. L., “Blunt-leading-edge raked wingtips,” ed: Google Patents, 2000.
- [10] Raymer, D. P. (1999) *Aircraft design: a conceptual approach*. American Institute of Aeronautics and Astronautics, Inc., Washington, DC.
- [11] Heyson, H. H., Riebe G. D., and Fulton C. L., “Theoretical

- Parametric Study of the Relative Advantages of Winglets and Wingtip Extension,” NASA Technical Paper, 1977.
- [12] Jones, R. T. and Lasinski, T. A., “Effect of Winglets on the Induced Drag of Ideal Wing Shapes,” NASA TM-81230, 1980.
- [13] Mostafa, S., Bose, S., Nair A., Raheem, M. A., Majeed T., Mohammed, A., and Kim, Y., "A parametric investigation of non-circular spiroid winglets", *EPJ Web of Conferences*, Vol.67, March 2014, pp. 1-6 (2014).
- [14] Ashrafi, Z. A., and Sedaghat, A., "Improving the Aerodynamic Performance of a Wing with Winglet", *International Journal of Natural and Engineering Sciences*, Vol. 8 (3), pp. 52-57, 2014.
- [15] Inam, M. I., Mashud. M., Nahian. A., and Selim. S. M. S., “Induced Drag Reduction for Modern Aircraft without Increasing the Span of the Wing by Using Winglet”, *International Journal of Mechanical & Mechatronics Engineering, IJMME-IJENS*, Vol. 10, No. 03, pp. 2010.
- [16] Bojja, A., and Garre, P., "Analysis on Reducing the Induced Drag Using the Winglet at the Wingtip", *International Journal of Engineering Research & Technology (IJERT)*, Vol. 2, pp. 51-53, 2013.
- [17] Azlin, M. A., Taib, C. F. M., Kasolang, S., and Azlin, F. H. M., "CFD Analysis of Winglets at Low Subsonic Flow", *Proceedings of the World Congress on Engineering*, Vol. I, pp. 87-91, 2011.
- [18] Raj, W. G., and Thomas, T. A., "Design and Analysis of Spiroid Winglet", *International Journal of Innovative Research in Science, Engineering and Technology*, Vol. 4, pp. 1139-1147, 2015.
- [19] Hossain, A., Rahman, A., Iqbal, A. K. M. P., Ariffin, M., and Mazian, M., "Drag Analysis of an Aircraft Wing Model with and without Bird Feather like Winglet", *International Journal of Mechanical, Aerospace, Industrial and Mechatronics Engineering*, Vol. 05, pp. 1894-1899, 2011.

- [20] Gall, P. D., and Smith, H. C., “Aerodynamic Characteristics of Biplanes with Winglets”, *Journal of Aircraft*, Vol. 24, No. 8, pp. 518-522, 1987.
- [21] Rajesh, A., Prasad, Dr. M. S. G., and Praveen, A. S., "Design and Analysis of UCAV Wing with a Winglet by Varying the Cant Angle", *International Journal of Engineering Research & Technology (IJERT)*, Vol. 04, pp. 350-355, 2015.
- [22] Dinesh, M., Mark, V. K., Venkatesan, D. V., Kumar, B. S., Radesh, R. S., and Kumar, V. R. S., "Diagnostic Investigation of Aircraft Performance at Different Winglet Cant Angles", *International Journal of Mechanical, Aerospace, Industrial, Mechatronic and Manufacturing Engineering*, Vol. 08, pp. 1882-191, 2014.
- [23] Weierman, Jacob, and Jacob, J. D., “Winglet Design and Optimization for UAVs”, AIAA 2010-4224, 28th AIAA Applied Aerodynamics Conference, Chicago, Illinois, 28 June - 1 July 2010.
- [24] Jain, R., Jain, S. and Bajpai, L., “Aerodynamics of *Winglet: A Computational Fluid Dynamics Study Using Fluent*”, *International Research Journal of Engineering and Technology (IRJET)*, Vol 03, Issue. 06, pp. 250-254, 2016.
- [25] Dwivedi, Y. D., Pratap, P. M., and Jagadish, D., “Design and Aerodynamic Analysis of Different Winlets”, *International Journal of Innovation in Engineering and Technology (IJIET)*, Volume 7, Issue 2, pp. 401- 410, 2016.
- [26] Gavrilović, N. N., Rašuo, B. P., Dulikravich, G. S., Parezanović, V. B., “Commercial Aircraft Performance Improvement Using Winglets”, *Faculty of Mechanical Engineering Transactions*, Volume 43, pp 1-8, 2015.
- [27] Helal, H. S. M., Khalil, E. E., Abdellatif, O. E., and Elhariry, G. M., “Aerodynamic Analyses of Aircraft-Blended Winglet Performance”, *IOSR Journal of Mechanical and Civil Engineering (IOSR-JMCE)*, Vol. 13, Issue 3, pp 65-72, 2016.

- [28] Panagiotou, P., Kaparos, P., and Yakinthos, K., "Winglet Design and Optimization for a MALE UAV using CFD", *Aerospace Science and Technology*, Vol. 39, pp. 190-205, 2014.
- [29] Sidairi, K. A. and Rameshkumar, G. R., "Design of Winglet Device for Aircraft", *International Journal of Multidisciplinary Sciences and Engineering*, Vol. 07, No.01, pp. 23-30, 2016.
- [30] Reddy, S. R., Sobieczky, S. R., Dulikravic, G. S., and Abdoli. A., "Multi-Element Winglets: Multi-Objective Optimization of Aerodynamic Shapes", *Journal of Aircraft*, Vol. 53, No. 4, pp. 992-1000, 2016.
- [31] Inaganti, M. S., Bhat, M. P., Ugargol, M. R. and Suvarna, M. S. M., "Design and Analysis of Wingtip Devices", *Discovery*, Vol. 31(139), pp. 48-55, 2015.
- [32] Cosin, R., Catalano, F.M., Correa, L.G.N., Entz, R.M.U., "Aerodynamic Analysis of Multi-Winglets for Low Speed Aircraft", *Proceedings of 27th International Congress of the Aeronautical Sciences (ICAS)*, 2010.
- [33] Hossain, A., Rahman, A., Hossen, J, Iqbal, A. K. M. P. and Hasan, S. K. "Application of Fuzzy Logic Approach for an Aircraft Model with and without Winglet", *International Journal of Aerospace and Mechanical Engineering*, Vol.5, No. 04, pp. 224-232, 2011.
- [34] Ning. S. A. and Kroo, I., "Tip Extensions, Winglets, and C-wings: Conceptual Design and Optimization", presented at *26th AIAA Applied Aerodynamics Conference*, Honolulu, Hawaii, 2008.
- [35] Jansen, P. W., Perez, R. E. and Martins, J. R. R. A., "Aerostructural Optimization of Nonplanar Lifting Surfaces", *Journal of Aircraft*, Vol. 47, No. 05, pp. 1491-1503, 2010.
- [36] Maughmer, M. D., Swan, T. S., and Willits, T. S., "The Design and Testing of a Winglet Airfoil for Low-Speed Aircraft", presented at *AIAA 19th Applied Aerodynamics Conference*, Anaheim, CA, 2001.
- [37] Chattot, J. J., "Low Speed Design and Analysis of Wing/ Winglet

- Combinations Including Viscous Effects”, *Journal of Aircraft*, Vol. 43, No. 02, pp. 386-389, 2006.
- [38] Guerrero, J. E., Maestro. D., and Bottaro, A., “Biomimetic spiroid winglets for lift and drag control,” *Comptes Rendus Mècanique*, vol. 340, pp.67-80, 2012.
- [39] Anderson, J.D., “Fundamentals of Aerodynamics”, McGraw-Hill Series in Aeronautical and Aerospace Engineering, 3rd Edition, pp. 15-22, 2010.
- [40] Nazmul M. and Ali M. “*An Experimental Investigation on the Aerodynamic Characteristics of NACA 4412 Aerofoil with Curved-Edge Planform*”, M.Sc. Thesis, Mechanical Engineering, BUET, Dhaka-1000, Bangladesh, 2015.
- [41] Ramesh, P., “*Numerical and Experimental investigation of the effect of geometry modification on the Aerodynamic characteristics of a NACA 64 (2)-415 wing*”, M.Sc. Thesis, Royal Institute of Technology, Stockholm, Sweden, 2013.
- [42] Laurence, K. L. Jr. and Poteat, M. I., “ Aerodynamic Characteristics of several NACA airfoil sections at seven Reynolds number from 0.7×10^6 to 9.0×10^6 ”, *Langley Memorial Aeronautical Laboratory*, 1948.
- [43] Eppler, R., “Airfoil Design and Data”, Springer-Verlag, Berlin, 1990.
- [44] Abbott, I. H. Von Doenhoff, A.E.V., and Stivers, L. S. “Summary of Aerofoil Data”, NACA Report No. 824, 1945.
- [45] Abbott, I. H. and Doenhoff, A.E.V., “Theory of Wing Sections including a Summary of Aerofoil Data”, Dover Publications, New York, 1990.
- [46] Mainuddin, M., and Ali, M.A.T., “Experimental Investigation of Lift to Drag Ratio between Volumetric Equivalent Fuselages”, *Proceedings of the 4th BSME-ASME International Conference on Thermal Engineering*, Dhaka, Bangladesh, pp. 383-390, 2008.

- [47] Alam, G. M. J., “Interference Effect and Flow Pattern of Four Biplane Configurations using NACA 0024 Profile”, *Proceedings of The International Conference on Mechanical Engineering, Dhaka Bangladesh*, 2011.
- [48] Devenport, W.J. and Schetz, J. A., “The Investigation of an Inboard-Winglet Application to a Roadable Aircraft”, M.Sc. In Aerospace Engineering Thesis, Virginia polytechnic Institute and State University, pp. 24-26, 2002.
- [49] Cimbala, J.M., “*Experimental Uncertainty Analysis*”, Online Edition, pp.1-4, 2013.
- [50] *National Aerofoil Data NACA 4412*, Online data, <http://airfoiltools.com/airfoil/details?airfoil=naca4412-il>
- [51] Pinkerton, R. M., “*The Variation with Reynolds Number of Pressure Distribution over an Airfoil Section*”, National Advisory Committee for Aeronautics, Report No. 613, pp. 65-84.
- [52] Agarwal, S. and Kumar, P., “Investigation of Flow Field over NACA4412 with a Vortex Generator”, *Journal of Advanced Research in Applied Mechanics & Computational Fluid Dynamics*, Vol. 01, pp. 1-12, 2014.
- [53] Anderson, J.D., “Introduction to Flight”, McGraw-Hill Series in Aeronautical and Aerospace Engineering, 6th Edition, pp. 326-328, 2010.

APPENDIX-1

Table 3: Calculated Values of Pressure Coefficient at -4° Angle of Attack

Segment	%C	Wing without Winglet		Wing with Blended Winglet		Wing with Double blended Winglet		Wing with Spiroid Winglet	
		C _{pu}	C _{pl}	C _{pu}	C _{pl}	C _{pu}	C _{pl}	C _{pu}	C _{pl}
Segment-A	20	0.022356945	-0.156498616	0.011178473	-0.134141671	0.011178473	-0.022356945	0.011178473	-0.178855562
	40	-0.335354178	0.011178473	-0.30181876	0.022356945	-0.022356945	0.022356945	-0.289427781	-0.011178473
	60	-0.223569452	0.033535418	-0.201212507	0.04471389	-0.011178473	0.06471389	-0.178855562	0.011178473
	80	-0.04471389	0.055892363	-0.011178473	0.055892363	-0.011178473	0.093569452	-0.111784726	0.04471389
Segment-B	20	-0.111784726	-0.189427781	-0.245926397	-0.178855562	0.011178473	-0.032356945	-0.09471389	-0.201212507
	40	-0.340640288	0.022356945	-0.357711123	0.033535418	-0.055892363	-0.011178473	-0.290640288	-0.020121251
	60	-0.201212507	0.067070836	-0.223569452	0.078249308	-0.032356945	0.033535418	-0.189427781	0.033535418
	80	0.04471389	0.089427781	0.023474792	0.09471389	-0.022356945	0.04471389	-0.033535418	0.067070836
Segment-C	20	-0.022356945	-0.223569452	-0.022356945	-0.201212507	0.011178473	0.04471389	-0.022356945	-0.323569452
	40	-0.290640288	0.067070836	-0.357711123	0.022356945	-0.067070836	0.067070836	-0.289427781	0.011178473
	60	-0.189427781	0.011178473	-0.245926397	0.011178473	-0.055892363	0.055892363	-0.201212507	-0.067070836
	80	-0.033535418	-0.122963199	-0.022356945	-0.122963199	-0.017885556	0.022356945	-0.022356945	-0.134141671
Segment-D	20	-0.067070836	-0.033535418	-0.055892363	-0.022356945	0.022356945	0.04471389	-0.022356945	-0.0468378
	40	-0.515422247	-0.092356945	-0.536566685	-0.09471389	-0.231178473	0.033535418	-0.491852795	-0.042478196
	60	-0.324781959	0.011178473	-0.357711123	0	-0.111784726	0.022356945	-0.30181876	0.022356945
	80	0.022356945	0.022356945	0.04471389	0.055892363	-0.011178473	0.011178473	0.022356945	0.067070836

Table 4: Calculated Values of Pressure Coefficient at 0° Angle of Attack									
Segment	%C	Wing without Winglet		Wing with Blended Winglet		Wing with Double blended Winglet		Wing with Spiroid Winglet	
		C_{pu}	C_{pl}	C_{pu}	C_{pl}	C_{pu}	C_{pl}	C_{pu}	C_{pl}
Segment-A	20	0	0.04471389	0.022356945	0.022356945	-0.011178473	-0.011299723	0.04471389	0.04471389
	40	-0.424781959	0.067070836	-0.380068068	0.023474792	-0.051178473	0.04471389	-0.380068068	0.04471389
	60	-0.357711123	0.145320144	-0.312997233	0.089427781	-0.032356945	0.044178473	-0.312997233	0.04471389
	80	-0.022356945	0.04471389	-0.04471389	0.04471389	-0.011178473	0.055892363	-0.067070836	0.04471389
Segment-B	20	-0.447138904	0.033535418	-0.424781959	0.022356945	-0.435960432	-0.01688896	-0.424781959	0.022356945
	40	-0.223569452	0.067070836	-0.323569452	0.022356945	-0.301178473	-0.014532014	-0.245926397	-0.067070836
	60	-0.09471389	0.089427781	-0.223569452	0.033535418	-0.231178473	0.055892363	-0.134141671	0.04471389
	80	-0.04471389	0.111784726	-0.156498616	0.156498616	-0.201212507	0.055892363	-0.068188683	0.178855562
Segment-C	20	-0.022356945	-0.022356945	0	-0.011178473	-0.033535418	0.04471389	0.04471389	-0.022356945
	40	-0.402425014	0.04471389	-0.469495849	0.011178473	-0.055892363	0.04471389	-0.368889596	0.067070836
	60	-0.290640288	0.055892363	-0.290640288	0.067070836	-0.04471389	0.067070836	-0.290640288	0.087070836
	80	-0.04471389	0.067070836	-0.067070836	0.111784726	-0.004471389	0.04471389	0.04471389	0.111784726
Segment-D	20	-0.223569452	-0.022356945	-0.290640288	-0.079367155	-0.022356945	0.089427781	-0.178855562	-0.082608913
	40	-0.737779192	-0.078249308	-0.782493082	-0.011178473	-0.52459264	0.055892363	-0.693065301	-0.013414167
	60	-0.380068068	0.067070836	-0.380068068	0.04471389	-0.455388212	0.04471389	-0.223569452	0.04471389
	80	0.04471389	0.089427781	0.067070836	0.078249308	0.033535418	0.033535418	0.04471389	0.089427781

Table 5: Calculated Values of Pressure Coefficient at 4° Angle of Attack

Segment	%C	Wing without Winglet		Wing with Blended Winglet		Wing with Double blended Winglet		Wing with Spiroid Winglet	
		C _{pu}	C _{pl}	C _{pu}	C _{pl}	C _{pu}	C _{pl}	C _{pu}	C _{pl}
Segment-A	20	-0.648351411	-0.022356945	-0.693065301	-0.022356945	-0.447138904	-0.020121251	-0.648351411	-0.012356945
	40	-0.447138904	0.011178473	-0.447138904	0.011178473	-0.335354178	0.04471389	-0.469495849	0.04471389
	60	-0.380068068	0.04471389	-0.268283342	0.06471389	-0.223569452	0.055892363	-0.26940119	0.052356945
	80	-0.111784726	0.04471389	-0.111784726	0.06471389	-0.134141671	0.055892363	-0.111784726	0.067070836
Segment-B	20	-0.804850027	0.067070836	-0.760136137	0.089427781	-0.693065301	0.033535418	-0.737779192	0.067070836
	40	-0.648351411	0.04471389	-0.523569452	0.055892363	-0.469495849	0.04471389	-0.431879386	0.088309934
	60	-0.447138904	0.033535418	-0.312997233	0.033535418	-0.245926397	0.055892363	-0.231178473	0.092356945
	80	-0.078249308	0.022356945	-0.134141671	0.033535418	-0.055892363	0.067070836	-0.111784726	0.111784726
Segment-C	20	-0.670708356	0.089427781	-0.648351411	0.06471389	-0.670708356	0.026828334	-0.693065301	0.04471389
	40	-0.412493082	0.071117847	-0.395354178	0.04471389	-0.335354178	0.033535418	-0.412493082	0.052356945
	60	-0.357711123	0.055892363	-0.36930653	0.033535418	-0.201212507	0.055892363	-0.189427781	0.067070836
	80	-0.069508411	0.033535418	-0.212390979	0.022356945	-0.111784726	0.067070836	-0.09471389	0.088309934
Segment-D	20	-0.961348644	0.022356945	-1.084311842	0.111784726	-0.782493082	0.033535418	-0.961348644	0.012356945
	40	-0.747138904	0.033535418	-0.79229626	0.092356945	-0.670708356	0.055892363	-0.84471389	0.022356945
	60	-0.347138904	0.055892363	-0.447138904	0.071117847	-0.401212507	0.067070836	-0.394277808	0.033535418
	80	0.071117847	0.067070836	-0.089427781	0.06471389	0.111885514	0.089427781	0.067070836	0.04471389

Table 6: Calculated Values of Pressure Coefficient at 8° Angle of Attack

Segment	%C	Wing without Winglet		Wing with Blended Winglet		Wing with Double blended Winglet		Wing with Spiroid Winglet	
		C _{pu}	C _{pl}	C _{pu}	C _{pl}	C _{pu}	C _{pl}	C _{pu}	C _{pl}
Segment-A	20	-0.693065301	0.092356945	-0.711784726	0.122963199	-0.52459264	0.078249308	-0.648351411	0.078249308
	40	-0.52459264	0.067070836	-0.55892363	0.092356945	-0.394277808	0.055892363	-0.491852795	0.067070836
	60	-0.370708356	0.055892363	-0.394277808	0.071117847	-0.245926397	0.04471389	-0.335354178	0.067070836
	80	-0.111784726	0.022356945	-0.092356945	0.055892363	-0.078249308	0.04471389	-0.089427781	0.033535418
Segment-B	20	-1.11784726	0.134141671	-1.140204205	0.201212507	-0.84471389	0.111784726	-1.084311842	0.123569452
	40	-0.670708356	0.111784726	-0.693065301	0.145320144	-0.515422247	0.089427781	-0.648351411	0.092356945
	60	-0.447138904	0.092356945	-0.469495849	0.111784726	-0.335354178	0.067070836	-0.412493082	0.092356945
	80	-0.134141671	0.055892363	-0.111784726	0.067070836	-0.089427781	0.045831738	-0.09471389	0.055892363
Segment-C	20	-1.184918096	0.201212507	-1.184918096	0.156498616	-0.871920863	0.123569452	-1.140204205	0.156498616
	40	-0.827206973	0.156498616	-0.84471389	0.122963199	-0.55892363	0.092356945	-0.760136137	0.134141671
	60	-0.515422247	0.111784726	-0.52459264	0.089427781	-0.368889596	0.078249308	-0.469495849	0.111784726
	80	-0.156498616	0.092356945	-0.122963199	0.067070836	-0.09471389	0.067070836	-0.111784726	0.089427781
Segment-D	20	-0.947138904	0.067070836	-0.983705589	0.089427781	-0.581280575	0.089427781	-0.916634753	0.055892363
	40	-0.804850027	0.055892363	-0.871920863	0.067070836	-0.569495849	0.067070836	-0.894277808	0.045831738
	60	-0.335354178	0.04471389	-0.340640288	0.055892363	-0.312997233	0.067070836	-0.380068068	0.033535418
	80	-0.09471389	0.033535418	-0.089427781	0.04471389	-0.055892363	0.055892363	-0.089427781	0.033535418

Table 7: Calculated Values of Pressure Coefficient at 12° Angle of Attack

Segment	%C	Wing without Winglet		Wing with Blended Winglet		Wing with Double blended Winglet		Wing with Spiroid Winglet	
		C _{pu}	C _{pl}	C _{pu}	C _{pl}	C _{pu}	C _{pl}	C _{pu}	C _{pl}
Segment-A	20	-0.711784726	0.111784726	-0.760136137	0.123569452	-0.55892363	0.089427781	-0.693065301	0.089427781
	40	-0.536566685	0.089427781	-0.55892363	0.092356945	-0.412493082	0.067070836	-0.51420974	0.067070836
	60	-0.412493082	0.067070836	-0.469495849	0.055892363	-0.270102103	0.055892363	-0.370708356	0.04471389
	80	-0.111784726	0.04471389	-0.122963199	0.055892363	-0.067070836	0.037070836	-0.092356945	0.04471389
Segment-B	20	-1.497915329	0.245926397	-1.58734311	0.268283342	-1.084311842	0.156498616	-1.408487548	0.223569452
	40	-0.894277808	0.156498616	-0.983705589	0.19471389	-0.634141671	0.089427781	-0.811784726	0.145320144
	60	-0.52459264	0.092356945	-0.693065301	0.134141671	-0.394277808	0.055892363	-0.435960432	0.071178473
	80	-0.156498616	0.055892363	-0.134141671	0.04471389	-0.089427781	0.04471389	-0.134141671	0.033535418
Segment-C	20	-1.296702822	0.312997233	-1.386130603	0.279461815	-0.916634753	0.111784726	-1.245926397	0.312997233
	40	-0.84471389	0.189427781	-0.938991699	0.156498616	-0.581280575	0.089427781	-0.811784726	0.156498616
	60	-0.458317377	0.111784726	-0.515422247	0.111784726	-0.370708356	0.067070836	-0.401212507	0.111784726
	80	-0.223569452	0.071178473	-0.111784726	0.067070836	-0.078249308	0.011178473	-0.133023824	0.089427781
Segment-D	20	-1.006062534	0.089427781	-1.140204205	0.134141671	-0.670708356	0.122356945	-1.162561151	0.179973409
	40	-0.804850027	0.067070836	-0.811784726	0.111784726	-0.581280575	0.089427781	-0.961348644	0.111784726
	60	-0.335354178	0.055892363	-0.394277808	0.089427781	-0.412493082	0.067070836	-0.412493082	0.089427781
	80	-0.067070836	0.022356945	-0.089427781	0.04471389	-0.055892363	0.055892363	-0.089427781	0.067070836

Table 8: Calculated Values of Pressure Coefficient at 16° Angle of Attack

Segment	%C	Wing without Winglet		Wing with Blended Winglet		Wing with Double blended Winglet		Wing with Spiroid Winglet	
		C _{pu}	C _{pl}	C _{pu}	C _{pl}	C _{pu}	C _{pl}	C _{pu}	C _{pl}
Segment-A	20	-0.894277808	0.145320144	-0.947138904	0.123569452	-0.634141671	0.111784726	-0.737779192	0.123569452
	40	-0.581280575	0.089427781	-0.634141671	0.111784726	-0.515422247	0.087070836	-0.52459264	0.111784726
	60	-0.491852795	0.04471389	-0.55892363	0.067070836	-0.324781959	0.017070836	-0.401212507	0.097070836
	80	-0.134141671	0.04471389	-0.111784726	0.055892363	-0.078249308	0.013414167	-0.156498616	0.04471389
Segment-B	20	-1.453201438	0.424781959	-1.58734311	0.189427781	-1.173739623	0.156498616	-1.721484781	0.178855562
	40	-0.961348644	0.178855562	-0.916634753	0.145320144	-0.737779192	0.122356945	-0.782493082	0.156498616
	60	-0.634141671	0.123569452	-0.760136137	0.071117847	-0.515422247	0.089427781	-0.536566685	0.111784726
	80	-0.178855562	0.04471389	-0.179973409	0.055892363	-0.111784726	0.055892363	-0.170102103	0.089427781
Segment-C	20	-1.386130603	0.201212507	-1.453201438	0.391246541	-0.938991699	0.089427781	-1.58734311	0.089427781
	40	-0.871920863	0.156498616	-0.871920863	0.145320144	-0.694277808	0.067070836	-0.894277808	0.067070836
	60	-0.289427781	0.089427781	-0.581280575	0.100606253	-0.435960432	0.037070836	-0.312997233	0.012356945
	80	-0.231178473	0.022356945	-0.156498616	0.017885556	-0.087070836	0.022356945	-0.134141671	0.01059264
Segment-D	20	-1.184918096	0.201212507	-1.296702822	0.402997233	-0.737779192	0.156498616	-1.386130603	0.424781959
	40	-0.84471389	0.134141671	-0.938991699	0.25710487	-0.670708356	0.089427781	-0.961348644	0.291758135
	60	-0.458317377	0.121784726	-0.491852795	0.19471389	-0.424781959	0.078249308	-0.569495849	0.09471389
	80	-0.089427781	0.111784726	-0.04471389	0.134141671	-0.067070836	0.067070836	-0.067070836	0.022356945

Table 9: Calculated Values of Pressure Coefficient at 20° Angle of Attack

Segment	%C	Wing without Winglet		Wing with Blended Winglet		Wing with Double blended Winglet		Wing with Spiroid Winglet	
		C _{pu}	C _{pl}	C _{pu}	C _{pl}	C _{pu}	C _{pl}	C _{pu}	C _{pl}
Segment-A	20	-0.424781959	0.089427781	-0.515422247	0.111784726	-0.292459048	0.089427781	-0.380068068	0.156498616
	40	-0.312997233	0.071178473	-0.380068068	0.089427781	-0.247138904	0.067070836	-0.281784726	0.134141671
	60	-0.268283342	0.067070836	-0.290640288	0.055892363	-0.167677089	0.055926397	-0.252997233	0.067070836
	80	-0.067070836	0.055892363	-0.071178473	0.04471389	-0.055926397	0.04471389	-0.097070836	-0.022356945
Segment-B	20	-0.469495849	0.156498616	-0.480674322	0.134141671	-0.357711123	0.134141671	-0.648351411	0.222997233
	40	-0.335070836	0.134141671	-0.401212507	0.121784726	-0.30181876	0.09471389	-0.424781959	0.111784726
	60	-0.268283342	0.121784726	-0.290640288	0.111784726	-0.252997233	0.089427781	-0.402425014	0.089427781
	80	-0.089427781	0.089427781	-0.111784726	0.078249308	-0.189427781	0.067070836	-0.080485003	0.067070836
Segment-C	20	-0.52459264	0.424781959	-0.491852795	0.458317377	-0.424781959	0.201212507	-0.380068068	0.389427781
	40	-0.412493082	0.134141671	-0.380068068	0.255892363	-0.36930653	0.134141671	-0.268283342	0.312997233
	60	-0.335354178	0.111784726	-0.312997233	0.122356945	-0.270102103	0.111784726	-0.201212507	0.25710487
	80	-0.111784726	0.067070836	-0.089427781	0.110640288	-0.089427781	0.089427781	-0.097070836	0.111784726
Segment-D	20	-0.737779192	0.25710487	-0.693065301	0.312997233	-0.470708356	0.252997233	-0.491852795	0.357711123
	40	-0.648351411	0.201212507	-0.581280575	0.268283342	-0.435960432	0.156498616	-0.424781959	0.201427781
	60	-0.536566685	0.111784726	-0.470708356	0.156498616	-0.267070836	0.134141671	-0.335354178	0.156498616
	80	-0.223569452	0.089427781	-0.19471389	0.067070836	-0.134141671	0.089427781	-0.089427781	0.097070836

Table 10: Calculated Values of Pressure Coefficient at 24° Angle of Attack

Segment	%C	Wing without Winglet		Wing with Blended Winglet		Wing with Double blended Winglet		Wing with Spiroid Winglet	
		C _{pu}	C _{pl}	C _{pu}	C _{pl}	C _{pu}	C _{pl}	C _{pu}	C _{pl}
Segment-A	20	-0.290640288	0.298855562	-0.380068068	0.279461815	-0.353031267	0.335354178	-0.412493082	0.268283342
	40	-0.245926397	0.235960432	-0.335354178	0.222997233	-0.189427781	0.100606253	-0.389495849	0.201212507
	60	-0.201212507	0.178855562	-0.312997233	0.156498616	-0.078249308	0.033535418	-0.368889596	0.134141671
	80	0.089427781	0.111784726	0.022356945	0.04471389	0.067070836	0.022356945	0.089427781	0.067070836
Segment-B	20	-0.312997233	0.279461815	-0.424781959	0.30181876	-0.268889596	0.189427781	-0.335354178	0.245926397
	40	-0.255892363	0.151784726	-0.356498616	0.223569452	-0.235960432	0.134141671	-0.312997233	0.156498616
	60	-0.201427781	0.087070836	-0.247138904	0.170102103	-0.167070836	0.101212507	-0.211784726	0.078855562
	80	-0.201427781	-0.013414167	-0.201212507	0.078249308	-0.122963199	0.089427781	-0.201212507	-0.022356945
Segment-C	20	-0.447138904	0.55892363	-0.424781959	0.491852795	-0.290640288	0.30181876	-0.380068068	0.469495849
	40	-0.356498616	0.252997233	-0.298855562	0.201427781	-0.312997233	0.134141671	-0.278855562	0.235960432
	60	-0.357711123	0.178855562	-0.290640288	0.049427781	-0.111784726	0.089427781	-0.212997233	0.111784726
	80	0.015649862	-0.022356945	-0.04471389	-0.012997233	0.022356945	0.04471389	0.013414167	-0.022356945
Segment-D	20	-0.51420974	0.312997233	-0.458317377	0.469495849	-0.223569452	0.19471389	-0.402425014	0.447138904
	40	-0.491852795	0.223569452	-0.424781959	0.156498616	-0.32930653	0.151784726	-0.335354178	0.201427781
	60	-0.435960432	0.071117847	-0.357711123	0.067070836	-0.313603486	0.111784726	-0.357711123	0.09471389
	80	-0.111784726	-0.019003403	-0.134141671	-0.020121251	-0.100606253	0.067070836	-0.089427781	-0.012478196

APPENDIX-11

UNCERTAINTY ANALYSIS

Experimental uncertainty analysis by Cimbala [49] provides a method for predicting the uncertainty of a variable based on its component uncertainty. Furthermore, unless otherwise specified, each of these uncertainties has a confidence level of 95%.

In this investigation, values of pressure coefficients on each surface points are calculated from the respective multi-tube manometer readings obtained during wind tunnel test. The coefficient of lift and coefficient of drag is estimated from the surface pressure coefficients. As such, the uncertainty started from the initial measurement of manometer height and it propagates with the values of C_p , C_L and C_D . The uncertainty in C_p , C_L and C_D can be estimated if their components individual uncertainty is known.

The equation of C_p can be rewritten in terms of all its components from equation (4.2) as follows:

$$C_p = \frac{\rho_{water} \times g \times \Delta H_{Multitubemanometer}}{\frac{1}{2} \rho_{air} \times U_{\alpha}^2} = f(g, \rho_{water}, \rho_{air}, U_{\alpha}, \Delta H_{Multitubemanometer})$$

Due to temperature rise during the experiment, the density of air is changed. So, uncertainty of 0.02 may be assumed as the uncertainty of ρ_{air} (difference between the air density at 20° C and 25° C). Uncertainty in the measurement of height from the multi-tube manometer may be assumed 0.0015 (as the reading vary ± 1.5 mm or 0.0015 m from the actual reading). The uncertainty in other components of C_p can be neglected. So,

$$\begin{aligned} u_{\rho_{air}} &= 0.02 \\ u_{\Delta H} &= 0.0015 \end{aligned}$$

The expected uncertainty in C_p can be estimated from the following formula:

$$U_{C_p} = \pm \sqrt{\left(u_{\rho_{air}} \frac{\partial C_p}{\partial \rho_{air}}\right)^2 + \left(u_{\Delta H} \frac{\partial C_p}{\partial \Delta H}\right)^2} \text{-----(1)}$$

Let us consider the case of segment-A of wing with blended winglet at 0° AOA. There, at 20% chord on the upper surface, $\Delta H = -1$ mm, $\rho_{air} = 1.204$ kg/m³ and corresponding $C_p = 0.02236$. So, from equation (1),

$$\frac{\partial C_p}{\partial \rho_{air}} = -\frac{C_p}{\rho_{air}} = -\frac{0.02236}{1.204} = -0.0186$$

$$\frac{\partial C_p}{\partial \Delta H} = \frac{C_p}{\Delta H} = \frac{0.02236}{0.001} = 22.36$$

Putting the above two values and the component uncertainties in equation (1), we get the uncertainty of C_p as:

$$U_{cp} = \pm \sqrt{(0.02 \times (-)0.0186)^2 + (0.0015 \times 22.36)^2} = \pm 0.034$$

So, the uncertainty in C_p is ± 3.4 %. Now, from equation 4.23

$$C_n = \sum_{i=1}^n \left[(C_{p,l,i} - C_{p,u,i}) \Delta \left(\frac{x_i}{c} \right) \right] = f(C_{p,l,i}, C_{p,u,i})$$

$$C_a = \sum_{i=0}^n \left[\left(C_{p,u,i} \frac{\Delta y_{u,i}}{\Delta x_i} - C_{p,l,i} \frac{\Delta y_{l,i}}{\Delta x_i} \right) \Delta \left(\frac{x_i}{c} \right) \right] = f(C_{p,l,i}, C_{p,u,i})$$

The uncertainty in C_n can be found from the following formula:

$$U_{C_n} = \pm \sqrt{\left(u_{C_{pu}} \frac{\partial C_n}{\partial C_{pu}}\right)^2 + \left(u_{C_{pl}} \frac{\partial C_n}{\partial C_{pl}}\right)^2} \text{-----}(2)$$

Now, at 20% chord length of segment, the value of x coordinate is 28 mm, y coordinates of upper and lower surface are 12.32 mm and -3.836 mm and chord length is 140 mm. So, from equation (2),

$$\frac{\partial C_n}{\partial C_{pu}} = -\frac{X_1}{C} = -\frac{28}{140} = -0.2$$

$$\frac{\partial C_n}{\partial C_{pl}} = \frac{X_1}{C} = \frac{28}{140} = 0.2$$

Putting the above two values and the component uncertainties in equation (2), we get the uncertainty of C_n as:

$$U_{C_n} = \pm \sqrt{(0.034 \times (-0.2))^2 + (0.034 \times 0.2)^2} = \pm 0.0095$$

So, the uncertainty in C_n is ± 0.95 %. The uncertainty in C_a can be found from the following formula:

$$U_{C_a} = \pm \sqrt{\left(u_{C_{pu}} \frac{\partial C_a}{\partial C_{pu}}\right)^2 + \left(u_{C_{pl}} \frac{\partial C_a}{\partial C_{pl}}\right)^2} \text{-----}(3)$$

So from equation (3),

$$\frac{\partial C_a}{\partial C_{pu}} = \frac{y_{u,1}}{C} = \frac{12.32}{140} = 0.088$$

$$\frac{\partial C_a}{\partial C_{pl}} = \frac{y_{l,1}}{C} = \frac{3.836}{140} = 0.0274$$

Now putting the above two values and the component uncertainties in equation (3), we get the uncertainty of C_a as:

$$U_{C_a} = \pm \sqrt{(0.034 \times 0.0274)^2 + (0.034 \times 0.088)^2} = \pm 0.0031$$

So, the uncertainty in C_a is ± 0.31 %. Now from equation (4.25) and (4.26) expression for lift and drag coefficient are

$$c_l = c_n \cos \alpha - c_a \sin \alpha$$

$$c_d = c_n \sin \alpha + c_a \cos \alpha$$

For 0° angle of attack the above two equation becomes,

$$C_l = C_n$$

$$C_d = C_a$$

As $C_l = C_n$ and $C_d = C_a$, the uncertainties of C_l is equal to the uncertainties of C_n as well as the uncertainties of C_d is equal to the uncertainties of C_a . So, the uncertainty in C_l is ± 0.95 % and the uncertainty in C_d is ± 0.31 %.